DEVELOPMENT OF GPR DATA ANALYSIS ALGORITHMS FOR PREDICTING THIN ASPHALT CONCRETE OVERLAY THICKNESS AND DENSITY

BY

SHAN ZHAO

DISSERTATION

Submitted in partial fulfillment of the requirements
for the degree of Doctor of Philosophy in Civil Engineering
in the Graduate College of the
University of Illinois at Urbana-Champaign, 2018

Urbana, Illinois

Doctoral Committee:

Professor Imad L. Al-Qadi, Chair
Professor Jeffery R. Roesler
Professor John S. Popovics
Associate Professor Zhen Leng
Research Assistant Professor Hasan Ozer

ABSTRACT

Thin asphalt concrete (AC) overlay is a commonly used asphalt pavement maintenance strategy. The thickness and density of thin AC overlay are important to achieving proper pavement performance, which can be evaluated using ground-penetrating radar (GPR). The traditional methods for predicting pavement thickness and density relies on the accurate determination of electromagnetic (EM) signal reflection amplitude and time delay. Due to the limitation of GPR antenna bandwidth, the range resolution of the GPR signal is insufficient for thin pavement layer evaluation. To this end, the objective of this study is to develop signal processing techniques to increase the resolution of GPR signals, such that they can be applied to thin AC overlay evaluation.

First, the generic GPR forward 2-D imaging scheme is discussed. Then two linear inversion techniques are proposed, including migration and sparse reconstruction. Both algorithms were validated on GPR signals reflected from buried pipes using finite difference time domain (FDTD) simulation.

Second, as a special case of the 2-D GPR imaging and linear inversion reconstruction, regularized deconvolution was applied to GPR signals reflected from thin AC overlays. Four types of regularization methods, including Tikhonov regularization and total variation regularization, were compared in terms of accuracy in estimating thin pavement layer thickness. The L-curve method was used to identify the appropriate regularization parameter.

A subspace method—a multiple signal classification (MUSIC) algorithm—was then utilized to increase the resolution of 3-D GPR signals. An extended common midpoint (XCMP) method was used to find the dielectric constant and the thickness of the thin AC overlay at a full-scale test section. The results show that the MUSIC algorithm is an effective approach for increasing the 3-D GPR signal range resolution when the XCMP method is applied on thin AC overlay.

Furthermore, a non-linear inversion technique is proposed based on gradient descent. The proposed non-linear optimization algorithm was applied on real GPR data reflected from thin AC overlay and the thickness and density prediction results are accurate.

Finally, a “modified reference scan” approach was developed to eliminate the effect of AC pavement surface moisture on GPR signals, such that the density of thin AC overlay can be monitored in real time during compaction.

ACKNOWLEDGEMENTS

I would like to express my earnest gratitude to my advisor Prof. Imad L. Al-Qadi, for his guidance and support during this research. His encouragement and belief in me also helped me overcome the difficulties I encountered in both research and life. I would also like to thank Prof. Jefferey R. Roesler, Prof. John S. Popovics, Prof. Zhen Leng, and Prof. Hasan Ozer for accepting to be in my committee and for taking time to improve my study and dissertation.

My thanks also go to the research engineers at the Illinois Center for Transportation (ICT), Michael Johnson, Shenghua Wu, Greg Renshaw and Jim Meister. I wouldn't be able to conduct the research without their help. Special thanks also go to my friends and colleagues at the Advanced Transportation Research and Engineering Laboratory (ATREL) for the great time we spent together. I learned a lot from each of them.

Finally, my highest gratitude goes to my mother Wencai Tian and my father Laibin Zhao for their unconditional love and support. They have always been there whenever I need them. Same gratitude also goes to my other family members.

TABLE OF CONTENTS

CHAPTER 1: INTRODUCTION

1.1 Background

In the United States, there are over 4.2 million miles of paved roads, including more than 76,000 miles of expressways (CIA 2018). To properly manage and maintain this road network, the U.S. spends over $200 million dollars of combined federal, state, and local funding each year (FHWA 2014). Since the completion of the U.S. Interstate Highway system decades ago, the rehabilitation and maintenance of existing pavements have become more important than the construction of new pavements.

The most common pavement maintenance treatment in the U.S. is AC overlay. Layer thickness is an important parameter in pavement design (Huang 2004; Yoder and Witczak 1975; Masad et al. 2012). Newly constructed AC overlay uses thickness for quality control and quality assurance (QC/QA), and existing AC overlay uses thickness to assess pavement condition and predict pavement remaining service life.

Density is another parameter that can greatly influence AC pavement performance. Achieving an appropriate density can reduce the maintenance and rehabilitation cost of the AC pavement, while improper density could result in premature pavement failures (Leng et al. 2012; Lytton et al. 1993). Density can also be used during AC pavement compaction to achieve the desired air voids.

1.2 Problem Statement

The traditional way of measuring asphalt pavement thickness and density is by taking core samples and subjecting them to laboratory tests. In addition to being destructive, taking cores can be time consuming and expensive, and can only cover limited locations. An alternative approach to measuring asphalt density is to use a nuclear density gauge. While this method is nondestructive, the use of radioactive materials requires a special license.

Another alternative is ground penetrating radar (GPR), a special type of radar that can be used to image subsurface targets such as rebar (Soldovieri 2011), drainage pipe (Zhao and Al-Qadi 2017a), archaeological structures (Sala and Linford 2012), landmines (Eide and Hjelmstad 2004), and railway ballast (Al-Qadi et al. 2016). In pavement engineering, GPR has been applied to predict AC pavement thickness (Al-Qadi et al. 2003; Al-Qadi and Lahouar 2005) and density (Al-Qadi et al. 2010; Leng 2011). The conventional way of estimating AC layer thickness involves two steps: predicting the dielectric constant of the AC pavement layer using the surface reflection method (Al-Qadi et al. 2001) and calculating the AC layer thickness using the two-way travel time (TWTT) method. The dielectric constant is also used to calculate the density of the AC pavement. Further details will be discussed in chapter 2.

The conventional method for thickness and density estimation relies on the accurate determination of the reflection time and amplitude. Because the bandwidth of the GPR antenna is usually limited, the resulting GPR time domain signal has a limited resolution. For thin asphalt overlay, when the layer thickness is smaller than the signal wave length, the reflection from two adjacent pavement layer interfaces will overlap, making it difficult to accurately determine the reflection time and amplitude. Therefore, signal processing methods need to be developed to solve the problem of thickness and density estimation for thin AC pavement overlay.

1.3 Objective

The main objective of this research is to develop signal processing techniques that can increase the range resolution of GPR signals, allowing GPR to be used to predict the thickness and density of thin AC overlay. The research efforts focus on developing linear inversion, non-linear optimization, and subspace methods. Additionally, this study also aims to develop an algorithm that allows for the real time compaction monitoring of AC pavement using GPR.

To validate the outcome of this study, the proposed algorithms were applied on finite difference time domain (FDTD) simulated data; on GPR data collected from test sections; and on GPR data collected from field tests.

1.4 Scope

The dissertation is divided into nine chapters. Chapter 1 briefly introduces the background and the objective of the research. Chapter 2 presents the current state of knowledge including fundamental GPR and EM theories and applications of GPR on pavement engineering. Chapter 3 discusses the generic GPR imaging scheme and reconstruction techniques. In Chapter 4, a linear inversion method, regularized deconvolution is developed and used on FDTD simulated GPR signals. Chapter 5 further validates the regularization technique using field study GPR data. Chapter 6 describes a subspace based super-resolution method, and validates the method on 3-D GPR data using the XCMP method. Chapter 7 presents a nonlinear optimization method that can accurately recover the surface reflection and time delay of GPR signals reflected from thin AC overlay. Chapter 8 describes a “modified reference scan” approach that allows real time compaction monitoring of AC pavement using GPR. Finally, chapter 9 provides the findings and conclusions of the study, and points toward future studies.

1.5 Importance of the Study

The accurate prediction of AC overlay thickness and density is important both during pavement construction and service. During the construction of AC overlay, monitoring thickness and density is critical to achieving the proper compaction effort. Thickness and density measurements are also used for QC/QA after pavement construction. Inadequate thickness or improper compaction will be costly to contractors and the public, as pavements fail. During the service life of pavement, thickness and density information will help experts make smart decisions on rehabilitation time and strategy.

With further development of this study, the GPR system can be integrated with an asphalt compactor roller to achieve real time compaction monitoring of both regular AC pavement as well thin AC overlay. This could potentially help to achieve optimum AC pavement compaction performance.

CHAPTER 2: BACKGROUND KNOWLEDGE

2.1 AC Overlay

Pavement deteriorates over time due to traffic loads and environment effects. Pavement preservation is a proactive approach to maintaining the existing highway, while pavement rehabilitation addresses the repair of part of the pavement when deterioration happens (IDOT 2010). Well-constructed pavements, such as full-depth asphalt pavement, need only functional improvements over time, rather than structural enhancements (Newcomb 2009). As the most common pavement preservation and rehabilitation treatment, asphalt concrete (AC) overlay can be used for either structural or non-structural purposes. Structural overlays are used to increase pavement structural capacity, while non-structural asphalt overlays are frequently used to improve the functionality of a pavement, including the improvement of friction and ride quality, correcting surface cracks, and reducing noise. Non-structural overlays are usually thin overlays with thicknesses ranging from 12.7 mm to 38.1 mm (Newcomb 2009). Thin AC overlays have advantages over other pavement rehabilitation and preservation methods, including low life cycle cost, less dust generation during construction, and the ability to be constructed in stages (Newcomb 2009).

2.2 GPR Principles

2.2.1 EM theories

The classical EM phenomenon is governed by a set of Maxwell's equations. While Maxwell's equations in the integral form are valid everywhere, the differential form in terms of free charges and currents is more convenient for analyzing physical problems:

$$\nabla\vec{E} = \frac{\rho}{\varepsilon}, \tag{2-1}$$

$$\nabla\vec{H} = 0, \tag{2-2}$$

$$\nabla \times \vec{E} = -\mu\frac{\partial\vec{H}}{\partial t}, \tag{2-3}$$

$$\nabla \times \vec{H} = \vec{J} + \varepsilon\frac{\partial\vec{E}}{\partial t}. \tag{2-4}$$

where $\vec{E}$ is electric field intensity (Volts/meter), $\vec{H}$ is magnetic field intensity (Amps/meter), ε is permittivity of medium (Farads/meter), μ is permeability of free space (Henrys/meter), $\vec{J}$ is the electric current density (Amperes/meter^2), and ρ is the electric charge density (coulombs/meter^3).

Faraday's induction law (2-3) shows that a changing magnetic flux can generate an electric field. The Maxwell-Ampere's law (2-4) shows that an electric current or a changing electric field can generate a magnetic field. Gauss' law (2-1) pertains to static electric fields, showing that the electric field lines originate from positive charges and terminate at negative charges. Gauss' law for magnetism (2-2) shows that magnetic flux lines don't have origins and must form a circle. In this study, the pavement mediums are assumed to be lossless, non-magnetic, homogeneous, isotropic, and non-dispersive.

In the application of GPR, the target is usually in the far field region of the antenna. In the far field of an antenna, the EM field exhibits local plane wave behavior. If we assume the EM wave is propagating in the z direction, the EM filed is linearly polarized (the most general case being elliptically polarized) with an electric field only in the x direction. Then, by solving Maxwell's equations, the harmonic plane wave solution in a lossless medium (the conductivity σ is zero) can be expressed as follows:

$$E(z) = E_{0x}\cos(\omega t - \beta z), \tag{2-5}$$

$$H(z) = H_{0y}\cos(\omega t - \beta z), \tag{2-6}$$

where E_{0x} and H_{0y} are arbitrary constant values, $Z = \frac{E_{0x}}{H_{0y}} = \frac{\mu}{\varepsilon}$ is the wave impedance, ω is the angular frequency, and $\beta = \omega\sqrt{\mu\varepsilon}$ is the phase constant.

The EM wave velocity *v* can then be calculated as:

$$\mathrm{v} = \frac{\omega}{\beta} = \frac{1}{\sqrt{\mu\varepsilon}}. \tag{2-7}$$

In free space, the EM wave velocity is equal to $\frac{1}{\sqrt{\mu_0\varepsilon_0}} = 3 \times 10^8 m/s$, which is the speed of light in free space.

If the plane wave is normally incident on an interface of medium 1 and medium 2, the reflection coefficient *R* and transmission coefficient *T* are:

$$\mathrm{R} = \frac{\eta_2 - \eta_1}{\eta_2 + \eta_1}, \tag{2-8}$$

$$\mathrm{T} = \frac{2\eta_2}{\eta_2 + \eta_1}, \tag{2-9}$$

where $\eta_1 = \sqrt{\mu_1/\varepsilon_1}$ and $\eta_2 = \sqrt{\mu_2/\varepsilon_2}$ are the intrinsic impedance of medium 1 and medium 2, respectively. This is Snell's law of reflection and transmission in the normal incident case. If medium 2 is a perfect conductor such as metal, then $\eta_2 = 0$, R = -1, and T = 0, meaning that all of the EM waves are flipped and reflected back.

2.2.2 GPR systems

Electrical signals are transmitted via transmission line or through empty space. Antennas are essentially transducers that can convert electrical signals from transmission lines to empty space, or vice versa. According to IEEE, an antenna is defined as "that part of transmitting or receiving system that is designed to radiate or to receive EM waves" (IEEE 1993). GPR, in contrast, is a type of radar whose purpose is to locate targets or interfaces buried with earth material (Daniels 2005).

A GPR system consists of a control unit, antenna, and power supply. The control unit contains the electronics which generate an incident electric signal to the antenna. It is built in with a computer or connected to an outside computer which operates the GPR system and stores the collected GPR data. GPR has three common signal types: pulsed signals, stepped frequency signals, and frequency-modulated signals. A GPR antenna serves as the transmitter and receiver to convert between electrical signals and EM waves. GPR antennas can be either ground-coupled or air-coupled. Ground-coupled antennas have the advantage of deeper penetration depth, while air-coupled antennas can be mounted on vehicles and can travel at highway speed. Other instruments such as distance measuring instrument (DMI) and GPS can also be used together with GPR to provide the location of the GPR scans.

This study mainly uses an air-coupled GPR system with horn antennas manufactured by Geophysical Survey Systems, Inc. (GSSI). Figure 2-1 shows two 2GHz air-coupled antennas mounted on a van. Figure 2-2 shows SIR20, a GPR control unit. Figure 2-3 shows the DMI and GPS antennas that are used during GPR data collection.

Figure 2-1 A vehicle-mounted air-coupled GPR system

Figure 2-2 SIR20 – GPR control unit

Figure 2-3 GPS antenna (left) and DMI (right)

2.3 GPR Applications in Asphalt Pavement

2.3.1 Layer thickness estimation

The most successful application of GPR on asphalt pavement is the estimation of layer thickness using the surface reflection and two-way travel time (TWTT) method. Figure 2-4 shows a typical GPR signal reflected from a two-layered AC pavement, where “Tx/Rx” represents a monostatic air-coupled antenna. The surface AC layer has a dielectric constant of ε_1 and thickness of h; the second layer (leveling binder or the old pavement) has a dielectric constant value of ε_2. A_1 and A_2 are the amplitudes of the reflection from the surface and the bottom of the surface layer, respectively. The two red arrows represent the impulse response of the pavement system. It should be noted that the reflection coefficient at the first layer and second layer interface is positive in Figure 2-4, assuming $\varepsilon_2 < \varepsilon_1$.

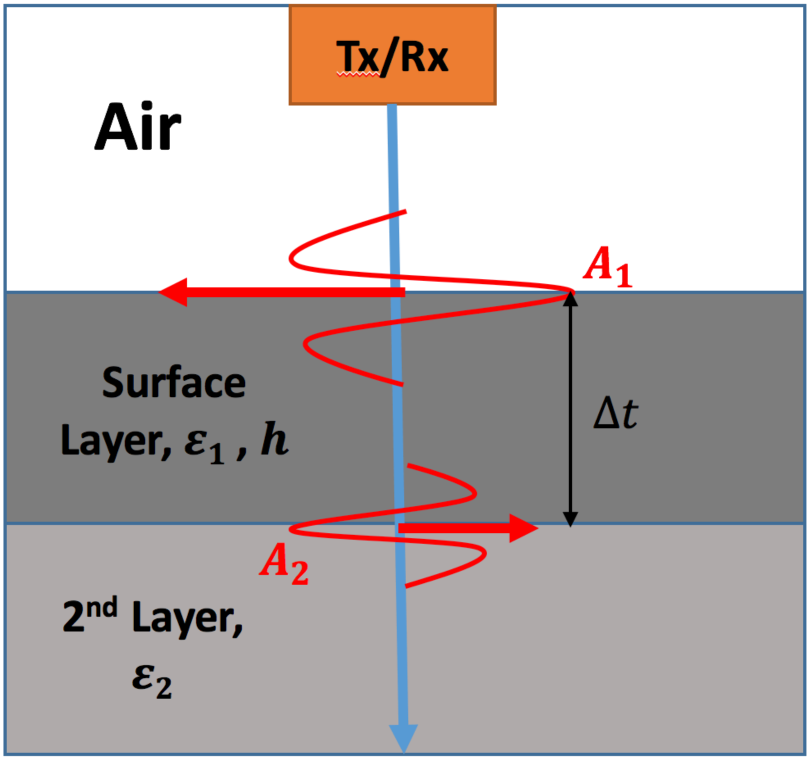

Figure 2-4 GPR signal reflected from a two-layered AC pavement

In the scenario shown in Figure 2-4, the surface layer thickness can be determined by:

$$h = (v\Delta t)/2, \tag{2-10}$$

where Δt is the TWTT between the reflection from the surface and the reflection from the bottom of the surface, and

$$v = c/\sqrt{\varepsilon_1} \tag{2-11}$$

is the speed of the EM wave in the surface layer, and $c = 3 \times 10^8 m/s$ is the speed of light in free space. According to equation (2-8), the dielectric constant of the surface layer can be determined using the following equation:

$$\varepsilon_1 = \left(\frac{1 + A_1/A_p}{1 - A_1/A_p}\right)^2, \tag{2-12}$$

where A_p is the amplitude of the reflection from a copper plate.

A similar procedure can be performed on each layer to find its dielectric constant and thickness.

Al-Qadi et al. (2003) report that the TWTT and surface reflection method shown in equations (2-10) through (2-13) provide an AC layer thickness average estimation error of 2.9%, using GPR data collected from AC pavements 100 mm to 250 mm thick. Another way to estimate AC pavement thickness is to use the common midpoint method (Lahouar et al. 2002), which requires multiple GPR channels.

2.3.2 Density estimation

AC pavement density can be predicted by relating the dielectric constant of the AC layer to its bulk specific gravity (G_{mb}). It has been suggested that an exponential regression relationship can be used (Saarenketo 1997). However, that is a simplified approach which was verified only on certain mixture types; it also relies on calibrating the relationship for each AC mixture type.

A more generic model can be developed using EM mixing theory (Shivola 1989). There are three existing EM mixing models: the complex refractive index model (CRI), the Rayleigh mixing model, and the Böttcher mixing model (Sihvola 1989; Böttcher 1978; Behari 2006). Beaucamp et al. (2013) used the Lichtenecker-Rother equation, which is a generalized CRI model, to predict asphalt mixture density from GPR. The study also used a method to correct for the effect of vehicle-mounted antenna vibration on GPR signals, which increases the density prediction accuracy. The study concluded that the proposed methods can be used for asphalt pavement compaction monitoring. A research group at the University of Illinois has modified the Böttcher mixing model, using a shape factor of -0.3. The new model is referred to as the Al-Qadi Lahouar Leng (ALL) model (Al-Qadi et al. 2010; Leng 2011). It was concluded that the ALL model outperforms other EM mixing models (Leng et al. 2011; Leng et al. 2012). The ALL model is presented below:

$$G_{mb} = \frac{\frac{\varepsilon_{AC} - \varepsilon_b}{3\varepsilon_{AC} - 2.3\varepsilon_b} - \frac{1 - \varepsilon_b}{1 - 2.3\varepsilon_b + 2\varepsilon_{AC}}}{\frac{\varepsilon_s - \varepsilon_b}{\varepsilon_s - 2.3\varepsilon_b + 2\varepsilon_{AC}} \cdot \frac{1 - P_b}{G_{se}} - \frac{1 - \varepsilon_b}{1 - 2.3\varepsilon_b + 2\varepsilon_{AC}} \cdot \frac{1}{G_{mm}}}, \qquad (2\text{-}13)$$

where ε_{AC} is the dielectric constant of the asphalt mixture, ε_b is the dielectric constant of the asphalt binder, ε_s is the dielectric constant of the aggregate, P_b is the asphalt binder content, G_{se} is the effective specific gravity of the aggregate, and G_{mm} is the maximum specific gravity of the AC mixture. ε_b is set as constant 3. G_{mm}, G_{se} and P_b are known from AC mix design. ε_s, however, needs to be determined using calibration from core data.

2.4 Super-Resolution of GPR Signals

As explained in section 1.2, the resolution of GPR signals need to be increased for its effective application to thin AC overlays. To this end, signal processing techniques, known as super-resolution techniques, need to be applied. The most common method to recover the layer reflectivity and thickness is deconvolution in either time or frequency domain (Riad 1986), which requires prior knowledge of the incident signal. The details of the deconvolution method will be discussed in chapter 4. If the incident signal is unknown, a blind deconvolution approach based on optimization can instead be used to recover the layer structure (Li 2014; Jia et al. 2017). Recently, machine learning algorithms have also been applied to GPR signal super-resolution. For example, Le Bastard et al. (2014) used a support vector machine (SVM) to find the thickness of thin pavement layer; however, machine learning algorithms usually require large amounts of data for model training. Another class of super-resolution algorithms are based on subspace analysis, such as MUSIC (multiple signal classification) algorithm (Schmidt 1986; Wax and Kailath 1985; Le Bastard et al. 2007; Zhao and Al-Qadi 2018); these approaches usually require knowledge of the noise subspace. Ihamouten et al. (2018) studied the stepped frequency GPR full wave inversion problem (Lambot et al. 2004) using optimization in the frequency domain to consider the near-field condition and vibration. The dielectric and thickness of pavement structures were predicted with good accuracy.

In this study, both traditional deconvolution methods and optimization methods will be discussed. Additional techniques will be proposed to either stabilize the solution or increase the result accuracy. The details will be covered in following chapters, especially in section 4.2.

2.5 Summary

In this chapter, the thin AC overlay was introduced, and the importance of the thin AC overlay thickness and density estimation was emphasized. An introduction to GPR principles was then provided, including basic EM wave theory and typical GPR system composition. Furthermore, the traditional methods of measuring AC pavement thickness and density were described, including the surface reflection method, the TWTT method, and the ALL model. Finally, the existing super-resolution techniques were briefly reviewed with more details to follow in subsequent chapters.

CHAPTER 3: GPR IMAGING AND RECONSTRUCTION AND APPLICATION ON DRAINAGE PIPE EVALUATION

3.1 Background and Objective

This chapter presents an overview of the generic GPR imaging and reconstruction technique. The GPR target imaging forward problem is a linear transformation under certain assumptions, and the reconstruction of GPR targets is a classic linear inversion problem. The general 2-D imaging and reconstruction equations will be derived. The problem of 1-D AC pavement imaging is then a special case of the general imaging/reconstruction problem.

In section 3.2, the GPR imaging forward problem will be formulated. In section 3.3, different GPR image reconstruction techniques will be discussed. In section 3.4, the GPR image reconstruction methods discussed in section 3.3 will be applied to a case study: a drainage pipe condition assessment. Section 3.5 summarizes the chapter.

3.2 GPR Imaging

A GPR transmitter antenna sends EM waves toward the ground and the EM waves are reflected from the targets. The GPR receiver antenna then receives the reflected signal. The GPR target can be anything that has an impedance contrast with the surrounding environment, such as metal objects or air voids.

The processing of general synthetic aperture radar data can be found in the literature (Soumekh 1999). As a special type of radar, GPR captures images of three-dimensional targets into a radargram by moving the transmitter/receiver along a straight line. The target is defined by its impedance property. The radargram is a 2-D image, with its vertical dimensional being the reflection time, or fast time, and the horizontal dimension being the trace number. The trace number represents the signal collection time, or the slow time. An example of the GPR imaging is shown in Figure 3-1. In this example, two rebars embedded in concrete were scanned by a monostatic GPR system with central frequency of 900 MHz, modeled using a FDTD simulation. The obtained radargram shows two hyperbolas, representing the reflection from rebars, as well as a horizontal line, which is the direct coupling pulse. The antenna is assumed to be ground-coupled so there is no ground surface reflection.

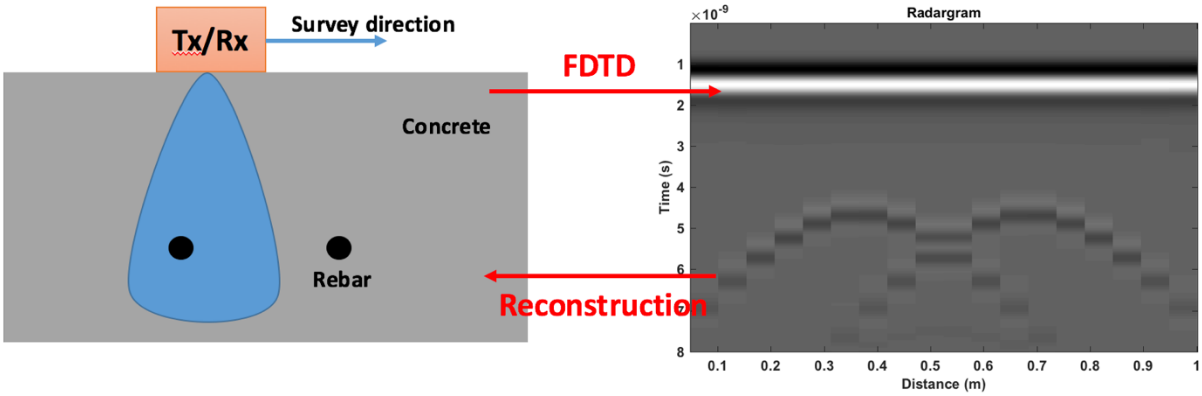

Figure 3-1 GPR imaging of rebars embedded in concrete

The general GPR imaging process is described by Maxwell's equations (Jin 2011). However, under certain assumptions, the imaging scheme can be simplified:

1) The first assumption made in this study is that the target is two-dimensional. This reduces the transverse dimension and greatly reduces the problem complexity.
2) The second assumption is that multiple reflection can be neglected. This assumption is true when the targets are placed far away from each other and there is no target that "shadows" other targets. This also ensures that the target space is sparse.
3) The third assumption is that the targets are thin, in the sense that the dimensions of the targets are small compared with the EM wavelength (i.e., a target dimension of less than a tenth of the EM wavelength).

Under these assumptions, the GPR imaging system is linear (Soldovieri 2011). Another way to explain the linearity is that the radargram is simply the superposition of all radargrams generated by each of the single point targets in the target space.

It is easiest to consider the GPR imaging process in the vector space signal processing content, as shown in Figure 3-2. First, we begin with a 2-D target, such as the one shown in Figure 3-1. We then vectorize the image by stacking the columns of the image to get an input vector $\vec{x} \in X$, where vector space X is the span of all possible vectors $\vec{x}$. Using the same technique, the 2-D radargram from Figure 3-1 can also be vectorized as a vector $\vec{y} \in Y$. Both input $\vec{x}$ and output $\vec{y}$ are in discrete domains with certain discretization steps that meet the Nyquist sampling criteria (i.e., the sampling frequency is at least twice that of the highest frequency band-limited signal) to prevent aliasing. The linear system serves as the transfer function between the input vector space X and the output vector space Y. Because the system is assumed to be linear, it can be represented by a matrix $\boldsymbol{H}$, with the input and output having the following simple relationship:

$$\vec{y} = \boldsymbol{H}\vec{x}. \tag{3-1}$$

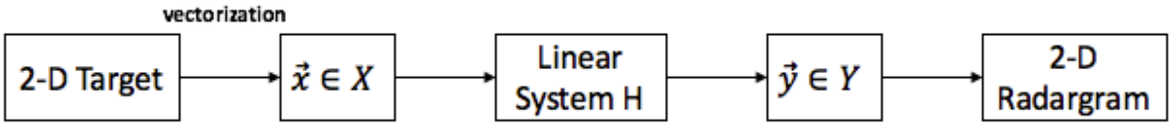

Figure 3-2 GPR imaging of 2-D target under linearity assumptions

The system matrix $\boldsymbol{H}$ is determined by the excitation source, attenuation factor and impedance of the media, and the dimension of both input and output vector space. Another way to obtain matrix $\boldsymbol{H}$ is through simulation; i.e., using FDTD to simulate the single radargram generated by each of the pixel in the input space. The latter method is more accurate; however, this can be extremely tedious when the input space is highly dimensional. Therefore, in the following drainage pipe example, we will use the first method to generate system matrix $\boldsymbol{H}$.

3.3 GPR Image Reconstruction

3.3.1 Migration

Under the GPR imaging scheme described in the section above, the objective was to find the GPR target from the obtained radargram. Considering the aforementioned assumptions, this is a linear inverse problem: find $\hat{\vec{x}}$ that can approximate $\vec{x}$. In order to do this, a linear inverse operator was established, such that:

$$\hat{\vec{x}} = \boldsymbol{H}^{*}\vec{y}. \tag{3-2}$$

Note that here we didn't follow the mathematical convention: $H*$ is not the complex conjugate of matrix *H,* but a matrix symbol to represent the inverse operator we need. The easiest solution to this problem is to select the inverse operator to be the adjoint operator:

$$\boldsymbol{H}^{*} = \boldsymbol{H}^{\boldsymbol{T}}. \tag{3-3}$$

Migration is a method commonly used in seismic wave reconstruction (Gazdag and Sguazzero 1984). The migration method refers to a series of similar methods—such as Kirchhoff migration (Bleistein and Gray 2001), Hagedoorn migration (Bleistein 1999), pre-stack migration (Berkhout 1986), and f-k migration (Gilmore et al. 2006)—which was demonstrated to be equivalent to the synthetic aperture radar technique shown in Soumekh (1999). Those migration techniques are equivalent to the adjoint operator shown in equation (3-3), which projects each pixel in the radargram space to the target space pixels, which contribute to that pixel in the radargram space.

A practical way to implement the migration technique is to use the synthetic aperture focus technique (SAFT; Gilmore et al. 2006). The procedure is summarized below:

1) Remove the radargram background (direct coupling) to obtain multiple traces (Figure 3-3(a)).
2) For each trace, convert time to distance and generate the reflection "circles" (Figure 3-3(b)). This step projects the radargram data back to the corresponding target space.
3) Superpose all circles to generate the desired target (Figure 3-3(c)).
4) Perform image thresholding (Figure 3-3(d)).

The migration algorithm has a complexity of O(n).

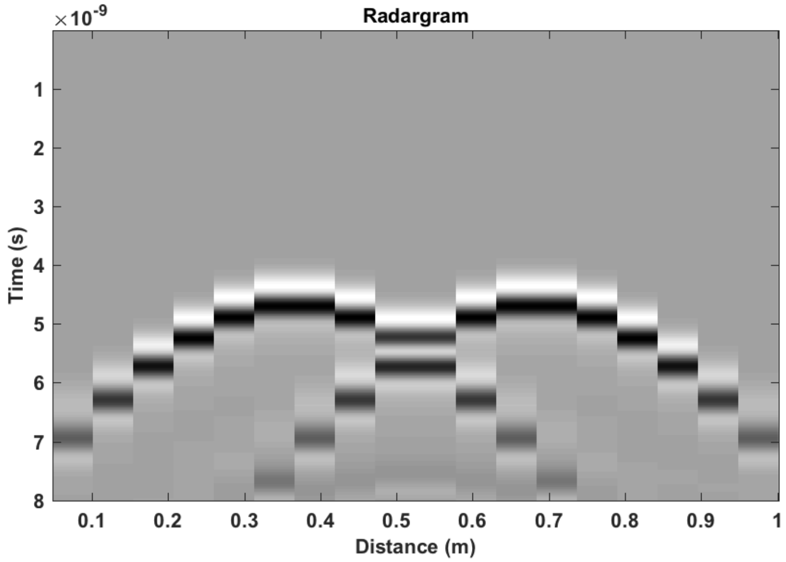

(a)

Figure 3-3 SAFT technique procedures: (a) Radargram after removal of direct coupling pulse; (b) "circle" generated by one of the trace; (c) superposition of all "circles"; (d) image thresholding.

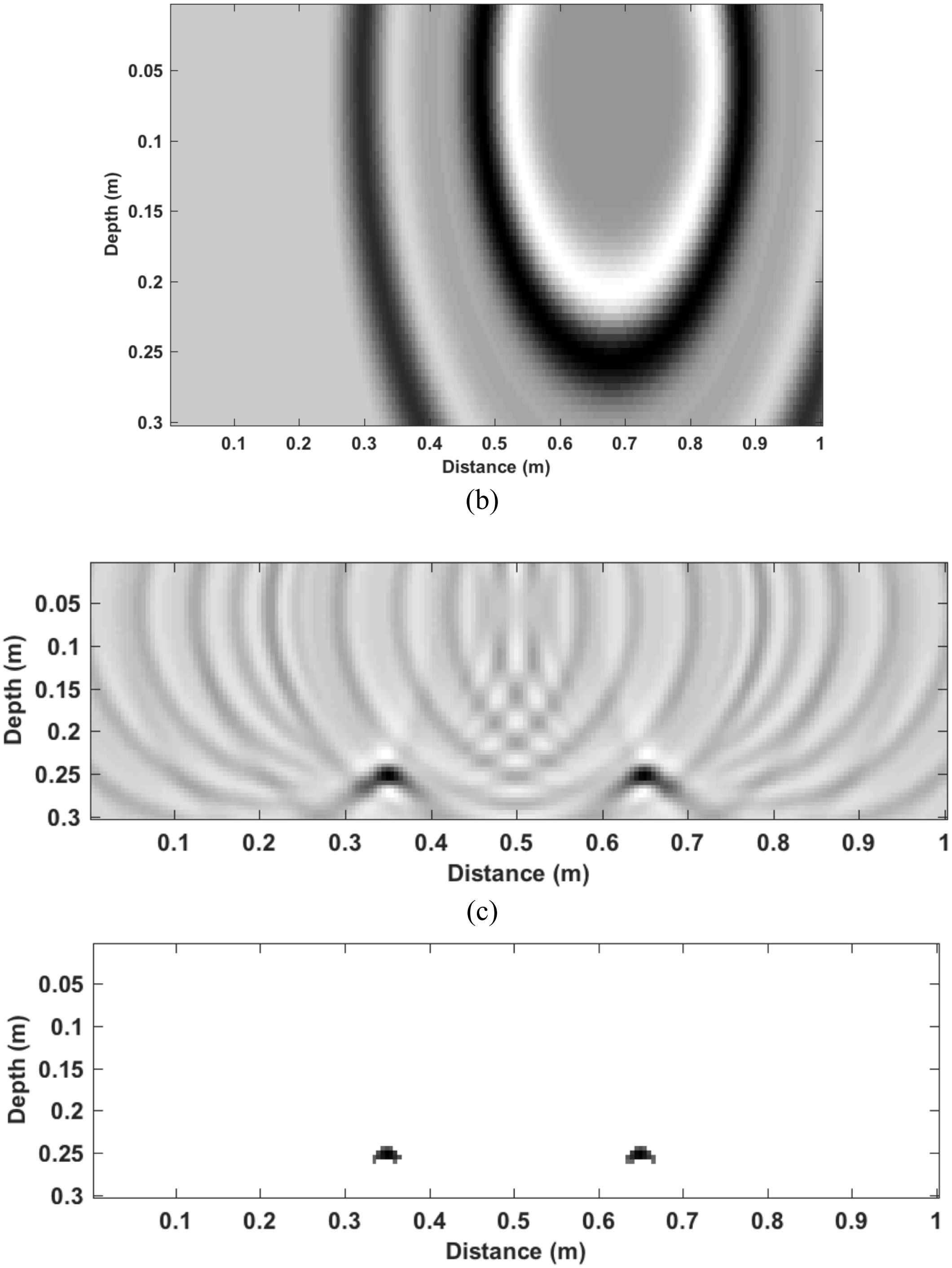

(b)

(c)

(d)

Figure 3-3 (cont.)

3.3.2 Sparse reconstruction

The intuitive way to find the exact target vector $\vec{x}$ from Equation (3-1) is to find the inverse of matrix H:

$$\boldsymbol{H}^{*} = \boldsymbol{H}^{-1}. \tag{3-4}$$

However, system matrix H is not always an invertible square matrix. An alternative way is to find the minimum square error (MSE) solution:

$$\hat{\vec{x}} = \boldsymbol{argmin}\{||\boldsymbol{H}\vec{\boldsymbol{x}} - \vec{\boldsymbol{y}}||^{2}\}, \tag{3-5}$$

where $||*||$ represents the L-2 norm and “argmin” means to find the argument x which minimizes the inner expression. The resulting inverse operator is given by the pseudo-inverse of system matrix H:

$$\boldsymbol{H}^{*} = (\boldsymbol{H}^{T}\boldsymbol{H})^{-1}\boldsymbol{H}^{T}. \tag{3-6}$$

However, the size of matrix H is too large to invert directly. If the input space has a dimension of 20,000—i.e., the target image has 20,000 pixels—and the output space has a dimension of 20,000, matrix A will be a 20,000 x 20,000 matrix. Inverting such a matrix will require a large amount of time since matrix inversion (using Gauss–Jordan elimination) has a complexity of $O(n^{3})$. There are algorithms that can solve the pseudo-inverse more efficiently: e.g., general singular value decomposition (GSVD). The detailed derivation can be found in Aster et al. (2013). In addition, matrix H is ill-posed. A small perturbation in the output $\vec{y}$ (e.g. noise) will result in huge fluctuation in the reconstructed target $\hat{\vec{x}}$ and, therefore, regularization is needed. There are several regularization methods available. A common method is the Tikhonov regularization:

$$\hat{\vec{x}} = \boldsymbol{argmin}\{||\boldsymbol{H}\vec{\boldsymbol{x}} - \vec{\boldsymbol{y}}||^{2} + \boldsymbol{\alpha}||\boldsymbol{L}\vec{\boldsymbol{x}}||^{2}\}, \tag{3-7}$$

where α is the regularization parameter, L is a matrix with full rank. The matrix L can be chosen as an identity matrix, first-derivative matrix, and second-derivative matrix, etc.; the corresponding regularizations are called the zeroth-, first-, and second-order Tikhonov regularization, respectively.

Sparse reconstruction regularization was used in this study because the GPR target space is sparse by nature (see second assumption in Section 1). Since the L-0 norm calculates the number of non-zero elements in a vector, the following L-0 norm regularization guarantees that the solution has a minimum number of non-zero elements:

$$\hat{\vec{x}} = \boldsymbol{argmin}\{||\boldsymbol{H}\vec{\boldsymbol{x}} - \vec{\boldsymbol{y}}||^{\boldsymbol{2}} + \boldsymbol{\alpha}||\vec{\boldsymbol{x}}||_{\boldsymbol{0}}\}. \tag{3-8}$$

It was found that when the input vector is sparse (which is the case in this study), the total variation will also give the sparse solution (Ramirez et al 2013):

$$\hat{\vec{x}} = \boldsymbol{argmin}\{||\boldsymbol{H}\vec{\boldsymbol{x}} - \vec{\boldsymbol{y}}||^{\boldsymbol{2}} + \boldsymbol{\alpha}||\vec{\boldsymbol{x}}||_{\boldsymbol{1}}\}. \tag{3-9}$$

In this study, total variation regularization was used because it is easier to implement due to the convexity of the problem.

There are many ways to solve the total variation problem, including the iteratively reweighted least squares (IRLS) method (Aster et al. 2013). In this study, the spectrum projected gradient method (SPG) was used due to its efficiency (Van Den Berg and Friedlander 2008). Equation (3-9) can be rephrased as the LASSO (least absolute shrinkage and selection operator) problem (Van Den Berg and Friedlander 2008):

$$\hat{\vec{x}} = \boldsymbol{argmin}\{||\boldsymbol{H}\vec{\boldsymbol{x}} - \vec{\boldsymbol{y}}||^{\boldsymbol{2}}, \boldsymbol{subjected\ to}\ ||\vec{\boldsymbol{x}}||_{\boldsymbol{1}} \leq \boldsymbol{\tau}\}, \tag{3-10}$$

where τ is a parameter associated with the regularization parameter in equation (3-9). The procedure of the SPG algorithm is then summarized in the following:

1) Find ∇_x, the gradient of $||A\vec{x} - \vec{y}||^2$ w.r.t. $\vec{x}$.

2) Gradient descent: $\vec{x}_{n+1} = \vec{x}_n - \alpha \nabla_x$, where α is the step length.

3) Project $\vec{x}_{n+1}$ to the one-norm ball of radius τ to update $\vec{x}_{n+1}$. The detailed procedure of this one-norm projection is explained in (Van Den Berg and Friedlander 2008).

4) Iterate the procedure until small enough error is achieved.

The SPG algorithm has a worst-case complexity of $O(n \log n)$.

3.4 Application of GPR Image Reconstruction on Drainage Pipe Evaluation

3.4.1 Introduction to drainage pipe condition assessment

Drainage design is important for the operation of traffic on highway or airport pavement. Malfunction of the drainage pipes can cause saturation of the pavement, resulting in serious flooding issues, a decrease in strength or stability, and pavement deficiencies including pumping, swelling, frost damage, and aggregate stripping. These issues jeopardize a pavement's structural ability to support heavy axle loads and decreases its functionality. A typical pavement drainage system consists of a permeable drainage layer to drain water beneath the pavement, a collector system to drain water out of pavement, an outlet, and a filter layer to prevent fine particles from entering the permeable layer (CDOT, 2015). Drainage pipes are a common collector system. The quality of drainage pipes can be impaired due to poor installation and lack of maintenance. Therefore, it is necessary to monitor the condition of the drainage system to ensure that they are well positioned and not clogged (by soil or foliage).

Once the drainage pipes are built, it is difficult to track their condition without excavation as they are buried deep under the pavement. There are, however, several non-destructive ways to inspect drainage pipes. The most common approach is to use a pipe crawler, or a pipe crawling inspection robot (Roman et al. 1993). The pipe crawler is a computer with multiple sensors, including a closed circuit television (CCTV) system and a fisheye camera. The pipe crawler is remotely controlled from the ground and moves inside the pipe collecting drainage pipe information, including cracking, clogging, and corrosion.

Using pipe crawlers greatly reduces the danger involved in human inspection. A fully autonomous pipe crawler system called “KANTARO” was developed in Japan and operates without the need for any human navigation (Nassiraei et al. 2006). However, the inspection speed of the pipe crawler is not fast enough to survey large distances of pipes. Another sensing method is the laser-based scanning system, which uses structured light as its source. The laser-based scanning system can provide a more accurate measurement of the shapes and defects of the pipes (Sinha 2003). Other NDT techniques have also been used to monitor drainage pipe conditions, including ultrasonic inspection, eddy current testing, infrared sensing, and acoustic emission mentoring (Sinha 2004). However, those methods provide less accurate results when the pavement structure is not so uniform. An overview of different NDT methods to assess drainage pipe condition can be found in Duran (2002).

All NDT techniques mentioned above require access to the drainage pipes, usually provided by sending a robot. This is sometimes impossible, as in the case where manholes are not accessible or the drainage pipes are filled with water or soil. An alternative NDT method is GPR.

GPR has already been used in drainage pipe detection. Allred et al. (2004a) used four methods (geomagnetic surveying, EM induction, resistivity, and GPR) to detect buried drainage pipes and concluded that only GPR provided good performance. Another study conducted by the same group using different central frequencies showed that GPR can be used to detect drainage pipes effectively under different moisture and temperature conditions (Allred et al. 2004b). Zeng and McMechan (Zeng and McMechan 1997) used ray-based GPR simulation data on drainage pipes and found that different GPR data characteristics can help identify the material, size, content, fluid levels, and shapes changes of the drainage pipe. The study was based on characterization of the hyperbolic shaped GPR signal done by humans. Youn and Chen (2004) successfully automated this process by developing a two-step neural network algorithm to transform the obtained hyperbola to actual drainage pipe image. With this technique, the accuracy of detecting drainage pipes increases, because operator experience is no longer needed for the identification of drainage pipes. The drawback of this method, as with any machine learning algorithm, is that it requires a large amount of GPR data and associated ground truth to train the neural network model.

Image reconstruction is an alternative way to recover the original drainage pipe target. In this section, both migration reconstruction and sparse reconstruction will be applied on FDTD simulated GPR signals to reconstruct drainage pipes with different sizes, locations, and conditions. The results of both methods are compared in terms of accuracy and computation speed.

3.4.2 FDTD modeling

Computational electromagnetics, which can solve Maxwell's equations numerically, is an important tool for modeling EM phenomenon in radio frequency. There are generally two methods of calculating computational electromagnetics: the time-domain method and the frequency domain method. Frequency methods are good for dispersive media applications, while time-domain methods are good for broadband problems with only a few excitations (Jin 2011). Due to the characteristics of GPR pulses, a time-domain method, FDTD method, and an open source program, GPRMax (Warren et al. 2016), were used in this study to model GPR signals reflected from two drainage pipes embedded in concrete pavement.

Cases with more drainage pipes are not considered in this study because of the large computational cost of the sparse reconstruction algorithm. The two drainage pipes in this study were 0.2 m apart and had different depths, sizes, and contents. The seven models are summarized in Table 3.1. The diameters of the two drainage pipes ranged between 6 cm and 10 cm, with a depth ranging between 0.11 m and 0.15 m. In practice, pavement drainage pipes are usually buried deeper. For this study, a shallower depth was selected because a deeper drainage pipe would generate a larger model (in terms of number of pixels in the target space) and would increase the computational time of the reconstruction algorithms, especially for the sparse reconstruction algorithm. The drainage pipes were assumed to be occupied by air, water, or soil, with relative permeabilities (or dielectric constants) of 1, 82.4, and 30, respectively. Since the pipe wall (clay or concrete) is usually thin compared with the EM wavelength, wall thickness was neglected. The study focused on estimating the diameter and the depth of the drainage pipes, and determining whether the drainage pipes were empty or occupied by water or soil.

Table 3-1 FDTD Models of Drainage Pipes

Model No.	Diameter (m)	Depth (m)	Content
1	0.1	0.13	Air
2	0.1	0.13	Water
3	0.1	0.13	Soil
4	0.08	0.13	Air
5	0.06	0.13	Air
6	0.06	0.11	Air
7	0.06	0.15	Air

An example configuration of the drainage pipes (Model 1) is shown in Figure 3-4. Concrete was assumed to be homogeneous, its dielectric constant was assumed to be 7, and its conductivity assumed to be 0.01 S/m. The GPR transmitter and receiver were placed 5 cm apart near the concrete surface. The GPR system is ground-coupled, so there is no surface reflection in the obtained radargram. The GPR antenna is broadband with central frequency of 900 MHz. The excitation source is Ricker wavelet. The spatial step of the FDTD model was set to 5 mm in both the x and y direction. The time step dt was set to $1.179*10^{-11}$ sec, which was determined using the following equation:

$$\mathrm{d}t \leq \frac{1}{c\sqrt{\frac{1}{(\mathrm{d}x)^2}+\frac{1}{(\mathrm{d}y)^2}}}, \tag{3-11}$$

where $\mathrm{d}x$ and $\mathrm{d}y$ are the spatial discretization steps in horizontal and vertical directions, respectively, and $\mathrm{d}t$ is the time step.

The radargram obtained from the FDTD simulation is shown in Figure 3-5.

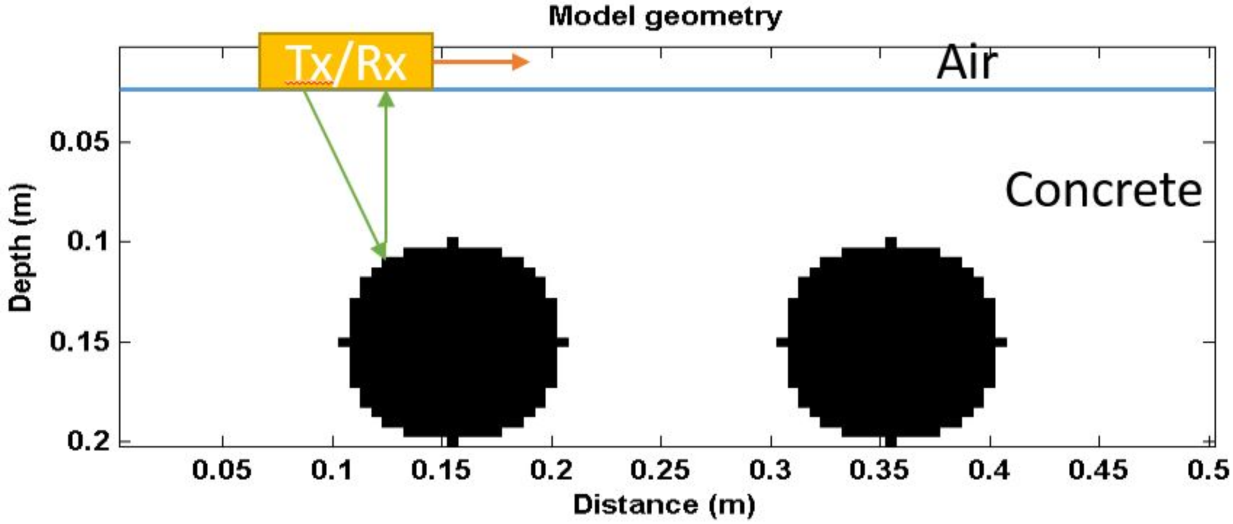

Figure 3-4 2-D target model: Two drainage pipes embedded in concrete pavement.

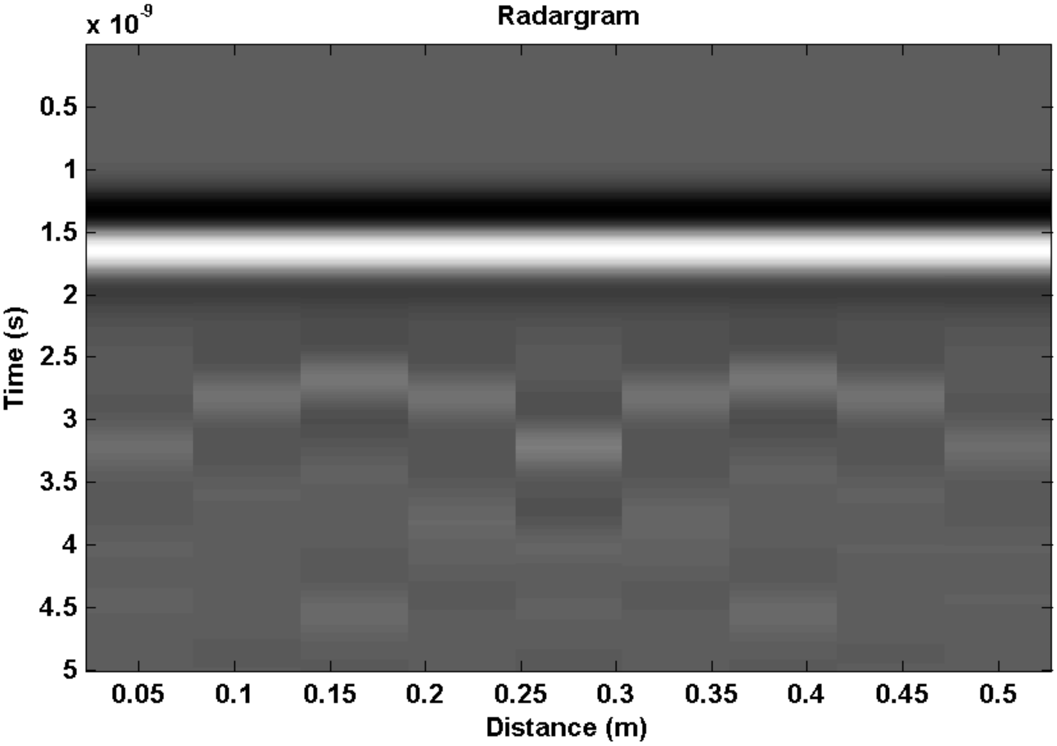

Figure 3-5 Radargram from FDTD simulation.

3.4.3 Results

Using both migration and the sparse reconstruction technique, the results of the reconstructed targets are presented in this section. The drainage pipe contents were obtained from the reconstructed images; the depths and diameters of the drainage pipes were estimated and compared with the true model. The computational time of both methods was also compared.

Figures 3-6 and 3-7 show the reconstructed targets from Models 1 and 2 using both the migration and the sparse reconstruction technique. First, we observed that both migration and the sparse construction methods could only reconstruct the top part of the drainage pipes. This is because of the violation of the second and the third assumption: the drainage pipes are thick, and the EM waves cannot penetrate the structure to reach the bottom part of the pipes. Second, we noted that when the drainage pipes are empty (i.e., occupied by air), the reconstructed image has positive pixel values; however, when the drainage pipes are occupied by soil or water, the target has negative pixel values. This makes sense if we consider the dielectric constant contrast of the target and the ambient concrete and the EM wave reflection law. We can then estimate the content of the drainage pipes: if the target has positive pixel values, the pipe is empty (Figure 3-6); if the target has large negative pixel values, then the pipe is occupied by water (Figure 3-7); if the target has small negative pixel values, the pipe is occupied by soil (Figure 3-8). The content estimation result is shown in Table 3-2.

The reconstruction performance of the two methods was also studied. The reconstructed images from both methods have artificial noise in the target because of violating the linearity assumption of the model. Specifically, the “inner pipe” shown in the sparse reconstruction could be due to multiple reflection inside the pipe or between adjacent pipes. The sparse reconstruction is nonetheless more accurate than the migration method. This is due to the fact that adjoint operator cannot give an exact reconstruction of the input vector.

In addition, the migration method always requires selecting the proper threshold and is, therefore, not a deterministic algorithm, while the sparse reconstruction is an automatic algorithm.

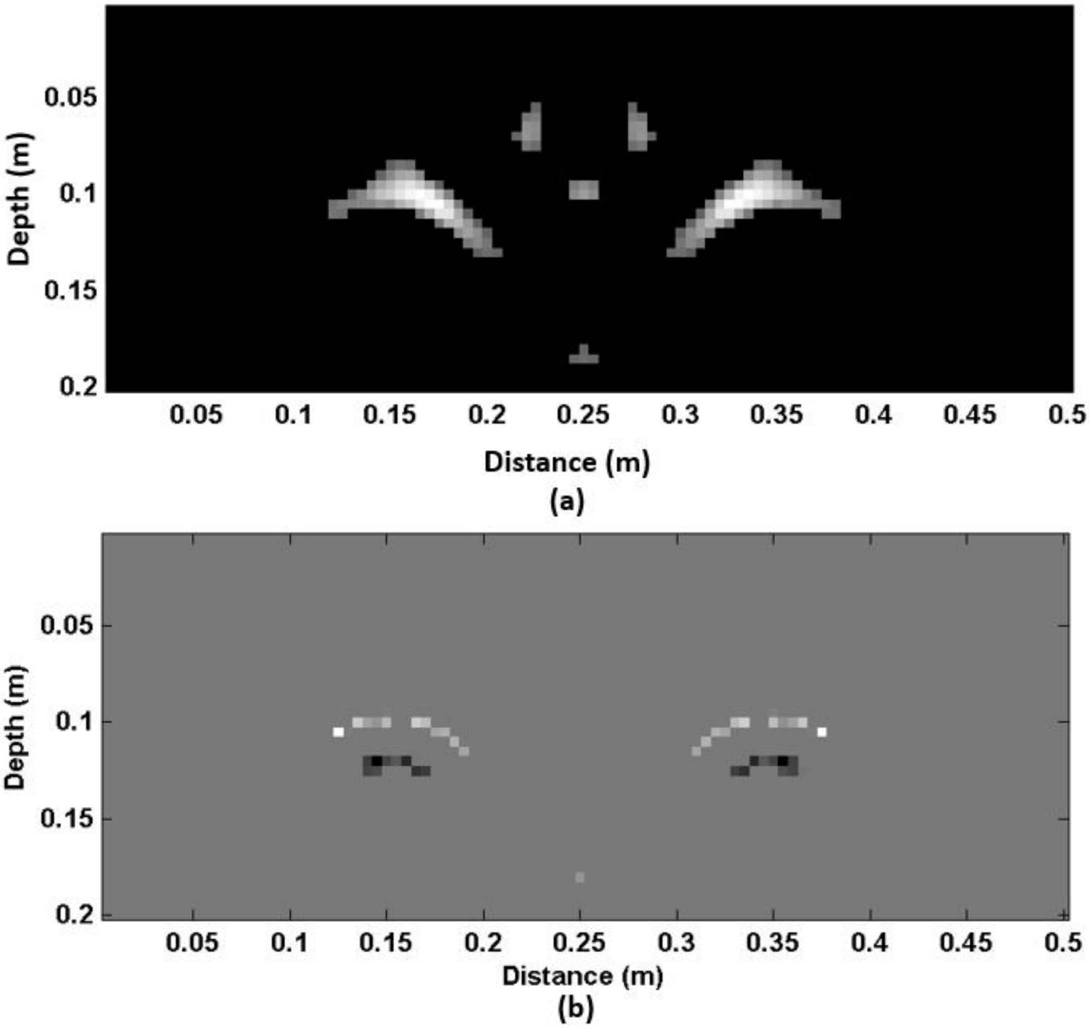

Figure 3-6 Reconstructed image of Model 1: (a) Migration reconstruction, and (b) sparse reconstruction

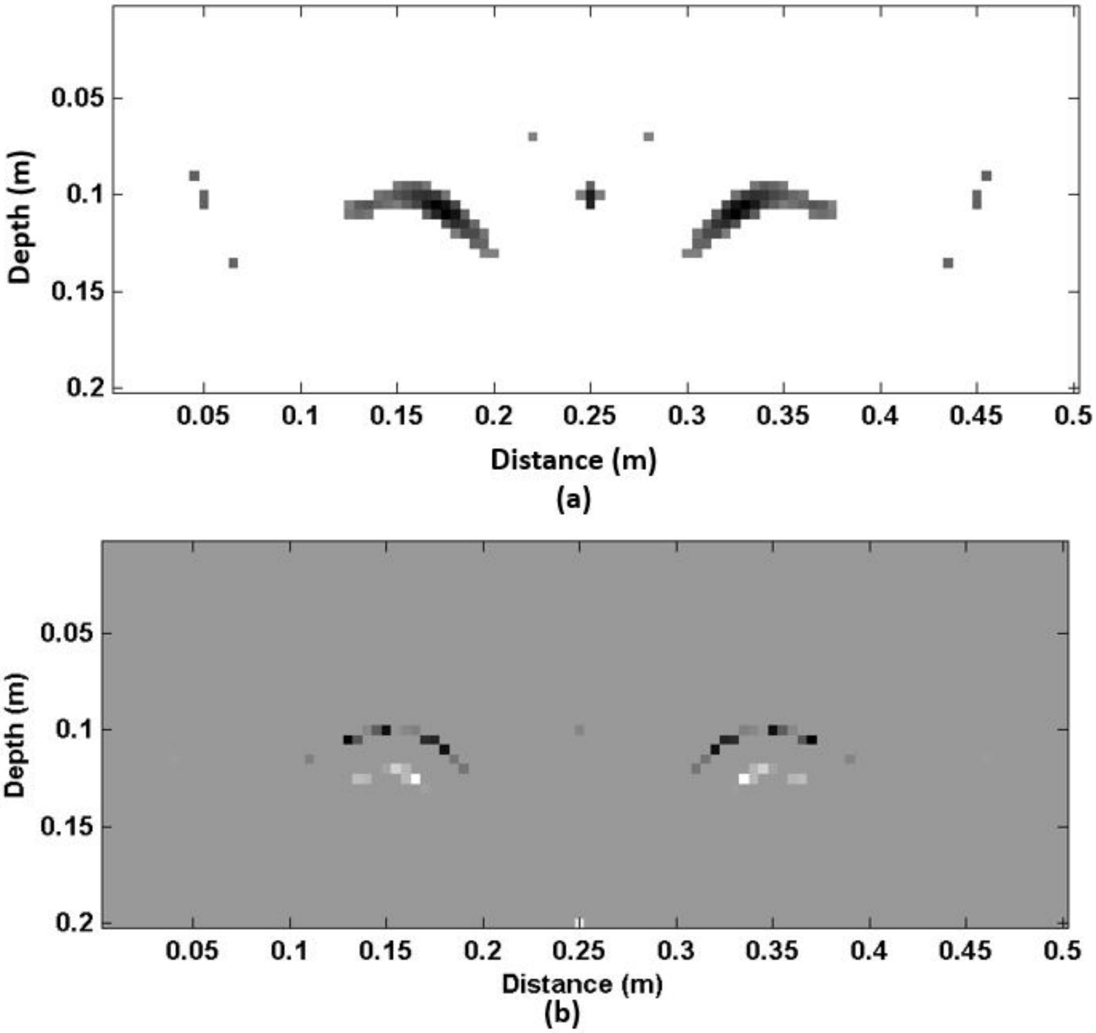

Figure 3-7 Reconstructed image of Model 2: (a) Migration reconstruction, and (b) sparse reconstruction.

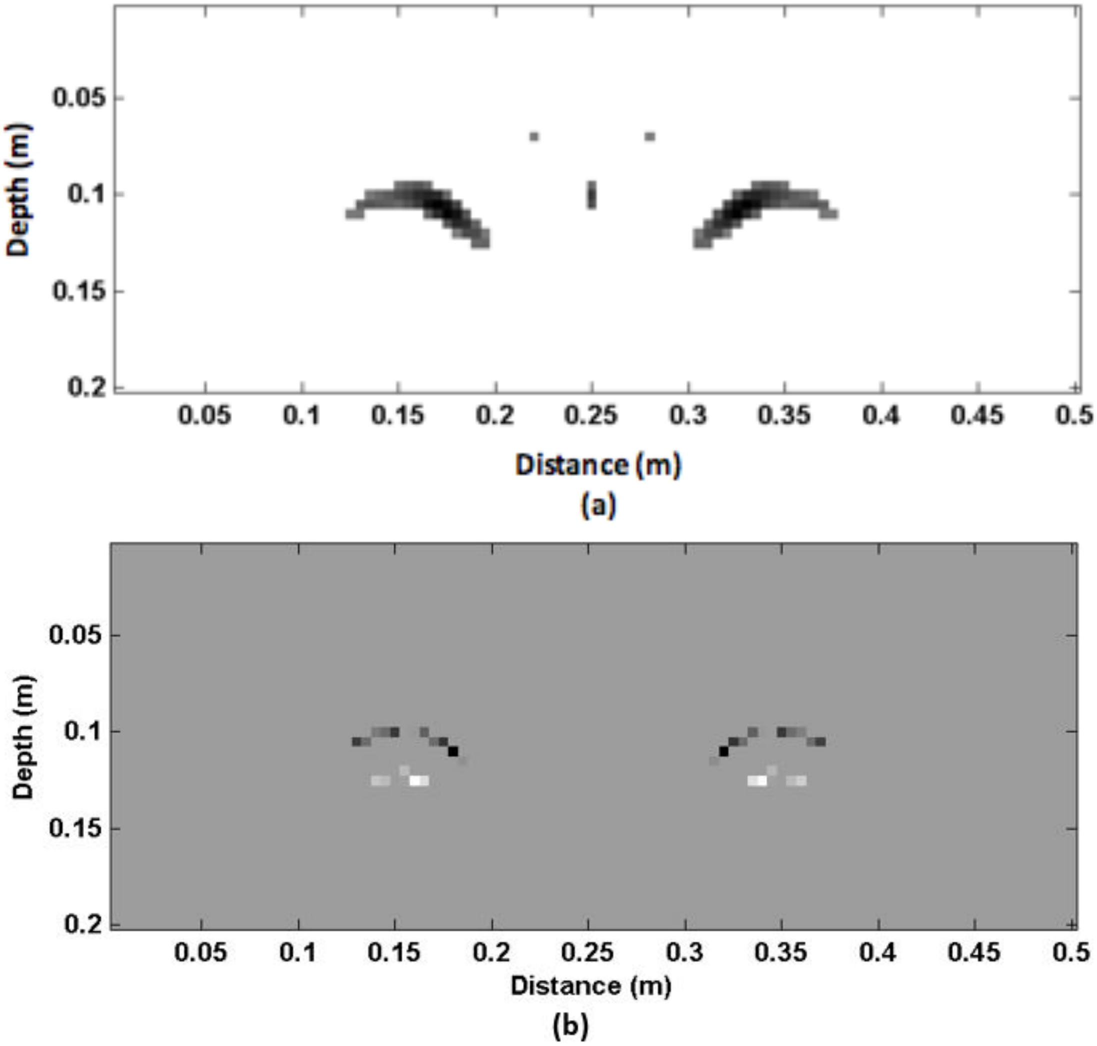

Figure 3-8 Reconstructed image of Model 3: (a) Migration reconstruction, and (b) sparse reconstruction.

The reconstruction of Models 3 to 6 show similar results as with Models 1 to 3, and is therefore not presented in this dissertation. From the two examples above, we noticed that we can easily find the pipe depth and diameter from the sparse reconstructed result; however, for the migration reconstructed results, a quantitative determination of the pipes parameters is made difficult because of the inaccurate reconstruction. Table 3-2 shows the depth and diameter estimation of the sparse reconstruction methods. The estimation process is illustrated in Figure 3-9. The radius of the pipe is estimated by first finding the center of the circle (which is an equal distance from all points on the circle in a MSE sense), then finding the distance from center of the circle to the top on the circle (we can also average all radii to get a more accurate estimation). The depth of the drainage pipe is the distance between the pipe center and the antenna position. The cover depth of the pipe can be then calculated by subtracting the pipe radius from the depth of the pipe.

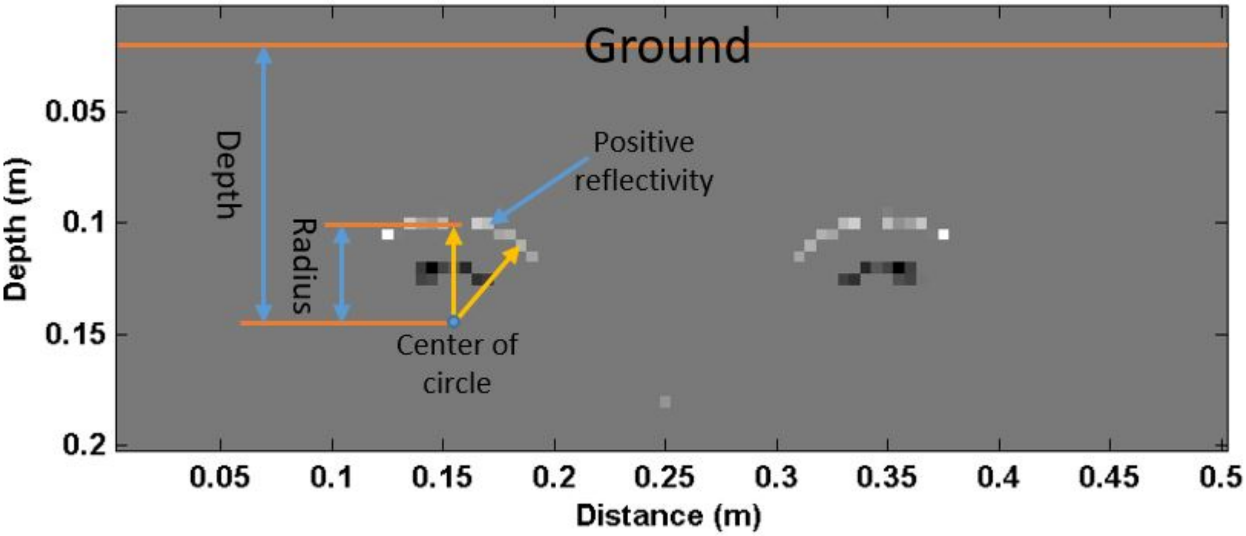

Figure 3-9 Estimation of drainage pipe size and location.

Table 3-2 Depth, Diameter and Content Estimation of the Reconstructed Pipes Using Sparse Reconstruction and Computation Speed of Both Methods

Model No.	Diameter (m)	Depth (m)	Content	Computation Time (s)	
				Migration	Sparse Reconstruction
1	0.110	0.135	Air	0.0242	2.10
2	0.110	0.135	Water	0.0212	1.30
2	0.110	0.135	Soil	0.0231	1.00
3	0.090	0.135	Air	0.0246	3.30
4	0.07	0.130	Air	0.0309	1.70
5	0.07	0.150	Air	0.0261	2.80
6	0.07	0.110	Air	0.0206	1.10

Table 3-2 shows that the estimated pipe diameters and depths are very close to the ground truth shown in Table 3-1. The absolute error is within 0.01 m. Considering that the model is discretized by steps of 0.005 m, the error is within two steps. Unlike thin 2-D targets, such as rebars, the MSE of the original target and the reconstructed targets cannot be computed, since we are only reconstructing the top surface of the drainage pipes instead of the full target image.

The last two columns in Table 3-2 show the computation time of both methods using a computer with an Intel i7 processor. The computation time of sparse reconstruction is more than 10 times that of the migration method. This is mainly because of the computational complexity difference of the two reconstruction methods: the migration method has time complexity of O(n), and the sparse reconstruction has worst-case complexity of $O(n \log n)$. For a larger model, the sparse reconstruction method requires even more computation time than the migration method.

For illustration purposes, three additional models are presented where the two pipes have different conditions. Detailed parameters are shown in Table 3-3. The thresholds of left and right pipes are different, so step 4 of the migration algorithm was not performed. The same numerical estimations of pipe diameter and depth used in the aforementioned models were used in these three additional models.

Figure 3-10 shows that the left pipe has positive pixel values, while the right pipe has large negative pixel values. This suggests that the left pipe is empty, while the right pipe is filled with water. The pipe on the left has a smaller diameter and a larger depth. Similarly, the left pipe has positive pixel values and the right pipe has small negative pixel values (Figure 3-11). This suggests that the left pipe is empty, while the right pipe is filled with soil. Again, the pipe on the left has a smaller diameter and a larger depth. On the other hand, Figure 3-12 shows both pipes having negative pixels. The left one has a smaller absolute value, indicating it is filled with soil, while the right pipe is filled with water.

Table 3-3 Additional FDTD Models of Drainage Pipes for Two Different Pipes

Model No.	Left Pipe			Right Pipe		
	Diameter (m)	Depth (m)	Content	Diameter (m)	Depth (m)	Content
8	0.06	0.15	Air	0.08	0.13	Water
9	0.06	0.15	Air	0.1	0.11	Soil
10	0.08	0.13	Soil	0.1	0.11	Water

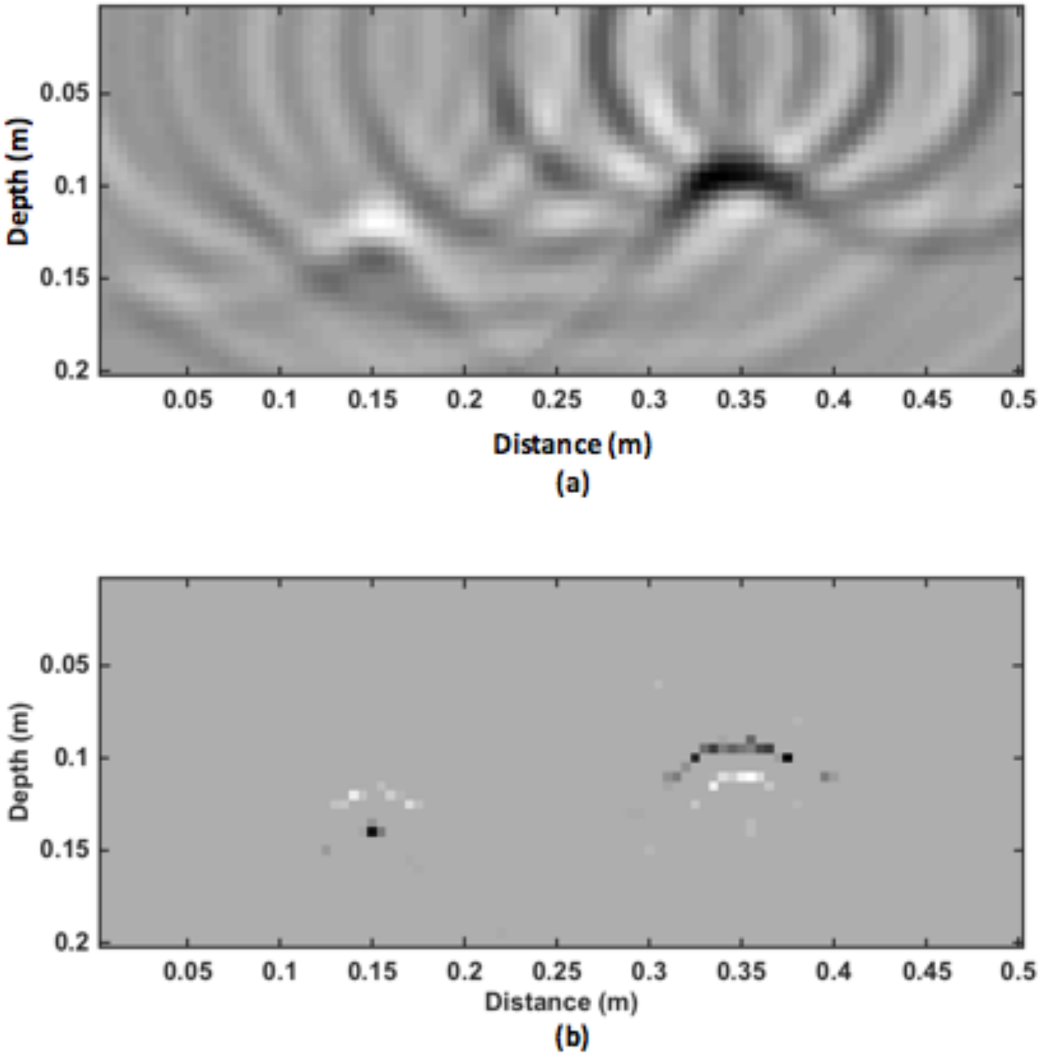

Figure 3-10 Reconstructed image of Model 8: (a) Migration reconstruction, and (b) sparse reconstruction.

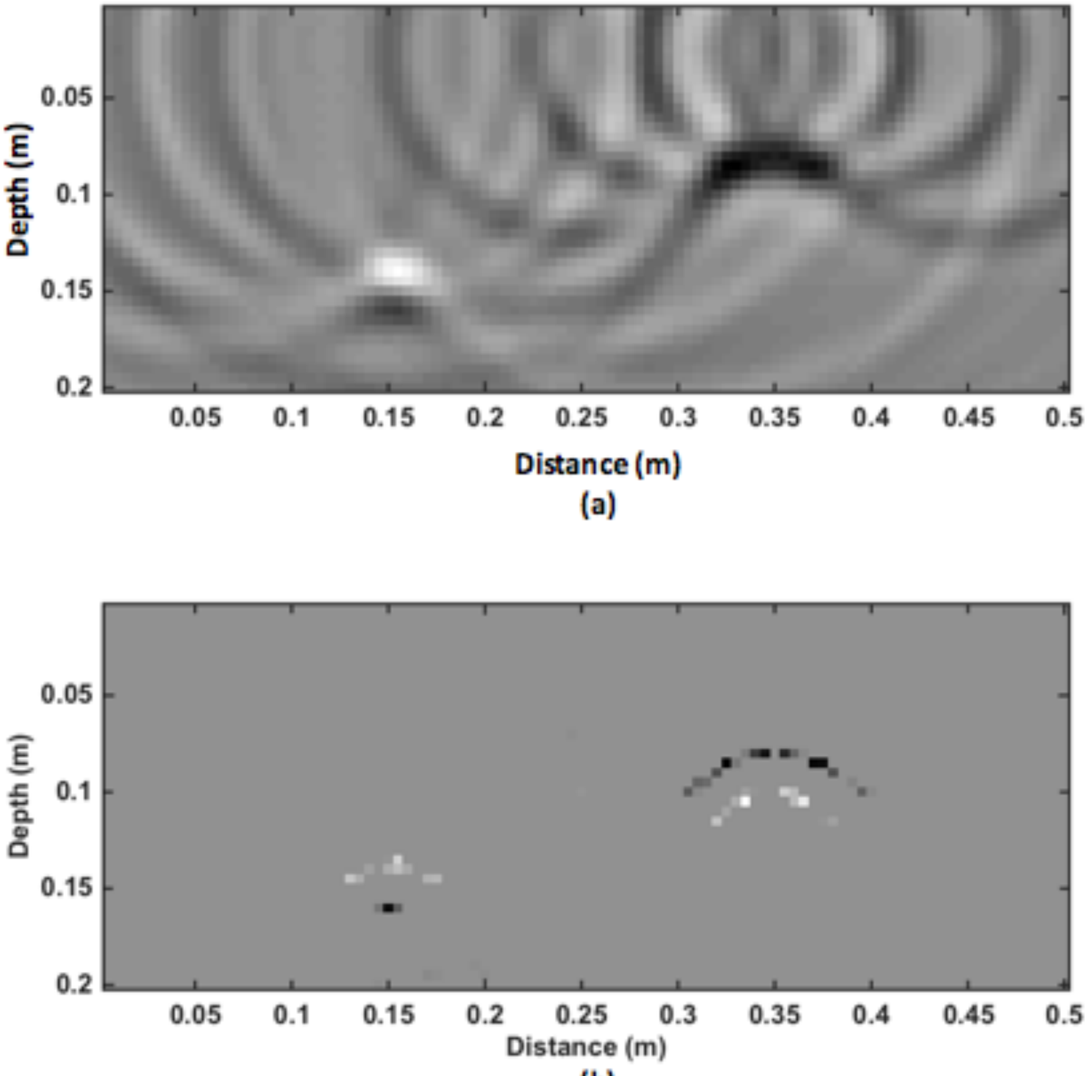

(a)

(b)

Figure 3-11 Reconstructed image of Model 9: (a) Migration reconstruction, and (b) sparse reconstruction.

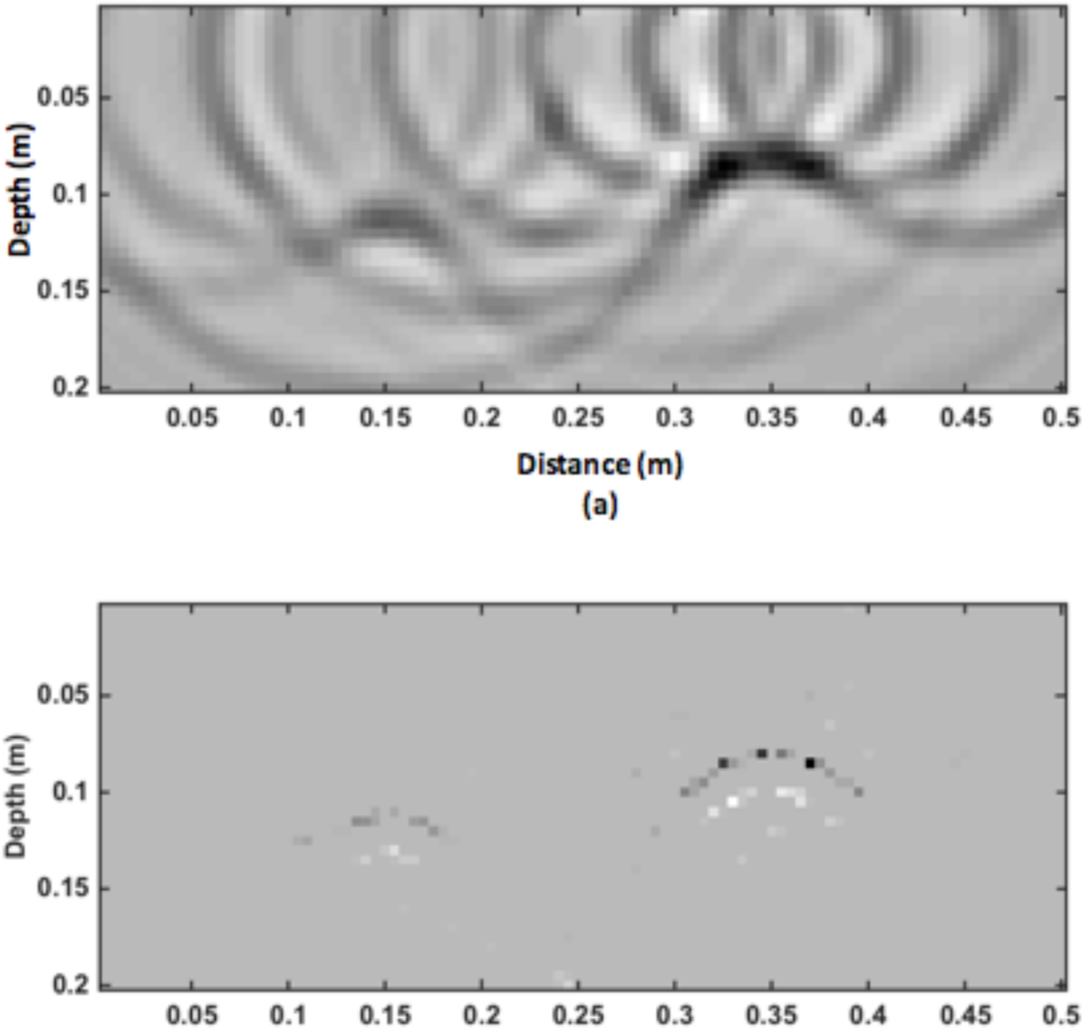

(a)

(b)

Figure 3-12 Reconstructed image of Model 10: (a) Migration reconstruction, and (b) sparse reconstruction.

3.5 Summary

In this chapter, the generic GPR imaging theory was discussed, and the forward imaging problem was demonstrated to be a linear problem under certain assumptions. Two linear inversion techniques were then developed, including migration and sparse reconstruction.

The FDTD simulation theory was described and an example of drainage pipe simulation was conducted. The simulated drainage models showed different condition parameters including locations, diameters, and contents. The proposed two image reconstruction techniques were then applied to the simulated GPR signal to reconstruct the drainage pipes under concrete pavement. The depth, diameter, and content of the drainage pipes were then estimated based on the reconstructed targets. The findings can be summarized as follows:

1) Both migration and sparse reconstruction can reconstruct 2-D targets when the linearity assumptions are met.
2) For drainage pipe reconstruction, both migration and sparse reconstruction can only reconstruct the top surface of the drainage pipes. This is due to the violation of the linearity assumption in GPR imaging.
3) SPG algorithm can be used to efficiently solve the LASSO problem.
4) Migration algorithms can effectively reconstruct the target, but require manually selecting a proper threshold. The drainage pipes content can be estimated based on the migration-reconstructed image.
5) Sparse reconstruction is more accurate than the migration algorithm, but it requires more computation time than the migration algorithm. The size and location of the drainage pipes can be accurately estimated based on the sparse reconstruction results.

In practice, migration better detects the presence of the drainage pipes and more efficiently estimates the content of the drainage pipes; the sparse reconstruction better estimates the location and size of the drainage pipes quantitatively.

As a continuation of the study, the recommendations for future studies are as follows:

1) The performance of both reconstruction methods need to be validated on real GPR signals collected from underground targets.
2) Targets of different shapes, sizes and depths need to be considered.

3) Reconstruction performance with different pavement structures, such as layered structures, needs to be studied.
4) Potential interference due to close proximity of targets need to be considered.

This chapter explains the general GPR imaging problem. Starting from here, the thin AC overlay thickness and density estimation problem can be solved using methods similar to those used for the two image reconstruction.

CHAPTER 4: DEVELOPMENT OF REGULARIZATION METHODS ON SIMULATED GPR SIGNALS TO PREDICT THIN AC OVERLAY THICKNESS

4.1 Background and Objective

This chapter presents the details of one of the proposed approaches to find thin AC overlay thickness, regularization method. The range resolution of GPR antenna signal is an important parameter in thin asphalt overlay thickness estimation. When the asphalt pavement thickness is comparable to the EM wavelength of the GPR signal, the GPR reflection from the pavement surface and the bottom of the surface layer may overlap. In such cases, our goal is to increase the resolution of the GPR signal, such that the reflections can be individually resolved.

In section 4.2, we'll first develop a mathematical model for GPR survey on two layered AC pavement, and then propose the four types of regularization algorithms, including Tikhonov regularization and total variation regularization. In section 4.3, the four regularization methods will be applied on simulated noisy GPR signals, and their performance will be evaluated. Section 4.4 summarizes this chapter.

4.2 Algorithm Development

4.2.1 Mathematical model

In this study, we consider two-layered AC pavement as shown in Figure 2-4, where the first layer is the surface binder, which is the thin overlay, and the second layer is the leveling binder, which could also be the old pavement. Here we assume that the reflection coefficient at ground surface, $-A_1/A_p$, is negative, and that the reflection coefficient at bottom of the surface binder, $-A_2/A_p$, is positive, as with the red arrows shown in Figure 2-4. The incident signal is Ricker wavelet type. A_1, A_2, and A_p are the reflection amplitude from the pavement surface, the bottom of the surface layer, and the copper plate, respectively.

A linear time-invariant system is a system that satisfies the following two properties:

- Linearity: a linear combination of the input will result in the linear combination of the corresponding outputs. For example, if the input $x_1(t)$ produces output $y_1(t)$, and input $x_2(t)$ produces output $y_2(t)$, then $a_1x_1(t) + a_2x_2(t)$ produces output $a_1y_1(t) + a_2y_2(t)$, where a_1 and a_2 are real scalars.
- Time-invariance: if we delay the input by some time interval, the output will be delayed by the same amount of time. For example, if $x_1(t)$ produces output $y_1(t)$, then $x_1(t + \Delta t)$ produces output $y_1(t + \Delta t)$.

It is easy to see that under the assumptions that AC is homogeneous, non-dispersive, and isotropic material, the asphalt pavement shown in Figure 2-4 is a linear time-invariant system: the input is the incident signal while the output is the GPR signal reflected from the pavement structure.

For a linear time-invariant system, the output signal is the convolution of the input signal and the system impulse response. In our case, the output signal y(t) is the convolution of incident signal x(t) and the pavement system impulse response h(t):

$$y(t) = h(t) * x(t) = \int_0^\infty h(t-u)x(u)du, \tag{4-1}$$

where y(t) is the pavement reflection signal, x(t) is the incident signal (usually Ricker wavelet), and h(t) is the impulse response. For a layered pavement system, h(t) simply consists of impulses at each layer interface, with amplitudes equal to the reflection coefficient at each layer interface, as shown by the red arrows in Figure 2-4. The impulse response h(t) contains the information we are interested in: the TWTT and the surface reflection amplitude. Therefore, we'll be able to calculate the asphalt overlay thickness and density once the impulse response is known. For GPR application, y(t) and x(t) are known from the pavement reflection and the copper plate reflection, while h(t) is unknown.

4.2.2 GPR signal resolution

If the pavement is thick, we will identify the reflection from the asphalt pavement surface and the bottom of the surface layer, and directly obtain the two-way travel time and surface reflection coefficient without any signal processing techniques. However, as stated in the "problem statement" section, when the layer thickness is thin compared to EM wavelength, the two pulses shown in Figure 2-4 will overlap with each other. Figure 4-1 illustrates this thin layer challenge.

Figure 4-1 shows the simulated output signal from a two-layer asphalt pavement model with different thicknesses. The incident signal in the simulation is the same as the one used by air-coupled antenna in this study. The incident signal is a Ricker wavelet with an arbitrary amplitude and an EM wavelength duration of 0.5382 ns. The dashed lines show the GPR signals which are generated by convoluting the incident GPR signal with Dirac delta functions at the surface and the bottom of the asphalt pavement layer. The amplitude of the Dirac delta functions represents the reflection coefficient that can be used to calculate the dielectric constant for each layer. The sign of impulses in Figure 4-1 are intentionally inverted for visualization purposes. For example, an impulse amplitude of the surface reflection of 0.3 means that $A_1/A_p = -0.3$; therefore, the dielectric constant ε_1 is 3.45, as calculated by equation 2-12. The locations and amplitudes of the Dirac delta function are simply assumed by the authors for the purpose of demonstration.

Figures 4-1(a) through 4-1(f) show the increase in layer thickness from 0.71 times the wavelength to 1.79 times the wavelength. For the Ricker wavelet-type of incident signal used in this study, the length of the wavelet is around twice the length of the EM wavelength. Figures 4-1(c), 4-1(d), 4-1(e) and 4-1(f) show that the two peaks can be seen directly because the thickness is relatively large; however, Figures 4-1(a) and 4-1(b) show that the second reflection is masked by the surface reflection, resulting in difficulties in obtaining the two-way travel time.

The two solid vertical lines in each figure represent the inverse of the assumed impulse responses at each layer interface. The amplitudes of these two impulses are $-A_1$ and $-A_2$, respectively, as shown in Figure 2-4. In Figure 4-1, the amplitude of the impulse responses is magnified to better show the locations of the surface and the bottom of the asphalt pavement layer.

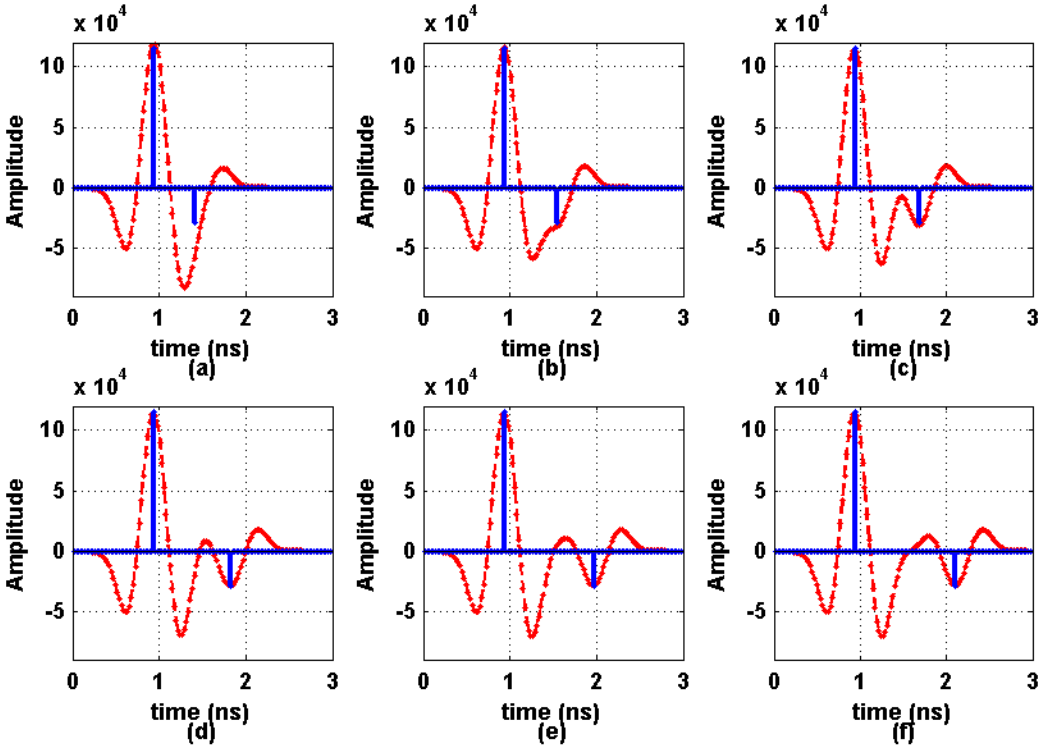

Figure 4-1 Pavement reflection (dashed) and impulse response (solid) for layer thickness which is a) 0.71 b) 0.93 c) 1.14 d) 1.36 e) 1.57 f) 1.79 times of the EM wavelength.

Thin layers present a challenge because GPR signals lack adequate range resolution. Radar resolution is an importation parameter for imaging (Soumekh 1999). The cross-range resolution (or azimuth resolution) of a radar describes its ability to resolve targets that are closely placed in angle, while the range resolution describes its ability to resolve targets closed placed in the range direction. This is shown in Figure 4-2, in which the round black circle represents general underground targets, such as rebar, drainage pipes, landmines, archaeological structures, and layered pavement. The cross-range resolution of a radar is usually determined by its antenna pattern: the larger the directivity of the antenna, the better the cross-range resolution. An example of the GPR antenna pattern is represented by the blue area shown in Figure 4-2. The range resolution of a radar is determined by the bandwidth of the antenna. Signals with a wider bandwidth have shorter pulse durations, allowing for target resolution at a closer distance. In extreme cases, signals of infinite bandwidth become impulse signals (or Dirac Delta functions) and have perfect range resolution. In practice, all signals are band-passed signals, and therefore have a nonzero pulse duration.

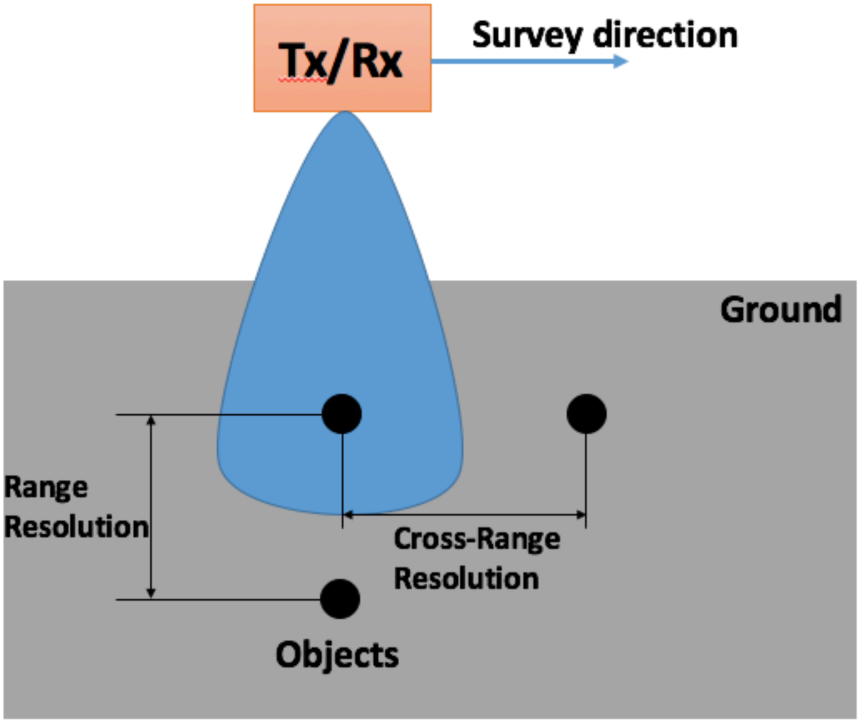

Figure 4-2 Illustration of range resolution and cross-range resolution of GPR

In the application of measuring asphalt layer thickness, whether using the conventional two-way travel time method or the XCMP method, the key factor determining GPR performance is the antenna range resolution, since the asphalt pavement layer can be considered a 1-D target which only varies in the vertical direction. Thus, it is preferable to use wide band antennas (e.g., horn antennas) or ultra-wide band antennas (e.g., bow-tie antennas) as GPR antennas (Stutzman and Thiele 2012).

There are many ways to characterize the range resolution of a signal. The most common method is to use Rayleigh resolution criteria (Culick 1987). The Rayleigh resolution $\Delta t_{Rayleigh}$ of a one dimensional signal is defined as the distance between the maximum point of a pulse and the first diffraction minimum of that pulse. Figure 4-3 depicts the situations when the two identical GPR pulses are resolved at the exact distance of Rayleigh resolution and unresolved, respectively. For pulses with a particular shape, their Rayleigh resolution $B\Delta t_{Rayleigh}$ is inversely proportional to the bandwidth of the pulse, B, or $B\Delta t_{Rayleigh} = const$. Rayleigh resolution is one of the many factors that determine the ability to resolve closely spaced pulses—other factors include the shape of the pulse, the amplitude ratio of the adjacent pulses, and the signal to noise ratio (SNR) of the signal, etc. For GPR antennas with a 2GHz center frequency, if the pavement has a dielectric constant of 9, the EM wave predominant wavelength is 5 cm. While the Rayleigh resolution is about half of the predominant wavelength, 2.5cm, the practical resolution is about one quarter of the predominant wavelength, 1.25cm (Kallweit and Wood 1982). For thin asphalt overlay thickness estimation this is less certain, since the reflection from the bottom of the asphalt overlay is generally small, as shown in Figure 4-1, due to the similarity of the dielectric constants of the asphalt overlay and the old pavement. This suggests that it is much more difficult to resolve thin layers, as in the case of asphalt pavement. It should be noted that the unit of the vertical amplitude axis is normalized voltage. The absolute amplitude value is not critical since in this study we always use the amplitude ratio for calculating the dielectric constant. This is true throughout the dissertation.

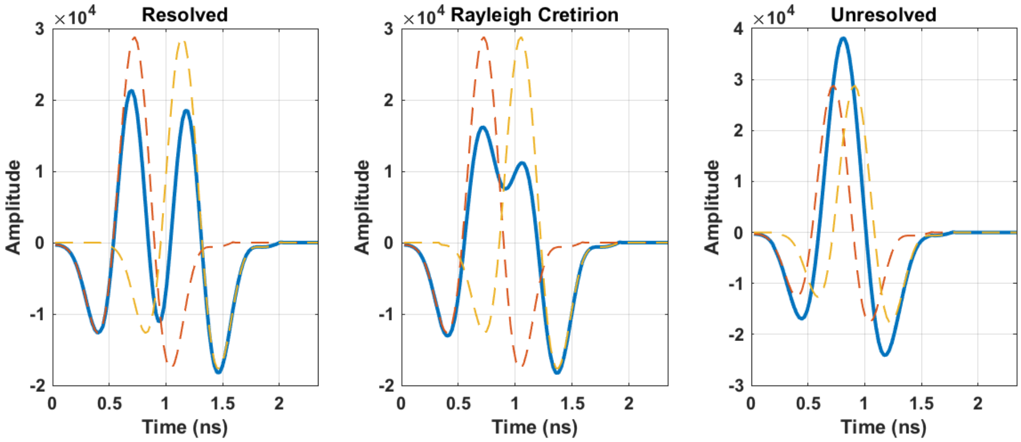

Figure 4-3 Demonstration of Rayleigh resolution of typical GPR signal: red signal is surface reflection, yellow signal is bottom reflection, and blue signal is total reflection.

4.2.3 Tikhonov regularization

Due to physical restrictions, the bandwidth of GPR antennas have an upper limit; thus, signal processing techniques are needed to increase the range resolution. These are called super-resolution techniques. One of the most common is the “layer stripping” method (Spagnonili, 1997), in which reflections are detected by a matched filter detector and then iteratively subtracted from the original signal. This method has been successfully applied to asphalt layer thickness detection (Lahour and Al-Qadi, 2008). The main drawback of this approach is that it is not robust to noises, resulting in large errors in amplitude and dielectric constant detection. An alternative to the layer stripping approach is the linear inversion technique, which we will discuss in this chapter.

Our goal is now to recover the $h(t)$ from equation (4-1). Since real world electronic signals are all continuous in time, the first step is to discretize equation (4-1) such that it can be processed by computer. When the Nyquist criterion is met, we can uniformly sample x(t), y(t) and h(t) to transform Equation (4-1) into:

$$\vec{y} = \boldsymbol{X}\vec{h}, \tag{4-2}$$

where $\vec{y} \in \mathbb{C}^{(m+n-1)\times 1}$ and $\vec{h} \in \mathbb{C}^{n\times 1}$ are vectors of y(t) and h(t), $\boldsymbol{X} \in \mathbb{C}^{(m+n-1)\times n}$ is the Toeplitz matrix constructed from $\vec{x}$, the vector by sampling x(t). Here m and n are the dimensions of $\vec{x}$ and $\vec{h}$, respectively. It should be noted that, technically, $\vec{x}$, $\vec{y}$, and $\vec{h}$ should have infinite lengths due to x(t), y(t) and h(t), but here we ignore the starting and ending zeroes, making the three vectors finite in length. Our problem now is to find the impulse response $\vec{h}$ from $\vec{y}$ and $\boldsymbol{X}$. This is a linear inversion problem: finding $\hat{\vec{h}}$ that can approximate $\vec{h}$.

Following the general GPR image reconstruction theory introduced in Chapter 3.3, there are two types of inversing techniques for the reconstruction of one-dimensional targets (here, asphalt pavement layers): matched filtering and deconvolution. These correspond to migration and inverse filtering techniques employed in general GPR image reconstruction (Soumekh 1999).

The matched-filtering technique is commonly used for chirp signals; i.e., linearly frequency-modulated (FM) signals. However, matched-filtered signals may not resolve pulsed signals (Soumekh 1999). The deconvolution method is a signal processing technique that can in theory perfectly resolve the target location (Riad 1986). For linear FM signals, it can be demonstrated that the matched-filter gives the same result as the deconvolution method. The forward and inverse models of one-dimensional GPR imaging for matched-filter and deconvolution are illustrated in Figure 4-4.

As shown in Figure 4-4, we consider h(t) to be the input signal instead of x(t). This is feasible since convolution is commutable: h(t) is first convolved with x(t) to get output y(t). For the matched-filtering method, $y(t)$ is filtered by $x^*(-t)$, where $x^*(t)$ is the complex conjugate of $x(t)$. Matched filtering is essentially the auto-correlation of signal $x(t)$. For the deconvolution method, $y(t)$ is filtered by $F^{-1}\left(\frac{1}{X(\omega)}\right)$, where F^{-1} represents the inverse Fourier transform, and $X(\omega)$ is the Fourier transform of $x(t)$. We should note that calculating the inverse filter by inverse

Fourier transform of 1/X(ω), as shown in Figure 4-4, is usually not applicable in practice because X(ω) is typically band-limited. Alternatively, the time domain deconvolution can be done by regularization, as illustrated in the following section.

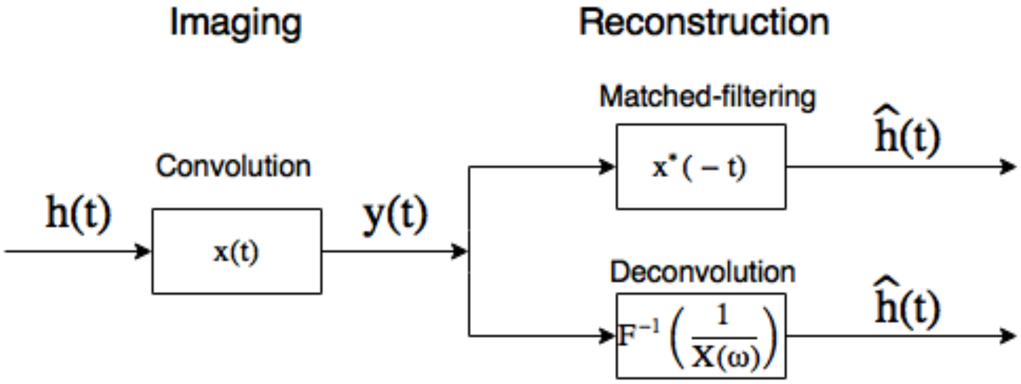

Figure 4-4 1-D target reconstruction: matched filtering and deconvolution.

The matched-filter technique has been used in GPR applications (Leuschen and Plumb 2001). To increase the range resolution of GPR signals, Savelyev and Sato (2004) report the success of the deconvolution method in landmine detection. Al-Qadi and Lahouar (2005) also report good results in estimating asphalt pavement layer thickness using the deconvolution method. Economou et al. (2012) and Schmelzbach et al. (2015) developed several deconvolution algorithms on GPR signals. However, none of these studies concern the ill-posed nature of the deconvolution.

The authors (Zhao et al. 2015) proposed a regularized deconvolution method and applied it on field data, with promising results. Regularizing the deconvolution makes it more robust to noise and small amplitude reflections, such as reflection at asphalt pavement layer interfaces. However, Zhao et al. (2015) only consider zeroth-order Tikhonov regularization, and the influence of noise levels and layer thickness on the performance of the deconvolution algorithm was not discussed.

The inverse problem of Equation (4-2) can be expressed as a simple optimization problem to minimize the least square target function $\left\|\boldsymbol{X}\vec{h}-\vec{y}\right\|^{2}$:

$$\hat{\vec{h}} = \underset{\vec{h}}{\operatorname{argmin}}\left\{\left\|\boldsymbol{X}\vec{h}-\vec{y}\right\|^{2}\right\}, \tag{4-3}$$

where $\left\|\boldsymbol{X}\vec{h}-\vec{y}\right\|^{2}$ represents the L-2 norm of $\boldsymbol{X}\vec{h}-\vec{y}$, "argmin" means to find the argument $\vec{h}$ which minimizes the inner target function. The solution to the above optimization problem can be found by setting the derivative to zero:

$$\nabla_{\vec{h}}\left\|\boldsymbol{X}\vec{h}-\vec{y}\right\|^{2} = 0. \tag{4-4}$$

Solving equation (4-4), we can get the solution of $\hat{\vec{h}}$:

$$\vec{h}_{LS} = (\boldsymbol{X}^{T}\boldsymbol{X})^{-1}\boldsymbol{X}^{T}\vec{y}. \tag{4-5}$$

where $(\boldsymbol{X}^{T}\boldsymbol{X})^{-1}\boldsymbol{X}^{T}$ is called the pseudo-inverse of the matrix $\boldsymbol{X}$ (Groetsch 1977).

Equation (4-4) makes sure that the noise contained in $\vec{y}$, the pavement reflection, is minimized. If we consider the fact that the incident signal $x(t)$ also contains noise, which is usually the case since we are using the copper reflection as the incident signal, the problem becomes the total least squares (TLS) problem:

$$\vec{h}_{TLS} = \underset{\widetilde{\boldsymbol{X}},\tilde{\vec{y}},\vec{h}}{\operatorname{argmin}}\left\{\left\|(\boldsymbol{X},\vec{y})-\left(\widetilde{\boldsymbol{X}},\tilde{\vec{y}}\right)\right\|^{2}\right\}, \text{subject to } \tilde{\vec{y}} = \widetilde{\boldsymbol{X}}\vec{h}. \tag{4-6}$$

According to Golub et al. (1999), this method gives the solution which is a special case of the Tikhonov regularization, which will be discussed later. The difference is that TLS uses negative regularization parameters and therefore de-regularizes the solution (Lampe and Voss 2010).

For solution 4-5, when one or more of the singular values of matrix A is small, the solution $\vec{h}_{LS}$ can be very unstable, meaning that small perturbation in $\vec{y}$ will cause large fluctuations in $\vec{h}_{LS}$. This is called an ill-posed problem. One solution is to use truncated singular-value decomposition

(TSVD; Xu 1988); however, this method decreases the resolution of the solution, biasing it (Aster et. al 2013).

An alternative approach is the regularization method. Tikhonov regularization is one of the major regularization approaches (Groetsch 1984) for the inversion of linear systems. In general, many linear systems can be represented by the Fredholm integral equations of the first kind:

$$g(t) = \int_a^b A(t,s)k(s)ds, \tag{4-7}$$

where k(s) is the input, g(t) is the output, and A(t,s) is the Fredholm integral operator. The Fredholm integral equations of the first kind represent systems including, among others, signal processing (Antoniou 2006), computed tomography (Blahut 2004), and astronomy (Craig and Brown). Equation (4-7) is a general form of the LTI system shown in equation (4-1). Discretizing Equation (4-7) will result in the same form as equation (4-2), except that matrix $\boldsymbol{X}$ in equation (4-2) is a Toeplitz matrix.

The Tikhonov regularization of form (4-2) can be again expressed as an optimization problem:

$$\vec{h}_{Tik} = \underset{\vec{h}}{\operatorname{argmin}} \left\{ \left\| \boldsymbol{X}\vec{h} - \vec{y} \right\|^2 + \alpha \left\| \boldsymbol{L}\vec{h} \right\|^2 \right\}, \tag{4-8}$$

where $\alpha \in R^+$ is the regularization parameter, $\boldsymbol{L}$ is a matrix of full rank, the other symbols are the same as in equation (4-3). The rationale behind using the Tikhonov regularization is to achieve two conditions: first, a small residue for accurate solution and second, a small solution so that the solution is not significantly affected by perturbation. The matrix L can be chosen as an identity matrix, a first-derivative matrix, a second-derivative matrix, etc.; the corresponding regularizations are called the zeroth-, first-, and second-order Tikhonov regularization, respectively.

The general solution of equation 4-8 can be obtained by using generalized singular value decomposition (GSVD). Assume $X \in R^{m\times n}$, $L \in R^{p\times n}$, and $m \geq n \geq p$, by taking derivatives of equation (4-8) with respect to each element in vector $\vec{h}$, and letting the derivatives to be zero, the solutions of equation (4-8) is given by:

$$\vec{h}_{Tik}^{\;(\alpha)} = \sum_{i=1}^{p} \frac{\gamma_i^2}{\gamma_i^2+\alpha} \frac{\vec{u}_i^T \vec{y}}{\sigma_i} \vec{z}_i + \sum_{i=p+1}^{n} (\vec{u}_i^T \vec{y}) \vec{z}_i, \tag{4-9}$$

where γ_i, u_i, and p are defined in the GSVD of matrix pair (X, L) as follows:

$$X = U\Sigma Z^{-1}, L = VMZ^{-1}, \tag{4-10}$$

where $U \in R^{m\times n}$, $V \in R^{p\times p}$ have orthonormal columns such that $U^T U = I_n$ and $V^T V = I_p$; $Z \in R^{n\times n}$ is nonsingular matrix, and Σ and M are of the form:

$$\Sigma = \begin{bmatrix} \Sigma_p & o \\ 0 & \mathrm{I}_{n-p} \end{bmatrix}, M = [\mathrm{M}_p \quad 0]. \tag{4-11}$$

The matrices $\Sigma_p = diag(\sigma_i)$ and $\mathrm{M}_p = diag(\mu_i)$ are both $p \times p$ diagonal matrices whose diagonal elements satisfy $\sigma_i^2 + \mu_i^2 = 1$ and in the following order:

$$0 \leq \sigma_1 \leq \cdots \leq \sigma_p \leq 1, 1 \geq \mu_1 \geq \cdots \geq \mu_p \geq 0. \tag{4-12}$$

The generalized singular values γ_i of (X, L) are defined as

$$\gamma_i \equiv \frac{\sigma_i}{\mu_i}, i = 1, \cdots, p. \tag{4-13}$$

It can be shown that the singular values φ_i of X can be expressed as $\varphi_i = \gamma_{n-i+1}, i = 1, \cdots, n$ when L is identity matrix.

A more detailed derivation can be found in Aster et al. (2013, 4.2).

When the matrix L is identity matrix, solution (4-9) can be simply reduced to:

$$\vec{h}_{Tik}^{\;(\alpha)} = (\boldsymbol{X}^T\boldsymbol{X} + \alpha I)^{-1}\boldsymbol{X}^T\vec{y}. \tag{4-14}$$

4.2.4 Total variation (TV) regularization

In the Tikhonov regularization discussed in the previous section, discontinuities in the original solution are smoothed out because smooth changes are penalized less by the quadratic regularization term $\left\|\boldsymbol{L}\vec{h}\right\|^2$ than abrupt changes. Therefore, the Tikhonov regularization will not perform well in situations when sharp changes exist in the solution. Alternatively, the total variation (TV) can be used as the cost function:

$$TV(\vec{h}) = \sum_{i=1}^{n-1} |h_{i+1} - h_i| = \left\|\boldsymbol{L_1}\vec{h}\right\|_1, \tag{4-15}$$

where $\|\cdot\|_1$denotes the L1-norm, and L is the first-derivative matrix:

$$L_1 = \begin{bmatrix} -1 & 1 & & & \\ & -1 & 1 & & \\ & & \ddots & \ddots & \\ & & & -1 & 1 \\ & & & & -1 \end{bmatrix}. \tag{4-16}$$

Replacing the cost function in Tikhonov regularization (4-8) with $TV(\vec{h})$, we can get the expression of TV regularization:

$$\vec{h}_{TV} = \underset{\vec{h}}{\operatorname{argmin}} \left\{ \left\|\boldsymbol{X}\vec{h} - \vec{y}\right\|^2 + \alpha \left\|\boldsymbol{L_1}\vec{h}\right\|_1 \right\}. \tag{4-17}$$

The L1-norm cost function is not differentiable at the origin; instead, we can take the derivative at other points and set them to be zero at the origin. The following equation can be obtained:

$$(2X^T X + \alpha L_1^T W L_1)\vec{h} = 2X^T \vec{h}, \tag{4-18}$$

where W is a diagonal matrix with elements:

$$W_{i,i} = \frac{1}{|h_{i+1} - h_i|}, \tag{4-19}$$

where $(h_{i+1} - h_i)$ is the i^th^ element of vector $\boldsymbol{L_1}\vec{h}$. To accommodate the nondifferentiability of the L1-norm, we can set a tolerance ε, and let:

$$W_{i,i} = \begin{cases} 1/|h_{i+1} - h_i|, |h_{i+1} - h_i| > \varepsilon \\ 1/\varepsilon, |h_{i+1} - h_i| \le \varepsilon \end{cases}. \tag{4-20}$$

Equation (4-18) cannot be solved directly via generalized singular-value decomposition, because matrix W is dependent on $\vec{h}$. The way to solve equation (4-18) is to do it iteratively, using the iteratively reweighted least squares (IRLS; Aster et al. 2013). It begins with the least squares solution ${\vec{h}_{TV}}^{(0)} = \vec{h}_{Tik}$ from equation (4-5). Then calculate $L_1{\vec{h}_{TV}}^{(0)}$ and update matrix W using equation (4-18). Then solve equation (4-18) to obtain a new solution ${\vec{h}_{TV}}^{(1)}$ and associated $L_1{\vec{h}_{TV}}^{(1)}$. The iteration stops if

$$\frac{\left\|{\vec{h}_{TV}}^{(k+1)} - {\vec{h}_{TV}}^{(k)}\right\|}{1+\left\|{\vec{h}_{TV}}^{(k+1)}\right\|} < \tau. \tag{4-21}$$

for some tolerance τ.

It can be illustrated that this process always converges to an approximation of solution equation 4-17 (Aster et al. 2013).

4.2.5 L-curve criterion

From equation (4-8) it can be demonstrated that the norm of solution $\left\|L{\vec{h}_{Tik}}^{(\alpha)}\right\|^2$ and the norm of residue $\left\|X{\vec{h}_{Tik}}^{(\alpha)} - \vec{y}\right\|^2$ can be expressed as:

$$\left\|L{\vec{h}_{Tik}}^{(\alpha)}\right\|^2 = \sum_{i=1}^{p}\left(\frac{\gamma_i^2}{\gamma_i^2+\alpha}\frac{\vec{u}_i^T\vec{y}}{\sigma_i}\right)^2, \tag{4-22}$$

$$\left\|X{\vec{h}_{Tik}}^{(\alpha)} - \vec{y}\right\|^2 = \sum_{i=1}^{p}\left(\frac{\alpha}{\gamma_i^2+\alpha}\vec{u}_i^T\vec{y}\right)^2 + \delta_0, \tag{4-23}$$

where $\delta_0 \equiv \|(I_m - UU^T)\vec{y}\|$ is the residue norm at infinite regularization. All the variables are the same as the ones in equation (4-9).

Then it can be shown that under the discrete Picard condition (Hansen 1990), the plot of L-curve $(\left\|X\vec{h}^{(\alpha)} - \vec{y}\right\|^2, \left\|L\vec{h}^{(\alpha)}\right\|^2)$ will have a distinct “corner.” It is demonstrated that choosing the regularization parameter at the "corner" of the L-shaped usually yields better results than by employing other regularization parameter choosing criteria (Hansen 1992).

There are several methods to determine the regularization parameter α in equations (4-8) and (4-16). The discrepancy principle (Morozov 2012) selects α so that the residue norm is equal to the norm of the error in y. It is shown that the discrepancy principle yields α to the right of the corner of the L-curve, and therefore over-smooths the solution. The quasi-optimality criterion (Morozov 2012) seeks to balance the regularization error and the perturbation error, and corresponds to locating the “corner” of the L-curve. The generalized cross-validation (GCV) method (Golub et. al 1979) is based on a statistical consideration; i.e., to choose α that predicts the missing data. However, it is difficult to find the minimum of the GCV because of its flatness; hence the performance of the GCV method is not good for highly correlated noise.

Choosing the regularization parameter at the “corner” of the L-shaped curve (L-curve criterion) typically yields better results than by using other regularization parameter-choosing criteria (Hansen 1990). Therefore, in this study, the L-curve criterion was used to select the appropriate regularization parameter in both Tikhonov regularization and total variation regularization.

4.3 Simulation

4.3.1 GPR signal simulation

In this section, we will use the simulated GPR signals to model the two-layered pavement model shown in Figure 2-4, where the surface binder has dielectric constant of ε_1 and the leveling binder has dielectric constant of ε_2. The peaks of the two pulses are shifted into alignment with the layer interface position to show the relationship between the impulse responses (two red arrows). The simulated GPR signals are generated by convoluting real GPR incident signals with the two impulses with different distances. We are only considering two layers because the pavement layer below the asphalt overlay is usually thick compared to the wavelength, and hence multiple pulse overlapping is rare. The reflection model is a linear time-invariant system and can be represented by LTI system equation (4-1), which is a special case of general linear system equation (4-7). The GPR used in the study is a pulsed 2GHz antenna manufactured by GSSI, Inc., and is shown in Figure 4-5. Both orange boxes are identical 2GHz antennas, with serial numbers of 0031 and 0080, respectively. The sampling interval of this GPR system is 0.0234ns (sampling frequency of 42.7GHz). The incident signal is a Ricker wavelet collected over a copper plate, which can be considered a perfect reflector.

Figure 4-5 Two 2GHz antennas mounted on vehicle (Zhao and Al-Qadi 2017b).

For an antenna with a specific frequency—e.g., 2GHz in this study—its EM wavelength remains constant in terms of time, whatever medium it is traveling in. Since GPR signals are not single frequency signals, their wavelength refers to the predominant wavelength. For this reason, in this simulation study, we use time instead of length to characterize layer thickness. In particular, we vary the distance between the assumed impulses between 0.351ns to 1.170ns in 36 equal steps. If the dielectric constant of the asphalt overlay is 6, the corresponding overlay thickness is from 2.15cm to 7.16cm, which covers the typical asphalt overlay thickness range.

Here, we can assume that the magnetic permeability of the surface binder and the leveling binder are the same as free space. If the dielectric constants of the surface binder and the the leveling binder are assumed to be 9 and 4.6, respectively, then according to the Snell's law referenced in section 2.2.1, the amplitude of the two impulses A_1/A_p and A_2/A_p are approximately -0.5 and 0.17, as shown in the top right corner of Figure 4-6.

To verify that the regularization methods are robust to noise, we add artificial Gaussian white noise to the simulated GPR signals at six SNR levels: 5dB, 10dB, 15dB, 20dB, 25dB, and 30dB. An illustration of the simulation model is shown in Figure 4-6. The top-left figure is the 2GHz GPR incident signal. This is obtained by inversing the sign of the copper reflection data. The top-right picture is the assumed system impulse response according to layer thickness and dielectric constant. The bottom-left figure is the simulated pavement reflection signal. The bottom-right figure is the noisy signal.

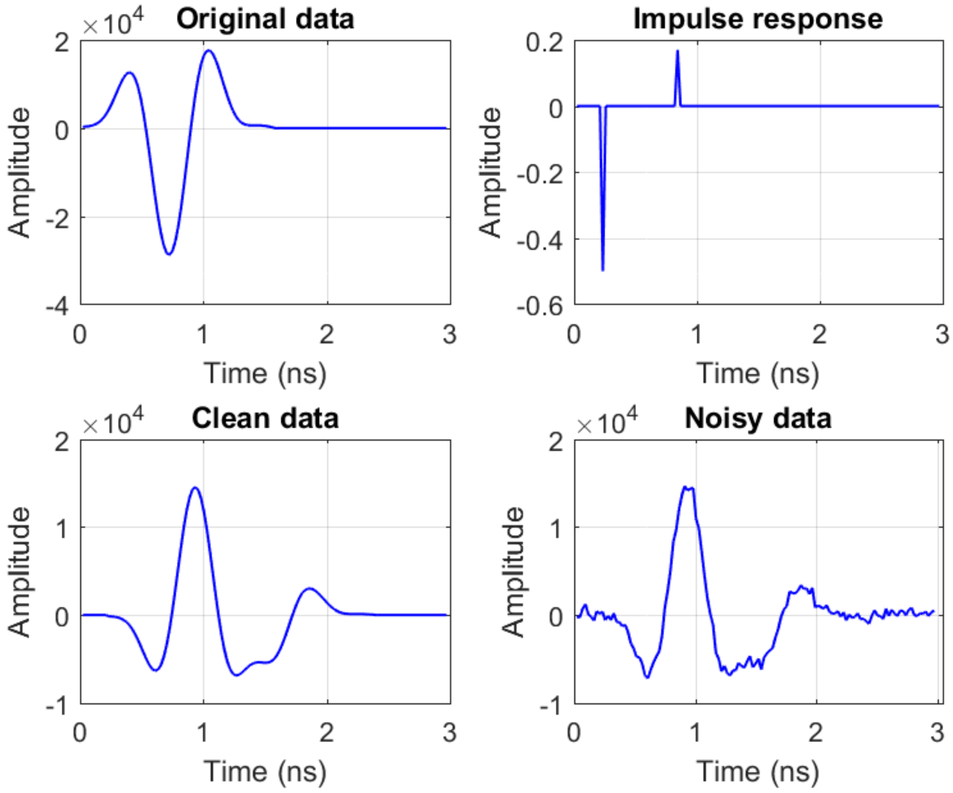

Figure 4-6 One simulation example. Top-left: incident signal, top-right: impulse response with distance of 0.61ns, bottom-left: simulated signal, and bottom-right: noisy signal.

Four regularization methods (i.e., zeroth-, first-, and second-order Tikhonov, and TV) are applied to the noisy signal to increase the range resolution. The regularization parameters are selected based on the L-curve criterion:

- The L-curve was generated by calculating $\vec{h}^{(\alpha)}$ using different α values and plotting the norm of solution $\left\|L\vec{h}^{(\alpha)}\right\|^2$ and the norm of residue $\left\|X\vec{h}^{(\alpha)} - \vec{y}\right\|^2$.
- The L-curve was then interpolated using cubic spline interpolation.
- The curvature of the interpolated L-curve was then calculated using

$$\kappa = \frac{C''}{(1+C'^2)^{3/2}}, \tag{4-24}$$

where C' and C'' are the first derivative and second derivative of the L-curve with respect to the horizontal axis variable, and the regularization parameter corresponding to the maximum curvature is selected and considered to be at the corner of the L-curve (Hansen and O'Leary 1993).

4.3.2 Results

For zeroth-, first-, and second-order Tikhonov regularization, each case (noise level and layer thickness) was repeated 30 times to ensure statistical correctness. For TV regularization, only 8 repetitions were performed because of the longer computation time. In applications such as the asphalt layer thickness estimation, the accurate determination of the impulse distance is the most important parameter; while in applications of the asphalt pavement density estimation, the accurate amplitude from the recovered pulses are the desired information. In this study, the error in estimated impulse distance for each case was calculated and compared to the true layer thickness. We'll also look at the recovered amplitudes to see if they represent the true impulse response amplitudes. Table 4-1 shows all the simulation test configurations:

Table 4-1 Configurations of simulation cases

Regularization method	SNR (dB)	Impulse distance (ns)	# or Repetitions	Surface binder dielectric constant	Leveling binder dielectric constant
Zeroth-order Tikhonov	5 to 30 at step of 5	0.351ns to 1.170ns in 36 equal steps	30	9	4.6
First-order Tikhonov					
Second-order Tikhonov					
TV			8		

Because of the large number of data points (over 20,000 cases) and figures generated, only a few typical examples are shown to illustrate the observations.

Figure 4-6 shows one simulation example with noise added: the first plot is the incident signal; the second, the assumed impulse response with distance of 0.61ns; the third, the simulated clean signal; the fourth, the noisy data with SNR of 20dB. It can be seen that it is impossible to resolve the two pulses in either clean or noisy signals without regularization. Since the sign of the impulses are not important, and the concern is to increase the resolution of the GPR signal, in later plots the sign of the impulse response and regularization result are inverted for better visualization.

Doing the deconvolution without regularization as shown in equation (4-5) produces the result shown in Figure 4-7(a). The large fluctuation of the solution is due to the ill-posed nature of the Toeplitz matrix X. Figure 4-7(b) shows the matched-filtered signal. The once overlapped two pulses still cannot be resolved, which indicates that the matched-filtering technique doesn't have good performance for the pulse signals.

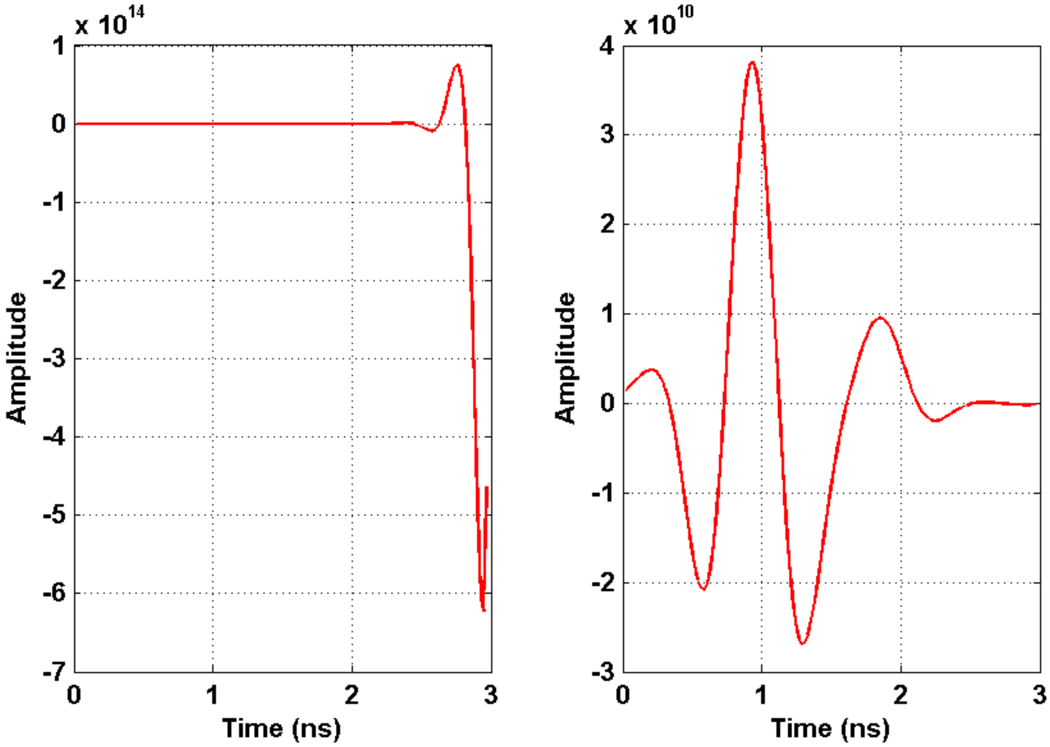

(a) (b)

Figure 4-7 (a) Pseudo-inverse solution $\vec{h}_{LS}$ and (b) matched-filter reconstruction solution.

The solutions of the example model shown in Figure 4-6 using zeroth-, first-, and second-order Tikhonov and TV regularization are shown in Figures 4-8 to 4-11, respectively. In each of the figures, the first plot is the L-curve, where the solid line is the original L-curve, and the dotted line is the spline-interpolated L-curve; the second plot is the curvature of the interpolated L-curve; the third plot is the regularized solution.

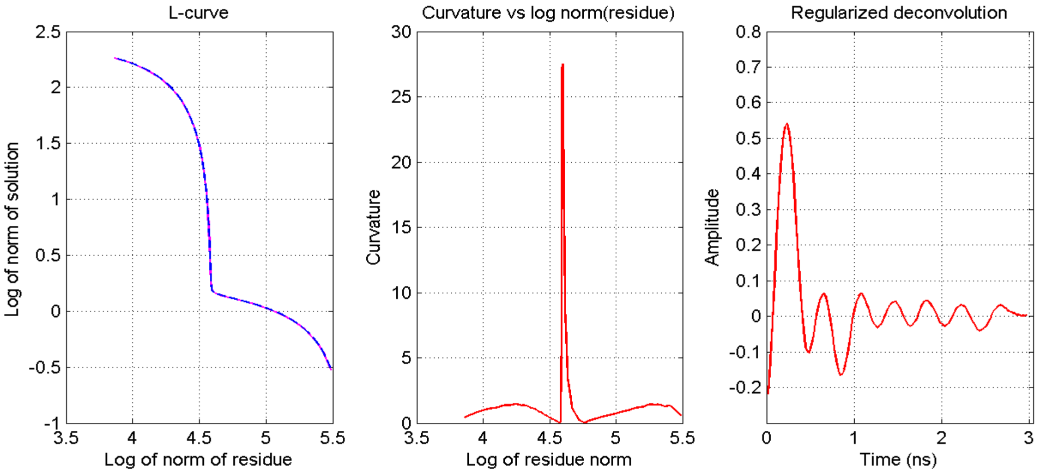

(a) (b) (c)

Figure 4-8 Zeroth-order Tikhonov regularization: (a) L-curve, (b) plot of L-curve curvature, and (c) regularized solution.

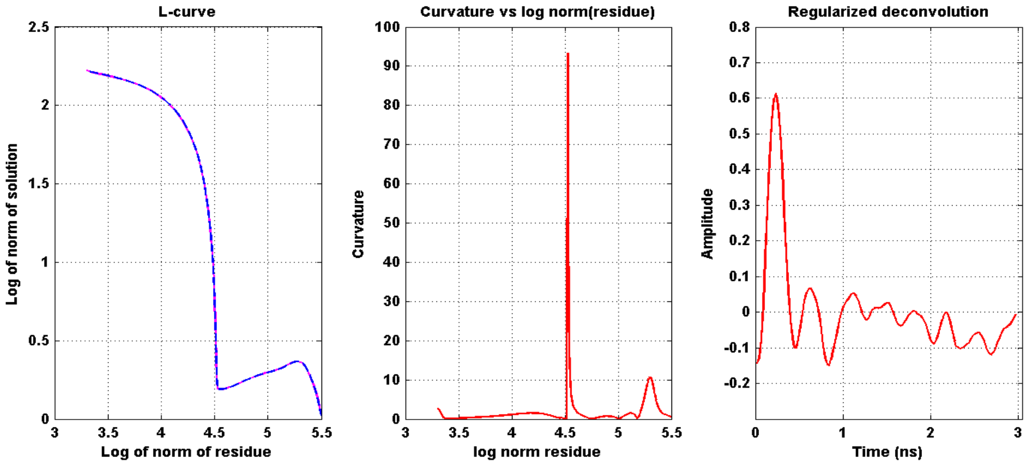

(a) (b) (c)

Figure 4-9 First-order Tikhonov regularization: (a) L-curve, (b) plot of L-curve curvature, and (c) regularized solution.

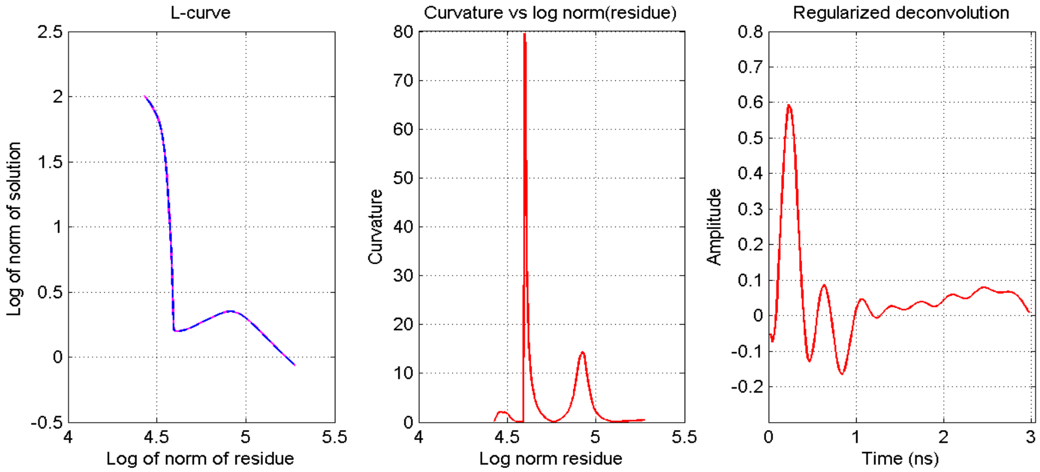

(a) (b) (c)

Figure 4-10 Second-order Tikhonov regularization: (a) L-curve, (b) plot of L-curve curvature, and (c) regularized solution.

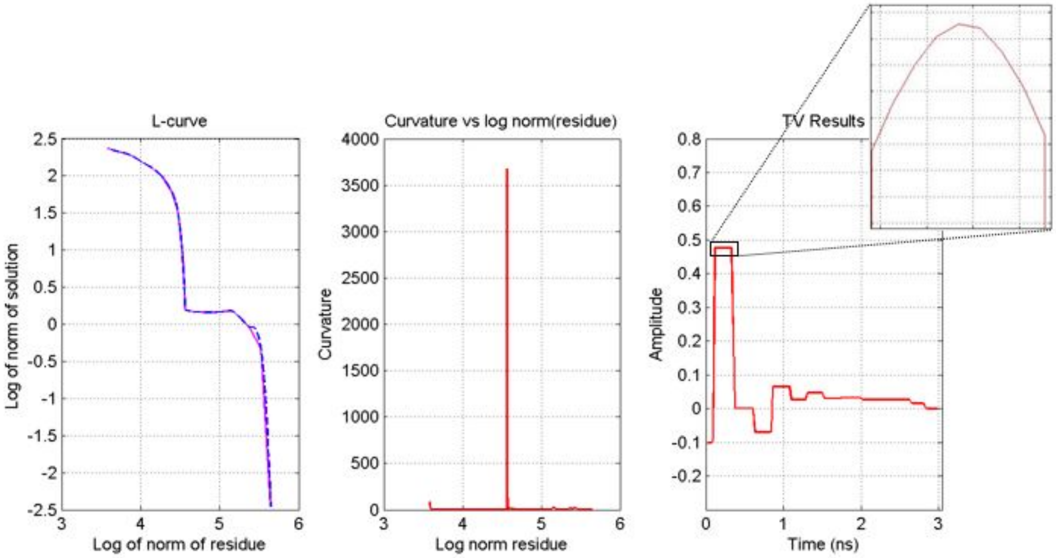

(a) (b) (c)

Figure 4-11 TV regularization: (a) L-curve, (b) plot of L-curve curvature, and (c) regularized solution.

Figures 4-8 to 4-11 show that all four regularizations have some kind of “L-curve,” although the “L-curve” was originally demonstrated only for Tikhonov regularization. The shapes of the L-curves from four regularization methods are slightly different, but the maximum curvature always occurs at the “corner” of the L-curve.

The regularization solutions from four regularizations display different properties. Plotting all four regularization solutions together with the assumed impulse response of the better reveals their differences, as shown in Figure 4-12.

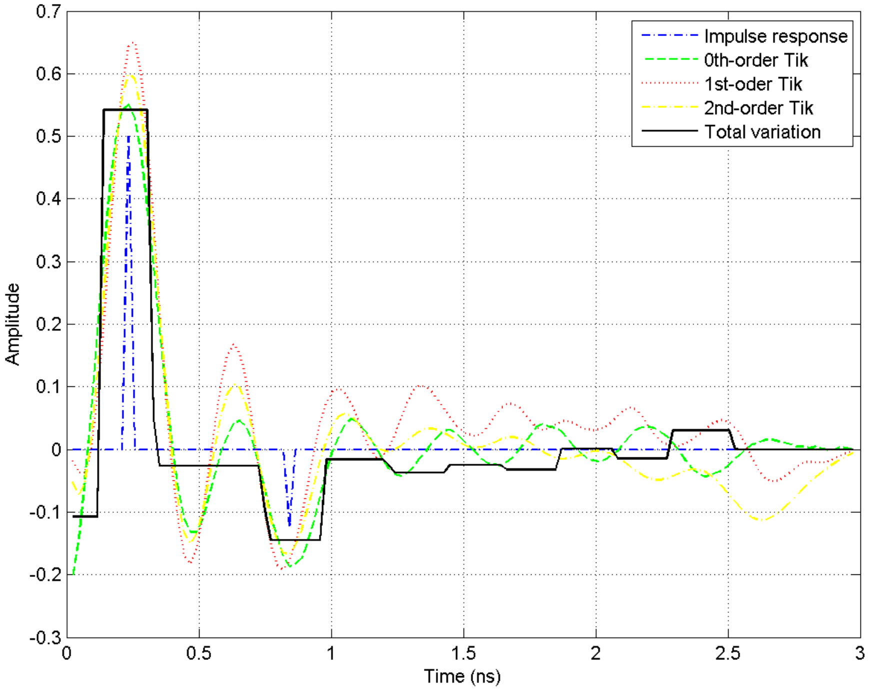

Figure 4-12 Plot of four regularization solutions and the impulse response.

In Figure 4-12, the peaks of signals are scaled to represent the two true impulse response amplitude. We can see that the recovered amplitude is not accurately representing the true impulse response amplitude. This means that the regularization method doesn't work for thin overlay density estimation. Table 4-2 shows the comparison of the amplitudes between the regularization results and the true impulse response. The amplitude data are obtained only from one random example where the impulse distance is 0.6084 ns and the noise level is SNR=20. This is to show that the amplitude errors are too large to be used for dielectric constant estimation and asphalt pavement density prediction.

Table 4-2 Comparison between recovered peak amplitudes and true impulse amplitudes

Regularization method	Surface reflection coefficient	Error between true impulse response (-0.5)	Bottom of surface reflection coefficient	Error between true impulse response (-0.17)
Zeroth-order Tikhonov	-0.5418	8.36%	0.1505	-11.47%
First-order Tikhonov	-0.5504	10.08%	0.1518	-10.71%
Second-order Tikhonov	-0.5745	14.90%	0.1443	-15.12%
TV	-0.5568	11.36%	0.1428	-16.00%

Figure 4-12 also shows that the three Tikhonov regularization methods give similar solutions with smooth changes, while the solution from the TV regularization has sharp changes. This result agrees with the theory that TV cost penalizes for sharp changes less than L^2-norm costs. Among three Tikhonov regularizations, the first- and second-order Tikhonov regularizations give smoother solutions than the zeroth-order Tikhonov regularization, but the solutions are skewed from the horizontal axis. This is because the cost function of the first-order Tikhonov regularization is the first-derivative matrix, and it penalizes the changes of the solution; the cost function of the second-order Tikhonov regularization is the second-derivative matrix, and it penalizes the rate of changes of the solution. The zeroth-order Tikhonov regularization is closer to the horizontal axis, but it is more fluctuating. This is because the cost function of the zeroth-order Tikhonov regularization is the identity matrix, and it penalizes only the absolute value of the solution.

The impulse response becomes "rectangular" in the TV regularization solutions. However, the zoomed-in version of the TV solution shows that the rectangular function has a maximum (or minimum for negative impulse) value near the center of the rectangular function. Therefore, it is still possible to find the distance between the two rectangular functions by locating the local maximum (or minimum). However, in practice the Tikhonov regularizations are preferred because the local maximum (or minimum) is easier to identify than in the TV regularization method.

The above results are from the case where the distance of the two impulses is 0.61ns, and the SNR is 20dB. All other cases yield similar results except when the distance of the two impulses is smaller than 0.51ns, when all regularization methods fail to resolve the two.

By identifying the local maximum (or minimum), the impulse distance can be found from the regularization solution. Therefore, the accuracy can be calculated by comparing the distance from the regularization solution and the original distance. For the case of 25dB SNR, the plots of the mean and standard deviation of the relative error versus impulse distances are shown in Figures 4-13 to 4-16, for zeroth-, first-, and second-order Tikhonov and TV regularization, respectively.

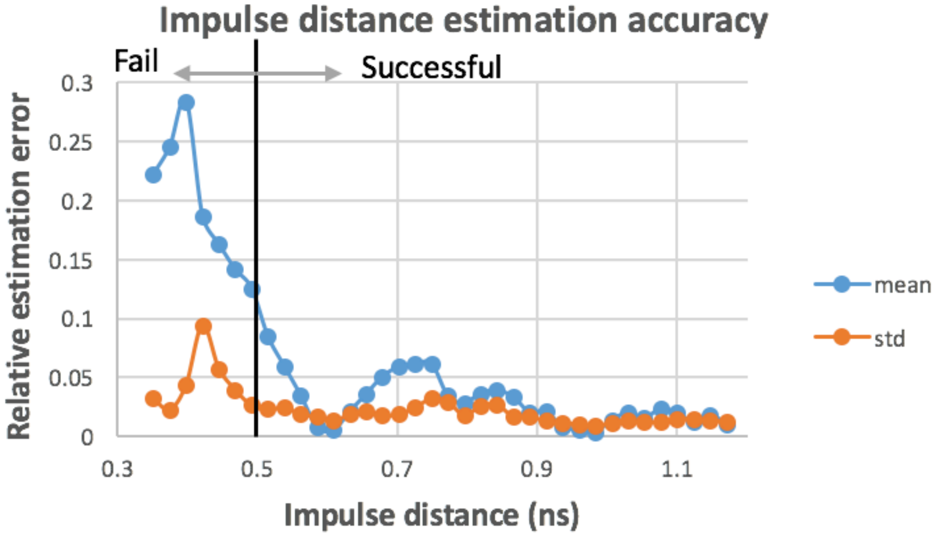

Figure 4-13 Impulse distance estimation accuracy of zeroth-order Tikhonov regularization

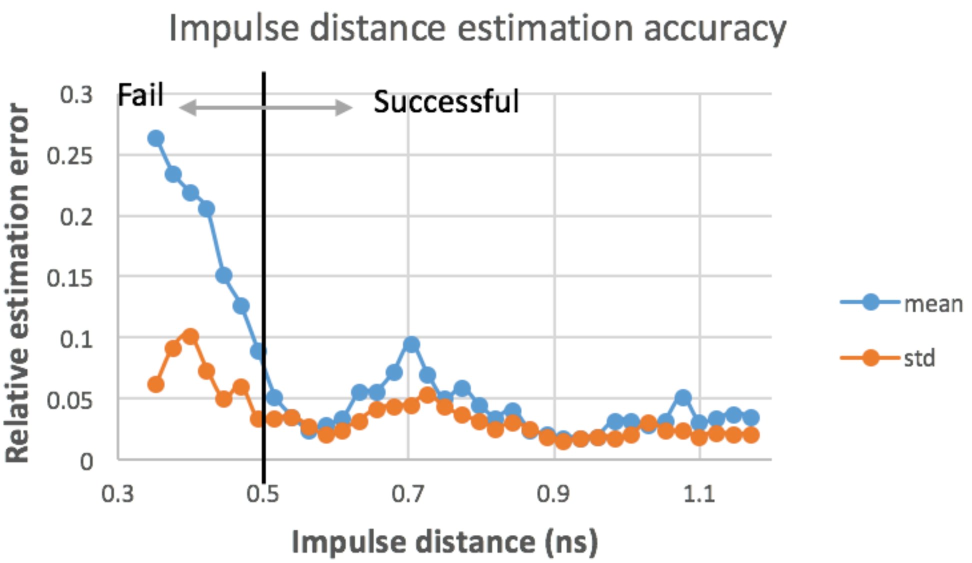

Figure 4-14 Impulse distance estimation accuracy of first-order Tikhonov regularization

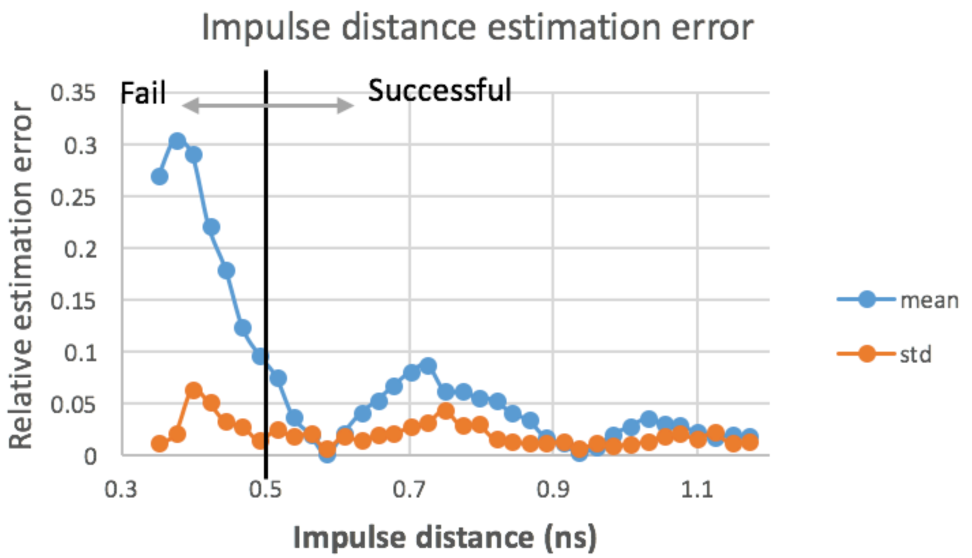

Figure 4-15 Impulse distance estimation accuracy of second-order Tikhonov regularization

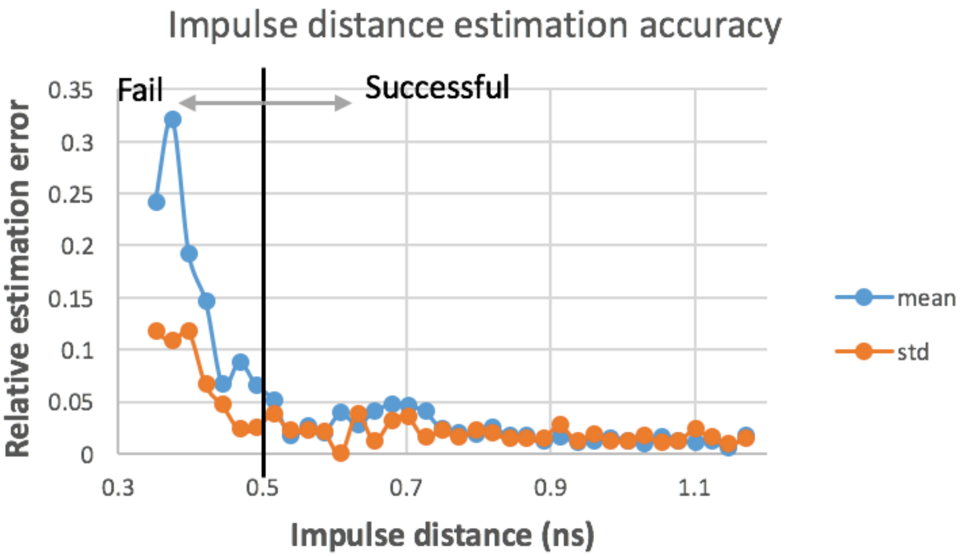

Figure 4-16 Impulse distance estimation accuracy of TV regularization

It should be noted that the results when the impulse distance is smaller than 0.51ns are meaningless because the two pulses overlap with each other after regularization, and the second peak does not necessarily represent the location of the second impulse. As such, the large error means and standard deviations when the impulse distance is smaller than 0.51ns and the decrease of the error means and standard deviations when the impulse distance is close to zero do not provide any useful information.

Figures 4-13 to 4-16 show that the means and standard deviations of the estimation errors from the three Tikhonov regularizations have a sudden increase when the impulse distance is around 0.7ns; the reason is related to the shape of the incident signal. The zeroth-order Tikhonov outperforms the first- and second-order Tikhonovs in terms of the sudden increase of error means and standard deviations. For the TV regularization, there is no such sudden increase and the error means and standard deviations change less with distance. This is again expected because the target function has sharp changes (two impulses).

For all 6 SNR levels, the average estimation error and error standard deviation for impulse distances greater than 0.51ns are shown in Table 4-3 for four regularization methods.

Table 4-3 Average estimation error and average standard deviation of the error for impulse distances larger than 0.51ns

SNR (dB)	Regularization	Zeroth-order Tik	First-order Tik	Second-order Tik	TV	Average
5	Average error (%)	4.76	7.93	7.15	5.82	6.42
	Average std (%)	3.51	6.22	6.96	6.37	5.77
10	Average error (%)	3.47	5.59	5.29	3.62	4.49
	Average std (%)	2.52	5.03	3.77	3.08	3.60
15	Average error (%)	3.03	4.29	4.39	2.94	3.66
	Average std (%)	2.06	3.14	2.93	2.83	2.74
20	Average error (%)	2.89	3.97	4.07	2.41	3.34
	Average std (%)	1.80	3.14	2.60	2.35	2.47
25	Average error (%)	2.71	4.05	3.51	2.09	3.09
	Average std (%)	1.75	2.90	1.85	1.80	2.08
30	Average error (%)	2.83	3.93	3.57	1.97	3.08
	Average std (%)	2.10	2.99	1.52	1.77	2.10
Average	Average error (%)	3.28	4.96	4.66	3.14	4.01
	Average std (%)	2.29	3.90	3.27	3.03	3.12

Table 4-3 shows that first the average error for the TV regularization is 3.14%, and smaller than the three Tikhonov regularization methods. This is expected because the impulse response solution has sharp changes, which are penalized less in the TV cost than L2-norm cost. Second, the zeroth-order Tikhonov regularization has the least average standard deviation, 2.29%. This means the results coming from the zeroth-order Tikhonov regularization are more stable than those obtained using other regularization methods. Third, considering both average error and the average standard deviation, the TV regularization and the zeroth-order Tikhonov regularization outperform the first- and the second-order Tikhonov regularizations. The zeroth-order Tikhonov regularization is preferred in practice to increase the range resolution of the GPR signals, since the peak is easier to identify compared to TV regularization. Finally, the performances of the regularization methods are better at high SNR levels. Using GPR antennas with high gain results in better SNR values.

The computation time of four regularization methods using a computer with Intel i7 processor is shown in Table 4-4. It was found that TV regularization requires significantly longer computation time than Tikhonov regularizations because TV regularization can only be solved iteratively using IRLS algorithm.

Table 4-4 Computation time of three four regularization methods

Regularization	Zeroth-order Tik	First-order Tik	Second-order Tik	TV
Computation time (s)	0.512	0.556	0.664	20.3

4.3.3 Discussion

In this simulation study, GPR signals reflected from a two-layered reflection system are simulated by convoluting GPR incident signals with assumed impulses. We assumed impulse distances ranging from 0.351ns to 1.170ns (the corresponding layer thicknesses ranging from 2.15cm to 7.16cm assuming the dielectric constant of the asphalt is 6) and signal-to-noise ratios ranging from 5dB to 30dB. Four types of regularization methods (i.e., zeroth-, first-, and second-order Tikhonov and total variation regularization) are applied to the noisy GPR signals to increase the signal range resolution. The regularization parameter was selected based on the L-curve criterion. The following points summarize the findings of the simulation study:

- The solutions of both Tikhonov and total variation regularization display the “L-curve” property. The “L-curve” criterion can be applied to both regularization methods to find the appropriate regularization parameter.
- Tikhonov and total variation regularization methods can effectively increase the GPR signal range resolution even when the second pulse from asphalt pavement overlay is small. Accurate impulse distance can be obtained when the impulse distance is larger than 0.51ns.

- Total variation regularization requires significantly longer computation time because it has to be solved iteratively.
- The total variation regularization and zeroth-order Tikhonov regularization outperform the first- and second-order Tikhonov regularizations in terms of the average impulse distance estimation error and the average standard deviation of the error. For total variation regularization and zeroth-order Tikhonov regularization, the absolute layer thickness estimation error, when the layer thickness is not thinner than 25.5mm, is less than 1mm, which is well below the construction tolerance.
- A higher SNR ratio improves the accuracy of layer thickness estimation. GPR antennas with high gains are preferred in practice.

This study shows the feasibility of regularization methods to increase the range resolution of GPR signals, such that thin asphalt pavement layers can be resolved. Since the zeroth-order Tikhonov regularization is preferred in practice, in the next chapter, we’ll study the performance of the zeroth-order Tikhonov regularization on field GPR data.

4.4 Summary

In this chapter, a regularization algorithm was developed to find the TWTT from GPR signals reflected from thin asphalt overlay. Regularization is an optimization approach to invert a linear system in the presence of noise.

Four regularization methods—zeroth-order, first-order, and second-order Tikhonov regularization and TV regularization—were used on simulated GPR signals reflected from thin overlay. It was found that zeroth-order Tikhonov and TV regularization outperforms the first-order and second-order Tikhonov regularization in terms of accuracy of estimating the TWTT. The zeroth-order Tikhonov regularization has less time complexity and is easier to perform. It was also found that when the impulse distances are smaller than 0.51ns, the regularization methods fail to resolve the overlapped signals.

From simulations, it was demonstrated that regularization is an efficient method to increase the range resolution of GPR signals, and to recover the TWTT from overlapped signals; however, regularization can’t restore the surface reflection amplitude, and therefore can’t be used to find the dielectric constant of the thin overlay.

CHAPTER 5: APPLICATION OF REGULARIZED DECONVOLUTION TECHNIQUES FOR PREDICTING PAVEMENT THIN AC OVERLAY THICKNESSES

5.1 Background and Objective

Based on the simulation study in Chapter 4, we can see that the zeroth-order Tikhonov and TV regularization outperform first-order and second-order Tikhonov regularization. The TV regularization results show nearly flat signals around the peak making it difficult to identify the TWTT. For this reason, we will choose the zeroth-order Tikhonov regularization as the algorithm for predicting the thin AC overlay thickness. To validate this algorithm, in this chapter we'll apply the zeroth-order Tikhonov regularization on in-service thin AC overlay sections.

In section 5.2, the field construction site will be described in detail. The results and discussion will be provided in sections 5.3 and 5.4, with a summary following in section 5.5.

5.2 Description of the Construction Site

A field study was conducted on IL-72 in Hoffman Estates and Barrington in Illinois in October of 2010 (Son et. al 2013). Thin asphalt concrete overlays with different layer thicknesses and mixture types were constructed on concrete pavement on two lanes in both directions. Below the wearing surface, a leveling binder layer was first placed to make the total overlay (leveling binder plus wearing surface) thickness equal to 50.8 mm, as shown in Figure 5-1. Only the wearing surface layer thickness was calculated in this study. The material of the leveling binder is a sprinkle mix without chips along with less expensive materials (which usually has a lesser dielectric constant than the wearing surface). Table 5-1 shows a summary of a total of five different mixtures. The layer thicknesses, in terms of EM wavelength, are calculated knowing that the duration of EM wavelength is 0.5382 ns (according to 2GHz GPR incident signal); the dielectric constant of asphalt concrete is assumed to be 6.

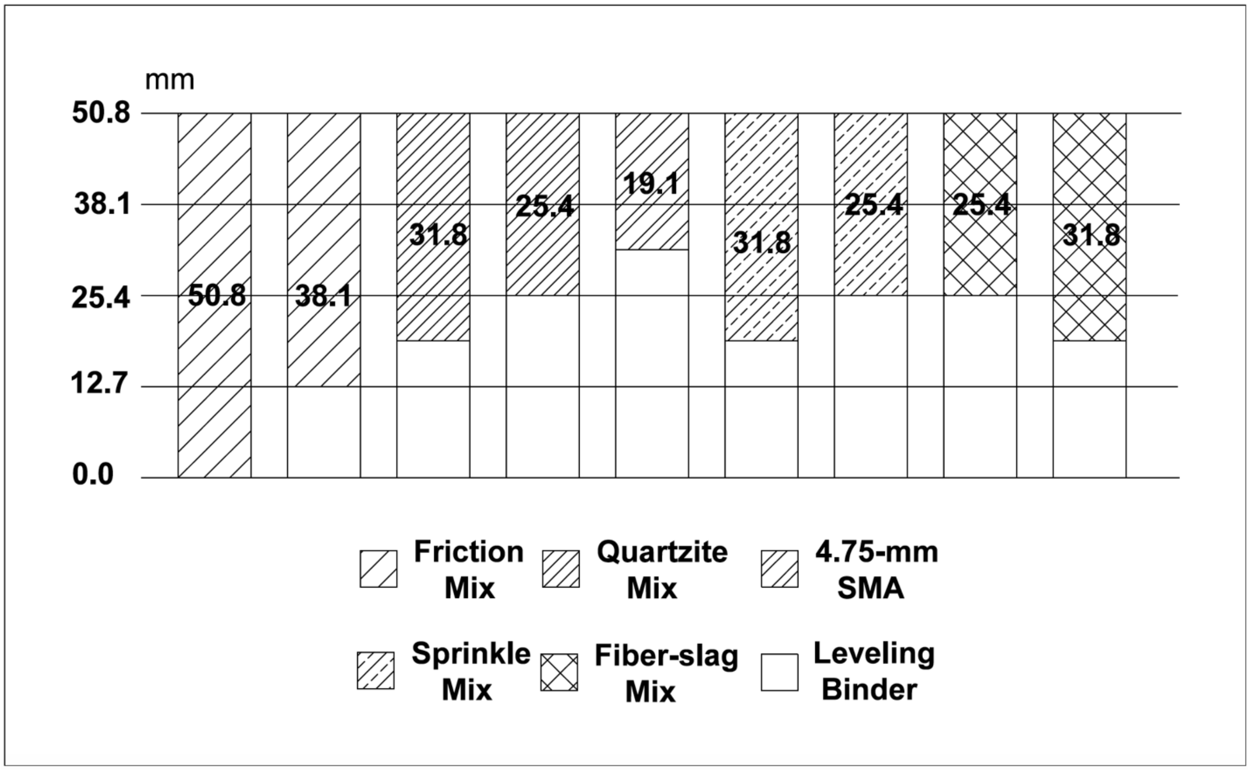

Figure 5-1 Design thickness of leveling binder and wearing surface in each section.

Table 5-1 Summary of Different Mixtures Used in Construction and Their Layer Thicknesses

Mixture	Binder Type	Asphalt Content (%)	Aggregate	Layer Thickness (mm)	Thickness in Terms of EM Wavelength
Friction mix	PG 70-22	5.1	Dolomite and slag	38.1/50.8	1.16/1.54
Quartzite mix	PG 70-22	5.8	Quartzite and dolomite	25.4/31.8	0.77/1.16
4.75-mm SMA	PG 70-22	7.3	Dolomite and quartzite	19.1	0.58
Sprinkle mix	PG 70-22	6.1	Dolomite	25.4/31.8	0.77/1.16
Fiber-slag mix	PG 70-22	5.7	Dolomite and slag	25.4/31.8	0.77/1.16

After construction, GPR survey was conducted at six static locations in each section. As shown in Figure 5-2, a 2.0 GHz (center frequency) air-coupled antenna manufactured by GSSI was used in the study. The designed thicknesses of each section were validated by taking cores from the same locations where the GPR data were collected and the thicknesses are included in the name of each section (e.g., section F-mix-50.8 has the thickness of 50.8 mm).

Figure 5-2 GPR data collection.

5.3 Results

Figure 5-3 shows the result at the left lane of 25.4-mm-quartzite section as an example of GPR signal before and after deconvolution with zeroth-order Tikhonov regularization. Figure 5-3(a) depicts the GPR signal collected over a flat copper plate, which represents the reverse of the incident signal. Figure 5-3(b) features a raw pavement reflection signal truncated from the original signal and shows that the second peak is hidden under the surface reflection. Figure 5-3(c) is the L-curve of the zeroth-order Tikhonov regularization. Figure 5-3(d) is the impulse response deconvoluted using α selected based on the L-curve, as shown in Figure 5-3(c). The second peak is clear, as indicated by the arrow. In addition, it should be noted that the fluctuation after the second peak is caused by the interference of the pavement structure underneath the surface layer and should thus be ignored.

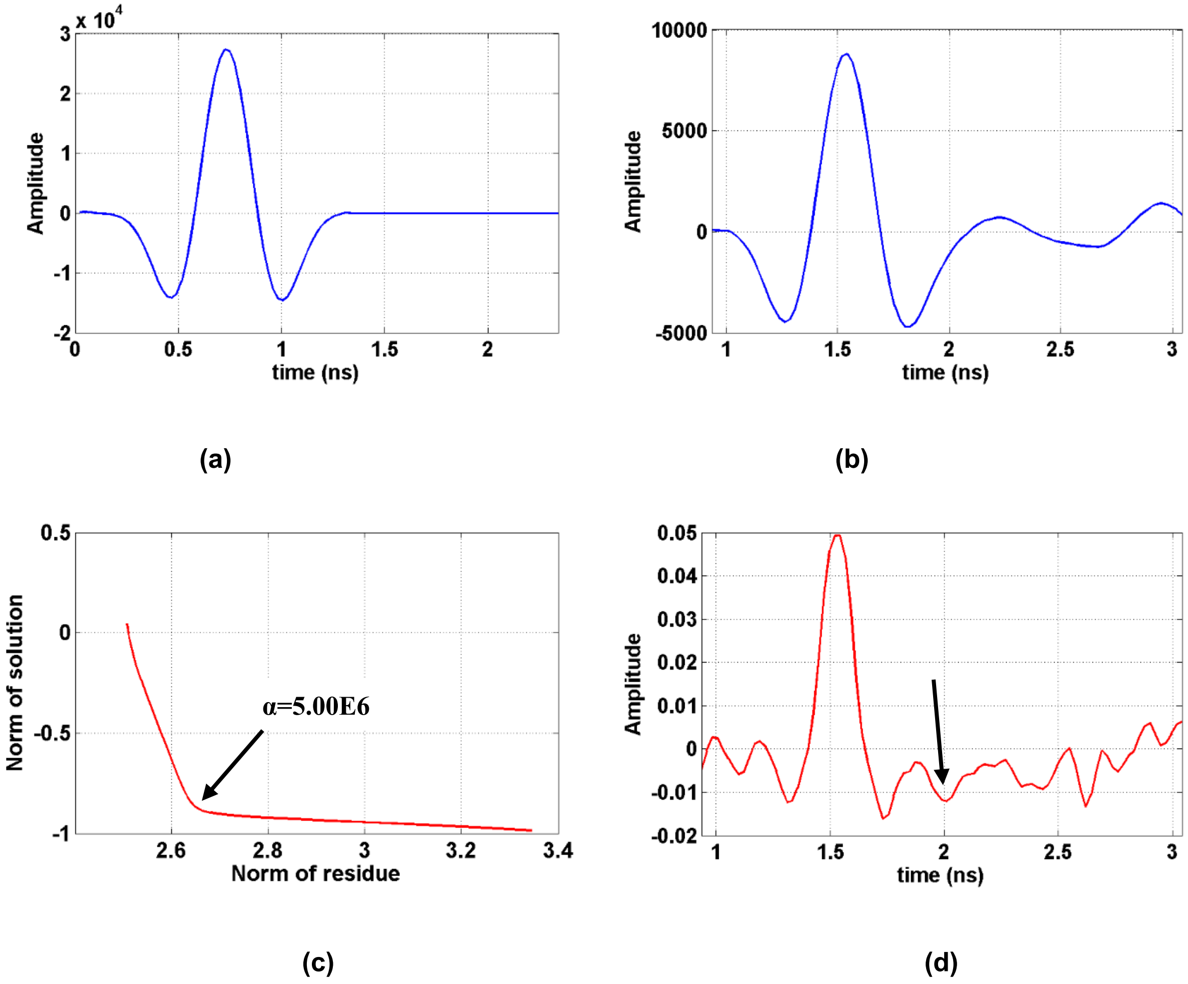

Figure 5-3 Results from 25.4-mm-quartzite section: a) Copper reflected signal b) Pavement reflected signal c) L-curve d) Impulse response.

Table 5-2 shows the results in all sections after deconvolution with regularization parameter obtained from the L-curve method. The dielectric constant of the surface asphalt layer and the EM wave velocity is determined by equations (2-12) and (2-11), respectively. For layers thinner than 38.1 mm (1.16 times of the EM wavelength), the regularization parameter *α* given by the L-curve method is larger than the optimal value, diminishing the second peak. In these cases, using a decreased α value makes the second peak clearer. All *α* values are shown in Table 5-3.

Thinner layers are more susceptible to α value; however, a reduction in α would influence the shape or the amplitude of the signal only, and does not affect the arrival time of the two peaks, which mainly affect the results. In practice, the alpha value given by L-curve method could be directly used if no further adjustments are desired.

Table 5-2 shows that for 19.1 mm thick SMA layer and the 25.4 mm quartzite layer, the thin overlay cannot be resolved using regularization. The reason is explained in section 3.2: the thin overlay cannot be resolved when the impulse distance is smaller than 0.51ns. For the 19.1 mm thick SMA layer, the impulse distance is around 0.23ns, which is much smaller than the 0.51ns threshold. The 25.4 mm thick quartzite layer has an impulse distance of around 0.3ns, which is also much smaller than 0.51ns. It should be noted that the criterion used here should not be exactly 0.51ns, since the model here is not the same as the FDTD model used in section 3.2: the dielectric constant of the wearing surface and the leveling binder are different, as is the GPR incident signal. In line with this, although the impulse distance for the other 25.4 mm and 31.8 mm layers are slightly smaller than 0.51ns, we are still able to resolve the wearing surface layer thickness using zeroth-order Tikhonov regularization.

For 50.8 mm thick F-mix layers, the error is 4.02%; for 38.1 mm thick F-mix layers, the error is -15.28%; for 31.8 mm thick layers, the errors range from -2.09% to 14.0%; and for 25.4 mm thick layers other than 25.4 mm F-mix, the error ranges from -6.71% to 15.11%.

This error can be partially attributed to the GPR system settings. During GPR data collection, the scan length of the GPR signal is set to 12 ns, and the number of samples for each scan is set to 512. The sampling resolution is 12/512=0.0234ns. The systematic error of thickness estimation is: $\delta = 0.0234\text{ns} \times \frac{3\times10^8}{\sqrt{6}}\text{m/s} \times \frac{1}{2} = 1.4\text{mm}$ (assuming the dielectric constant is 6.0). It will result in a relative error of 5.64% for a 25.4 mm thick layer.

Table 5-2 Layer Thickness Calculated after Regularization

Section	Right Lane of F-Mix-50.8						
Test No.	1	2	3	4	5	6	average
Thickness (mm)	55.1	48.8	49.8	49.5	49.8	50.5	50.5
Core thickness (mm)	52.6	45.0	50.5	48.5	47.0	48.0	48.5
error(%)	4.48%	8.44%	-1.53%	2.08%	6.32%	4.91%	4.02%
Section	Right Lane of Quartzite-31.8						
Test No.	1	2	3	4	5	6	average
Thickness (mm)	34.5	37.1	34.5	35.1	34.8	37.8	35.8
Core thickness (mm)	33.8	35.1	36.1	34.0	39.1	40.9	36.6
error(%)	2.72%	6.23%	-4.33%	3.23%	-10.75%	-7.31%	-2.09%
Section	Right Lane of Fiber/Slag-25.4						
Test No.	1	2	3	4	5	6	average
Thickness (mm)	26.9	27.4	27.4	26.4	26.4	28.2	27.2
Core thickness (mm)	28.4	28.7	28.7	29.2	29.7	30.0	29.2
error(%)	-4.94%	-4.96%	-4.12%	-9.46%	-10.65%	-6.00%	-6.71%
Section	Right Lane of Sprinkle-31.8						
Test No.	1	2	3	4	5	6	average
Thickness (mm)	35.3	36.8	36.3	36.1	37.3	35.3	36.1
Core thickness (mm)	33.5	31.0	32.0	31.5	30.5	31.2	31.8
error(%)	5.28%	18.90%	13.51%	14.33%	22.18%	13.07%	14.39%
Section	SMA-19.1						
Test No.	1	2	3	4	5	6	average
Thickness (mm)	-	-	-	-	-	-	-
Core thickness (mm)	-	-	-	-	-	-	-
error(%)	-	-	-	-	-	-	-
Section	Right Lane of F-Mix-38.1						
Test No.	1	2	3	4	5	6	average
Thickness (mm)	35.8	37.3	36.3	35.3	34.3	34.3	35.6
Core thickness (mm)	40.6	41.1	42.7	40.4	45.2	41.9	41.9
error(%)	-11.75%	-9.46%	-14.72%	-12.57%	-24.00%	-18.21%	-15.28%

Table 5-2 (cont.)

Section	Right Lane of Quartzite-25.4						
Test No.	1	2	3	4	5	6	average
Thickness (mm)	-	-	-	-	-	-	-
Core thickness (mm)	-	-	-	-	-	-	-
error(%)	-	-	-	-	-	-	-
Section	Right Lane of Fiber/Slag-31.8						
Test No.	1	2	3	4	5	6	average
Thickness (mm)	32.0	31.5	33.0	33.0	32.8	35.1	32.8
Core thickness (mm)	29.2	27.4	24.4	27.9	35.6	25.9	28.4
error(%)	10.26%	14.49%	35.63%	18.39%	-7.59%	34.78%	15.92%
Section	Right Lane of Sprinkle-25.4						
Test No.	1	2	3	4	5	6	average
Thickness (mm)	33.8	34.0	34.3	34.3	35.1	34.8	34.3
Core thickness (mm)	28.2	30.0	30.2	30.7	31.0	29.5	30.0
error(%)	20.50%	13.59%	14.20%	11.96%	12.55%	18.45%	15.11%

Table 5-3 Regularization parameter α for all sections

Section	*alpha*
Right lane of F-mix-50.8	1.30E+07
Right lane of F-mix-38.1	3.20E+07
Right lane of quartzite-31.8	8.00E+06
Right lane of quartzite-25.4	-
Right Lane of Fiber/Slag-31.8	7.90E+06
Right Lane of Sprinkle-25.4	2.00E+06
Right Lane of Fiber/Slag-25.4	2.00E+06
Right Lane of Sprinkle-31.8	7.90E+06
SMA-19.1	-

Table 5-2 shows that some sections, especially those with thin layers (25.4 mm and 38.1 mm), have greater average errors than systematic errors (5.6%). One possible reason is that when the dielectric constant is calculated based on equation (2-12), it is assumed that the first peak of the GPR signal represents the amplitude of surface reflection A_1. In this case, however, the surface reflection partially or completely overlaps with the reflection at the bottom of the surface layer because of the small layer thickness. As a result, the true value of surface reflection amplitude might be different from the amplitude of the reflection pulse shown in the signal as a result of overlapping. The inhomogeneity of the asphalt pavement layer may also contribute to the error. To reduce the error, the data from the first core out of six was used to calibrate the dielectric constant of the asphalt pavement layer. The calibrated dielectric constant was then used as the dielectric constant value at the other five core locations to calculate the layer thicknesses.

The average of dielectric constants before and after calibration are shown in Table 5-4 and Figure 5-4. It can be seen that for the 19.1 mm SMA section and 25.4 mm quartzite section, the thin overlay cannot be resolved using the regularization method, and thus it is not possible to calibrate the dielectric constant. For other sections, the dielectric constants all range from 3 to 6, which is within the typical asphalt concrete dielectric constant range. It should be noted that for some sections with the same asphalt mixture design, the dielectric constant appears different. For example, the dielectric constant of 25.4 mm Fiber/Slag section is 4.96, and the dielectric constant of the 38.1 mm Fiber/Slag is 5.84; the dielectric constant of 25.4 mm sprinkle section is 5.65, and the dielectric constant of the 38.1 mm sprinkle section is 4.41; the dielectric constant of 50.8 mm F-mix section is 5.77, and the dielectric constant of the 38.1 mm F-mix is 3.61. This could be due to many reasons, but the most plausible is that the compaction level of the two sections are different, resulting in varied density for each section. Another fact from Table 5-4 and Figure 5-4 is that the 50.8 mm F-mix and the 38.1 mm Fiber/Slag section have the largest dielectric constant; this is reasonable because from Table 5-1 we can see that the F-mix and the Fiber/Slag mix both contains metal slags, which has very large dielectric constant.

Table 5-4 Dielectric constant before and after calibration

Section	Dielectric Constant	
	before calibration (mean)	after calibration
Right Lane of Fiber/Slag-25.4	5.64	4.96
Right Lane of Sprinkle-31.8	4.03	4.41
SMA-19.1	3.67	-
Right lane of F-mix-50.8	5.48	5.77
Right lane of F-mix-38.1	4.80	3.61
Right lane of quartzite-31.8	3.98	3.78
Right lane of quartzite-25.4	4.02	-
Right Lane of Fiber/Slag-31.8	4.96	5.84
Right Lane of Sprinkle-25.4	3.77	5.65

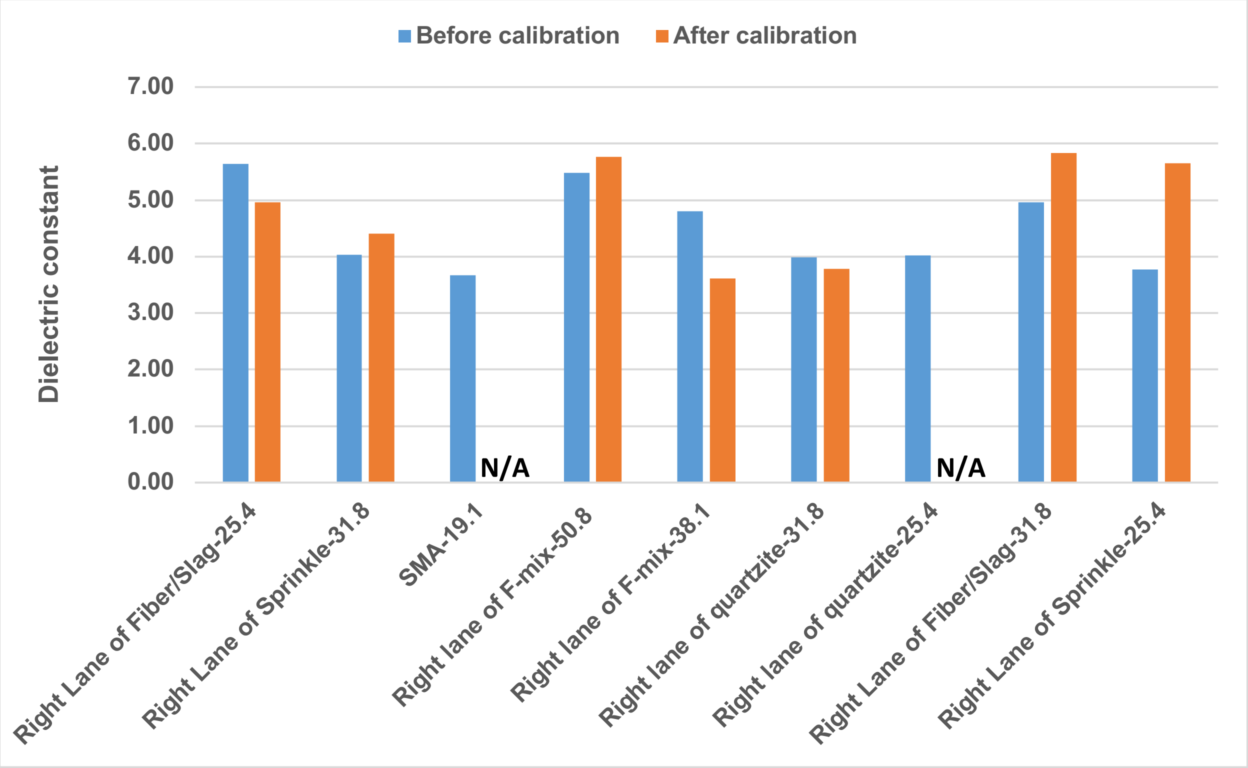

Figure 5-4 Dielectric constant from all sections before and after calibration

Table 5-5 shows the thickness estimation results across all sections using the dielectric constant obtained from core calibration. The average relative error of the 31.8 mm Sprinkle mix section is 9.43%. Nonetheless, the absolute error is still small and within the construction tolerance, because the total thin overlay thickness is small.

Figure 5-5 shows the average absolute error for all sections before and after dielectric constant calibration. After calibration, the average absolute errors from all sections are below 5 mm, which are within Illinois construction tolerances—usually 5 mm (IDOT 2012). We can also see from Figure 5-5 that other than 31.8 mm Quartzite section, the average absolute error for all other sections dropped after the dielectric constant calibration. The reason why the error doesn't change much for 31.8 mm Quartzite section is probably because the surface reflection amplitude wasn't affected much by the second reflection pulse. Similarly, for the 50.8 mm layer, the error is small (2 mm) before the dielectric constant calibration; this is because the layer thickness is large, and the surface reflection amplitude is not much affected by the second pulse.

Overall, the average absolute errors before the dielectric constant calibration ranges from 0.76 mm to 6.42 mm; while the errors after calibration ranges from 0.17 mm to 2.98 mm. Therefore, calibration can effectively reduce the mean thickness error for the sections with large estimation error due to signal overlap.

Table 5-5 Layer Thickness Regularization Results after dielectric constant calibration

Section	Right Lane of F-Mix-50.8						
Test No.	1	2	3	4	5	6	average
Thickness (mm)	52.6	48.3	48.3	48.3	48.3	49.8	49.3
Core thickness (mm)	52.6	45.0	50.5	48.5	47.0	48.0	48.5
error(%)	0.00%	7.59%	-4.53%	-0.39%	3.01%	3.49%	1.38%
Section	Right Lane of Quartzite-31.8						
Test No.	1	2	3	4	5	6	average
Thickness (mm)	33.8	36.1	34.5	34.5	34.5	36.1	34.8
Core thickness (mm)	33.8	35.1	36.1	34.0	39.1	40.9	36.6

Table 5-5 (cont.)

error(%)	0.00%	3.32%	-4.73%	1.41%	-11.98%	-11.58%	-4.34%
Section	Right Lane of Fiber/Slag-25.4						
Test No.	1	2	3	4	5	6	average
Thickness (mm)	28.4	28.4	30.0	28.4	28.4	30.0	29.0
Core thickness (mm)	28.4	28.7	28.7	29.2	29.7	30.0	29.2
error(%)	0.00%	-1.38%	4.46%	-2.74%	-4.05%	0.27%	-0.60%
Section	Right Lane of Sprinkle-31.8						
Test No.	1	2	3	4	5	6	average
Thickness (mm)	33.5	35.1	35.1	35.1	35.1	33.5	34.5
Core thickness (mm)	33.5	31.0	32.0	31.5	30.5	31.2	31.8
error(%)	0.00%	13.47%	9.93%	11.67%	15.33%	7.03%	9.43%
Section	SMA-19.1						
Test No.	1	2	3	4	5	6	average
Thickness (mm)	-	-	-	-	-	-	-
Core thickness (mm)	-	-	-	-	-	-	-
error(%)	-	-	-	-	-	-	-
Section	Right Lane of F-Mix-38.1						
Test No.	1	2	3	4	5	6	average
Thickness (mm)	40.6	42.7	40.6	40.6	40.6	40.6	40.9
Core thickness (mm)	40.6	41.1	42.7	40.4	45.2	41.9	41.9
error(%)	0.00%	3.53%	-4.68%	0.75%	-9.95%	-3.09%	-2.40%
Section	Right Lane of Quartzite-25.4						
Test No.	1	2	3	4	5	6	average
Thickness (mm)	-	-	-	-	-	-	-
Core thickness (mm)	-	-	-	-	-	-	-
error(%)	-	-	-	-	-	-	-
Section	Right Lane of Fiber/Slag-31.8						
Test No.	1	2	3	4	5	6	average
Thickness (mm)	29.2	29.2	30.5	30.5	30.5	32.0	30.2
Core thickness (mm)	29.2	27.4	24.4	27.9	35.6	25.9	28.4
error(%)	0.00%	6.20%	25.74%	9.51%	-13.93%	23.11%	6.86%
Section	Right Lane of Sprinkle-25.4						
Test No.	1	2	3	4	5	6	average
Thickness (mm)	28.2	28.2	28.2	28.2	28.2	28.2	28.2
Core thickness (mm)	28.2	30.0	30.2	30.7	31.0	29.5	30.0
error(%)	0.00%	-6.02%	-6.64%	-8.47%	-9.64%	-4.42%	-5.97%

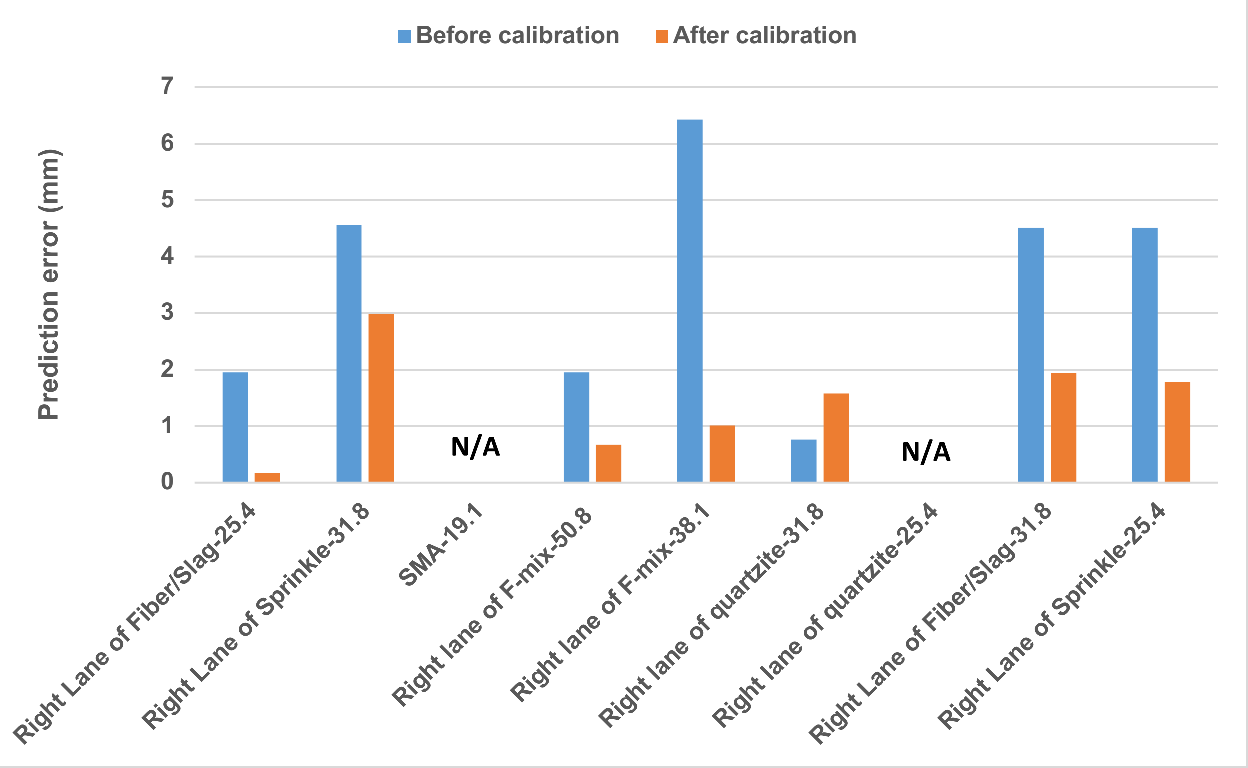

Figure 5-5 Average absolute error for all sections before and after dielectric constant calibration

5.4 Discussion

Regularized deconvolution is an algorithm that could be used on GPR signals to calculate the impulse response of the pavement system. This approach would increase the resolution of overlapped pulses, and address the “thin layer challenge” (the problem of predicting pavement layer thickness, which is comparable to the wavelength of the EM pulse). GPR measurements were taken at six static coring locations in each section during a survey conducted on newly built AC overlays with different mixture types and thicknesses on IL-72 in Hoffman Estates, Illinois and Barrington, Illinois. The regularized deconvolution method was utilized on raw GPR signal using the regularization parameter α given by L-curve method. One of six data points was used to calibrate the dielectric constant of asphalt concrete layer. The thickness calculated using regularized deconvolution was then compared with the ground truth from coring. The proposed zeroth-order Tikhonov regularization showed good results across sections except for two: the 19.1 mm thick SMA section and the 25.4 mm thick quartzite section. Among all other sections, the maximum error was 2.98 mm, well below Illinois state construction tolerances.

In summary, the error in predicting the thin asphalt layer thickness using the regularized deconvolution algorithm is acceptable and less than the construction tolerance (usually 5 mm in the State of Illinois). The regularized deconvolution of GPR signal can be used to accurately predict asphalt layer thickness at different noise levels. It is also a simple and effective technique for addressing the “thin layer challenge.”

5.5 Summary

In this chapter, the zeroth-order Tikhonov regularization was applied on real GPR data collected from newly constructed AC overlay. There are nine construction sections, and each section had a different mixture design and design thickness. The thicknesses found by the regularization method were compared to coring data, and it was found that pulse overlapping led to inaccuracies in the dielectric constant calculations. The dielectric constants of each section were then calibrated using one out of six cores. It was found that after dielectric constant calibration, the thickness estimation errors were below 3 mm, well within construction tolerance. Due to the limitations of the regularization method, it failed to resolve thin overlay thickness in two sections, whose thicknesses are 25.4 mm and 19.1 mm respectively.

The limitation of the regularized deconvolution method is that when the layer thickness is below a certain critical threshold, the regularization method is unable to resolve the thin layer. This critical threshold—typically between 12.7 mm to 38.1 mm—depends on the type of incident signal of the GPR and the dielectric constant of surface course and leveling course.

This study is therefore oriented in two directions: one problem is to find an approach that can be used to calculate the dielectric constant of the thin AC overlay without the need of calibration. A second problem is to find a method to recover TWTT when the layer thickness is below the critical threshold. The first problem will be discussed in Chapters 6 and 7, with the second problem also being discussed in Chapter 7.

CHAPTER 6: SUPER-RESOLUTION OF 3-D GPR SIGNALS TO ESTIMATE THIN AC OVERLAY THICKNESS USING XCMP METHOD

6.1 Background and Objective

The linear inversion techniques discussed in Chapters 4 and 5 can be used to accurately determine the TWTT of GPR signals within thin AC overlay. However, these techniques cannot be used find the dielectric constant of the thin AC overlay due to the inaccurate surface reflection amplitude. In Chapter 5, the dielectric constants of the thin AC overlay were back calculated using core data—a destructive process. To address these concerns, this chapter uses an extended common midpoint method to calculate the dielectric constant of the thin AC overlay without the need of back calculation.

In section 6.2, the methodologies will be explained. In section 6.3, an experiment study is conducted and the results are discussed. Section 6.3 summarizes this chapter.

6.2 Methodology

The conventional way to estimate AC layer thickness involves two steps: the prediction of the dielectric constant of the AC pavement layer using the surface reflection method (Al-Qadi et al. 2001) and the calculation of the AC layer thickness using the two-way travel time (TWTT) method. The main issue with this approach is that the dielectric constant cannot be accurately estimated due to several factors that can affect the surface reflection amplitude, such as surface moisture and signal overlapping. Calibrating the dielectric constant by taking cores is one way to improve the dielectric constant estimation accuracy; however, it is destructive. Multi-offset methods such as the common midpoint (CMP) method have been recently used to calculate asphalt pavement thicknesses (Liuzzo-Scorpo and Cook 2017). A novel approach, the modified common midpoint (MCMP) method, was developed by Al-Qadi and his research group (Lahouar et al. 2002). The approach uses one bi-static antenna and one mono-static antenna to find the dielectric constant and AC layer thickness without the need for coring calibration. Wright et al. (2014) explored the possibility of using two air-coupled antennas for pavement dielectric constant and thickness measurement; however, they assumed linear wave paths of the EM wave, and the method is therefore not accurate. A more generic algorithm was proposed by Leng and Al-Qadi (2014), and the modified method was referred to as XCMP method.

The XCMP method requires accurate determination of the peak location in the GPR signal. This becomes an issue when the AC layer is thin (such as thin AC overlay) compared with the signal wavelength, since the GPR signals do not have sufficient resolution to resolve two adjacent peaks. To this end, this chapter aims to increase the resolution of the GPR signals for thin AC overlay thickness estimation using super-resolution algorithms.

In this chapter, a new multi-channel 3-D GPR was used to collect signals from a full-scale AC overlay test section, and the estimated overlay thickness was compared with the ground truth.

6.2.1 Extended common midpoint method

The XCMP method is one of the multi-offset profiling techniques originally used in seismic wave processing (Yilmaz 2001). The basic setup of the XCMP method is shown in Figure 6-1. "Tx_1/Rx_1" and "Tx_2/Rx_2" are the transmitter/receiver pairs for Channel 1 and Channel 2, respectively. Both channels are at distance d from the ground surface. The antenna offset for Channel 1 and Channel 2 are x_{01} and x_{02}, respectively. Both channels share the same midpoints, P_1 and P_2. The dielectric constants of the air and the AC are $\varepsilon_0 = 1$ and ε_1, respectively. For both channels, the GPR signals reflect from the surface of the AC overlay and the bottom of the AC overlay, as indicated by the dotted path and solid path, respectively. t_1 and t_2 are the time EM wave travels in the pavement for Channel 1 and Channel 2, respectively. Other geometrical information is also indicated in Figure 6-1.

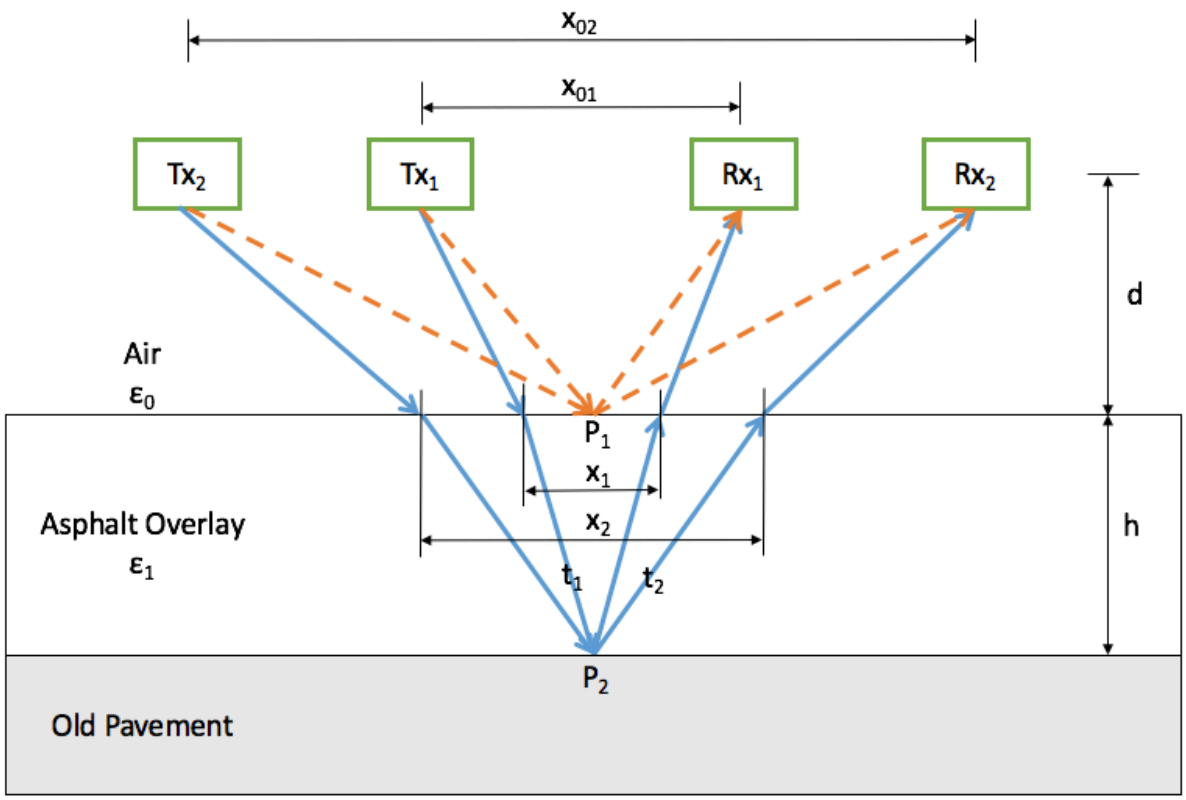

Figure 6-1 Setup of XCMP method with 2 bi-static air-coupled antenna channels.

The XCMP problem has two unknowns: the thickness of the AC overlay, h, and the dielectric constant of the asphalt overlay, ε_1. Obtaining two AC overlay bottom reflection times from two channels can fully determine the two unknowns. Based on the Snell's law of reflection and refraction, the solution of the problem is derived as follows:

$$\left(\frac{x_{01}-x_1}{2d}\right)^2 + 1 = \frac{t_1^2(x_2^2-x_1^2)^2}{t_1^2(x_2^2-x_1^2)^2-x_1^2c^2(t_2^2-t_1^2)^2}, \tag{6-1}$$

$$\left(\frac{x_{02}-x_2}{2d}\right)^2 + 1 = \frac{t_2^2(x_2^2-x_1^2)^2}{t_2^2(x_2^2-x_1^2)^2-x_2^2c^2(t_2^2-t_1^2)^2}, \tag{6-2}$$

$$\Delta t_1 = t_1 + \frac{2\sqrt{d^2+(x_{01}-x_1)^2/4}}{c} - \frac{2\sqrt{d^2+{x_{01}}^2/4}}{c}, \tag{6-3}$$

$$\Delta t_2 = t_1 + \frac{2\sqrt{d^2+(x_{02}-x_2)^2/4}}{c} - \frac{2\sqrt{d^2+{x_{02}}^2/4}}{c}, \tag{6-4}$$

where c=3*10^8m/s is the speed of EM waves in free space, Δt_1 and Δt_2 are the time difference of the EM wave between surface reflection and reflection at the bottom of the overlay for Channel 1 and Channel 2, respectively, as shown in Figure 6-2. To increase the precision of the obtained Δt_1 and Δt_2, it is necessary to interpolate the GPR signals, such as using Whittaker-Shannon interpolation (Lyons 2011). However, since the MUSIC algorithm has O(n^3) time complexity, interpolating the original signal greatly increases the computation time. It should be noted that if the AC overlay is relatively thin, Δt_1 and Δt_2 may not be resolved due to pulse overlapping. The solution of this problem, super-resolution, is discussed in the next section.

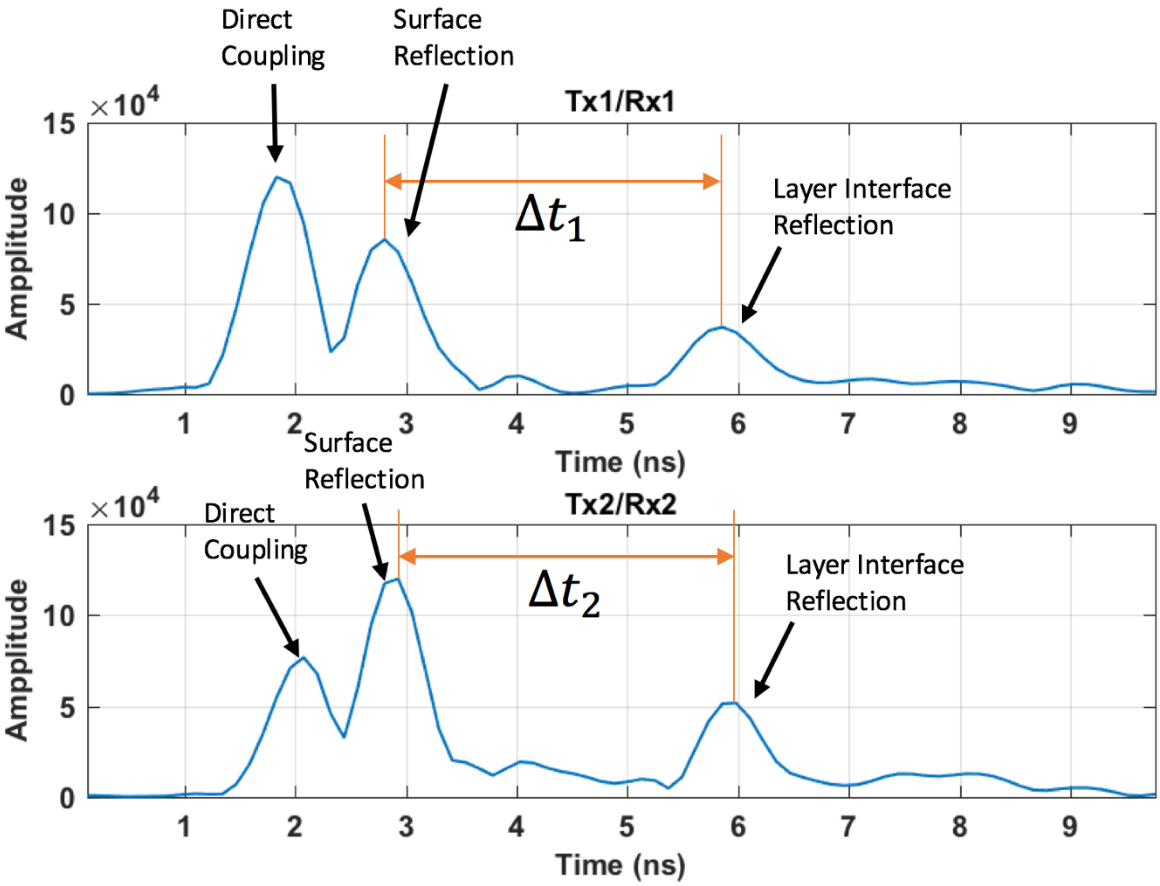

Figure 6-2 A-scan reflection from both XCMP channels.

From the four aforementioned equations, the four unknowns, x_1, x_2, t_1, and t_2 may be solved numerically. The dielectric constant and AC layer thickness can then be determined by

$\varepsilon_1 = \frac{c^2(t_2^2-t_1^2)}{x_2^2-x_1^2}$ and $vt_1 = 2\sqrt{h^2 + (x_1/2)^2}$, where v is the EM wave speed in the AC overlay. The complete signal processing process used to solve XCMP problem is shown in Figure 6-3. Whether an asphalt layer is a thin layer or not depends on both the layer thickness and the resolution of the GPR signal. The details will be discussed in next section.

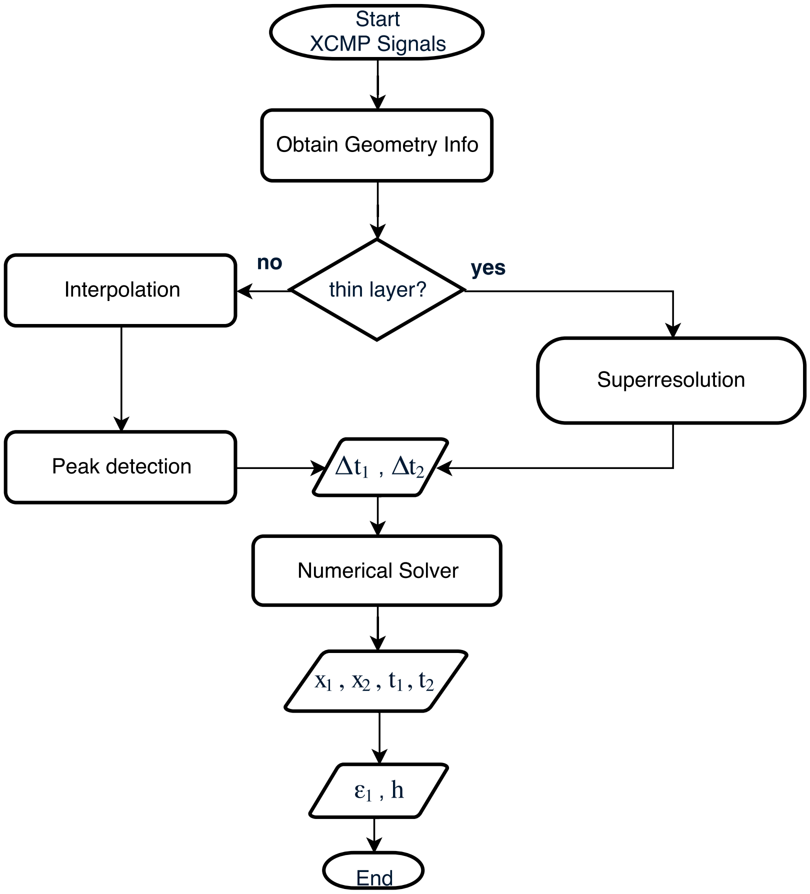

Figure 6-3 Complete signal processing scheme for XCMP problem.

6.2.2 Subspace approach

When measuring AC layer thickness, whether using the conventional two-way travel time method or the XCMP method, the key factor for the GPR performance is the antenna range resolution, since the AC pavement layer can be considered a 1-D target in the vertical direction.

Therefore, it is preferable to use a wide-band antenna such as a horn antenna or an ultra-wide-band antenna such as a bow-tie antenna, commonly used in GPR (Stutzman and Thiele 2012).

Due to the upper limit of the bandwidth of the commercial GPR antenna, signal processing techniques, known as super-resolution techniques, are needed to increase range resolution. The importance of the resolution of GPR signal and the available super-resolution algorithms including regularization is discussed in Sections 4.2.2 and 4.2.3.

Another class of method for time delay estimation (TDE) is the subspace approach. For example, MODE (Method of Direction Estimation) and WRELAX (Weighted Fourier transform and RELAXation) are both TDE methods based on eigen-analysis (Wu et al. 1999; Wu et al. 2002). In this chapter, the MUSIC (multiple signal classification) algorithm was used. It was originally used to determine the direction of arrival (DOA) of multiple waves arriving at an antenna array (Schmidt 1986). The method was applied to perform TDE from time domain data (Bruckstein et al. 1985) and from frequency domain data (Le Bastard et al. 2007). In both cases, the MUSIC method allows for the increase of time resolution and helps to separate overlapping signals in the time domain. Time domain MUSIC was conventionally applied on oscillating signals with zero mean; however, the MUSIC algorithm has also been used for non-negative signals. For example, Marengo et al. (2007) applied the signal-subspace method on intensity-only data (lacking field phase information). The performance of TDE could be possibly improved when additional phase information is available. Bruckstein et al. (1985) used time domain MUSIC on triangular and Gaussian pulses, producing a time-delay estimation result of high accuracy. Bastard et al. (2007) applied this method for thin AC pavement layer thickness estimation; the super time resolution capability of MUSIC was demonstrated on artificial materials in laboratory and not on real pavement materials as opposed to the work which is developed in this study and in Wu et al. (1999) and Wu et al. (2002).

The MUSIC algorithm relies on the eigenstructure of the received signal covariance matrix. Similar to equation (4-2), one can discretize equation (4-1) as follows:

$$\vec{y} = \boldsymbol{H}\vec{x} + \vec{n}, \tag{6-5}$$

where $\vec{x} \in \mathbb{C}^{m\times 1}$ is vector of x(t), $\vec{n}$ is the noise vector, and $\boldsymbol{H} \in \mathbb{C}^{(m+n-1)\times m}$ is the Toeplitz matrix constructed from h(t). The covariance of the received signal is computed by:

$$\boldsymbol{S}_y = \vec{y}\vec{y}^H = (\boldsymbol{H}\vec{x} + \vec{n})(\boldsymbol{H}\vec{x} + \vec{n})^H, \tag{6-6}$$

where $\boldsymbol{S}_y \in \mathbb{C}^{n\times n}$ are the covariance matrices of signal y(t). The superscript "H" represents a Hermitian transpose.

The MUSIC algorithm then assumes that the signal subspace is the span of vectors associated with the k principal component (Jolliffe 1986) of matrix $\boldsymbol{S}_y$, where k is the number of pulses in y(t). For example, for a two-layered pavement system, k = 3 (i.e., direct coupling, surface reflection, and bottom of the surface reflection). If the prior of the number of delayed echoes is unknown, Wax and Kailath (1984) propose a method using information theory such as Akaike information criterion (AIC; Akaike 1974) to determine the number of signals. They then assume that the noise subspace is orthogonal complement of the signal subspace. The signal subspace can be found by the singular value decomposition of matrix $\boldsymbol{S}_y$:

$$\boldsymbol{S}_y = \boldsymbol{U\Sigma V}^H, \tag{6-7}$$

where $\boldsymbol{U}, \boldsymbol{V} \in \mathbb{C}^{n\times n}$ are both unitary matrix, $\boldsymbol{\Sigma} = \text{diag}(\sigma_1, \sigma_2, \dots, \sigma_n)$. The diagonal elements $\sigma_1 \geq \sigma_2 \geq \cdots \geq \sigma_n$of $\boldsymbol{\Sigma}$ are the singular values of $\boldsymbol{S}_y$. It is then clear that the signal subspace is the span of $\{\vec{v}_i\}_{i=1,2,\dots,k}$, and the noise subspace is the span of $\{\vec{v}_i\}_{i=k+1,k+2,\dots,n}$, where $\vec{v}_i$ is the i^th^ column of $\boldsymbol{V}$. For the time delays, $\theta \epsilon [0, T]$ is searched over by measuring the following orthogonality, which is the distance between the delayed signal and the noise subspace:

$$P_{MUSIC}(\theta) = \frac{\vec{x}_\theta * \vec{x}_\theta}{\sum_{i=k+1}^{n} (\vec{x}_\theta * \vec{v}_i)^2}, \tag{6-8}$$

where $\vec{x}_\theta$ is the incident signal $\vec{x}$ delayed by θ, i.e. $\vec{x}(t - \theta)$. Since the MUSIC algorithm assumes that the signal subspace is orthogonal to the noise subspace, when the orthogonality in equation (6-8) is at a local maximum, the θ value corresponds to the true time delay of the signal. Performing the MUSIC algorithm may also be done in the frequency domain such as in Le Bastard et al. (2007) if the signal frequency content is coherent throughout the whole bandwidth.

From the above discussion, it is clear that the MUSIC algorithm requires each signal in the signal subspace to be linearly independent. However, this may not be satisfied in practice since the signals reflected from each layer interface may be correlated with one another. In this study, the spatial smoothing method is used on the signal covariance matrix to de-correlate the signals. Algorithms like SSP (Shan et al. 1985) and MSSP (Williams et al. 1988) demonstrate good performance as preprocessing techniques when MUSIC is used for frequency estimation (Yamada et al. 1991). The idea of the spatial smoothing algorithms is to take consecutive subarrays of the received signal $\vec{y}$ find the covariance matrix of each subarray, and then average them. The spatial smoothing preprocessing reduces the dimension of the signal space. It was found that spatial smoothing is most effective for thin pavement thickness estimation when the subarray length is around 84% of the received signal.

6.3 Experiment Study

6.3.1 Test plan

To validate the XCMP method, the authors (Zhao and Al-Qadi 2016) collected 3-D GPR data on a test section as shown in Figure 6-4. The test site has four sections, and each section is

3.35m by 3.35m. The design thicknesses of the four sections are 50, 100, 150, and 200 mm, respectively. Thin steel plates were embedded between each AC lift and were used to increase the reflection coefficient of the GPR signals. There are transition zones between each section due to construction need. Cores were taken at the center of each steel plate for validation purposes.

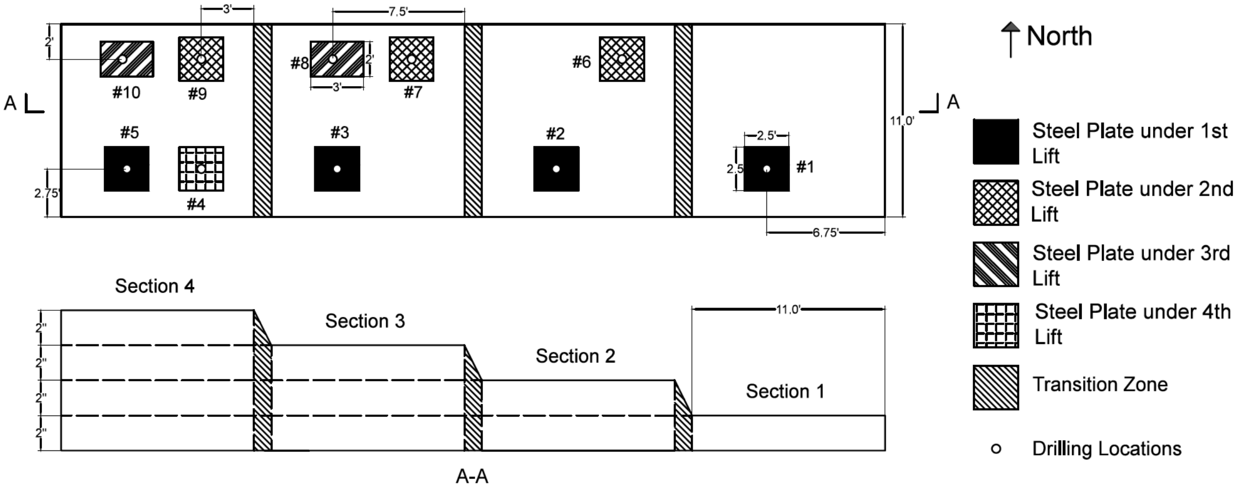

Figure 6-4 Illustration of the pavement test section and coring location.

A DX1821 3-D GPR manufactured by 3D-Radar company was used. The 3-D GPR used stepped frequency signals, and the time domain signal was obtained by inverse Fourier transform. Only processed non-negative time domain signals could be accessed from the 3-D GPR software. An illustration of the 3-D GPR antenna array is shown in Figure 6-5. The antenna array had 11 transmitting antennas (Tx) and 11 receiving antennas (Rx). The width of the antenna array was 1.8 m. Each of the antennas was a bow-tie antenna with a frequency band from 200 MHz to 3 GHz. A total of 21 channels existed in the standard survey pattern, as represented by the dashed lines in Figure 6-5. A XCMP configuration was used, denoted by the solid lines in Figure 6-5. For the XCMP configuration shown in Figure 6-5, the offset between Tx and Rx antennas are 0.446 m and 0.685 m for each channel, respectively. Two GPR surveys were conducted at the north half and south half of the test lane to cover the whole lane.

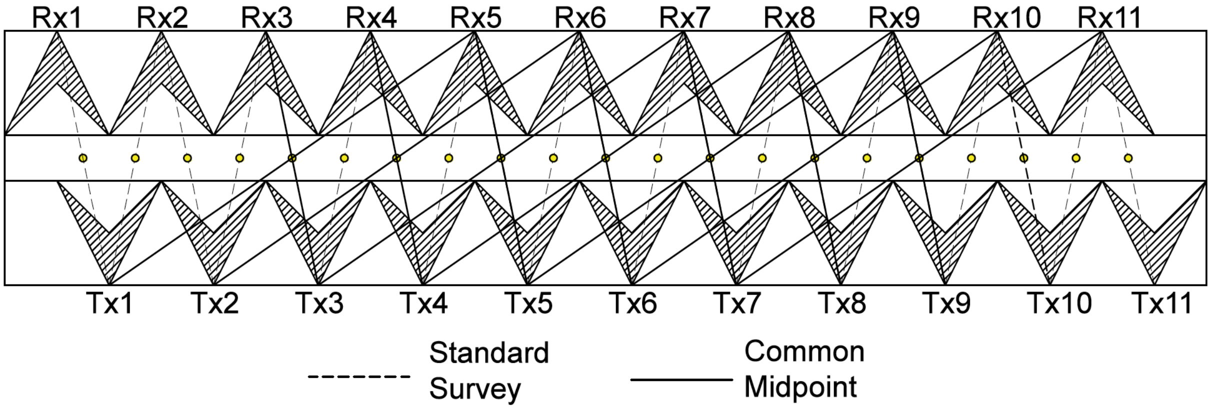

Figure 6-5 3-D antenna array, standard and XCMP survey pattern.

In a previous study, Zhao and Al-Qadi (2016) found that by using the XCMP configuration shown in Figure 6-5, the AC layer thickness at steel plate locations #2, #3, #5, #7, #9, and #10 can be estimated with an average error of 3.45%. For steel plate location #1, the signal reflected from the bottom of the first lift overlapped with the surface reflection; for steel plate locations #4, #6, and #8, the time delay estimation accuracy was not high enough to perform XCMP due to the relatively thin AC layer, even though there were no overlapped pulses. In this study, the super-resolution algorithm MUSIC was applied on GPR signals from steel plated locations #1, #4, #6, and #8 to increase the time resolution of the GPR signal, and, as a result, to improve the accuracy of the time delay estimation and the XCMP results.

6.3.2 Test result

Using the XCMP configuration shown in Figure 6-5, 14 radargrams, or B-scans, were collected for each north and south half of the lane. By locating the center of the steel plate, only the channels measuring along the centerline of the steel plates were selected. The four radargrams (two for north section and two for south section) are shown in Figure 6-6. Figure 6-6(a) is the radargram of the north half of the section collected from channel Tx7/Rx7. The two shallow steel plates, #6 and #8, are marked by arrows. Figure 6-6(b) is the same section, but collected by channel

Tx5/Rx9. Both channels together form the configuration for the XCMP method. Similarly, Figures 6-6(c) and 6-6(d) are the radargrams of the south half of the pavement, and the two shallow plates, #1 and #4, are also marked by arrows.

In the four radargrams shown in Figure 6-6, the first perfect horizontal line is the direct coupling pulse (signal transmitted directed from transmitter to receiver). The second horizontal line is the reflection from the surface of the pavement. We can clearly see the ten steel plates (white rectangles); however, for steel plates #1, #4, #6, and #8, the signals reflected from the steel plate were either very close to the surface reflection, or overlapped with the surface reflection (such as in #1 in Figures 6-6(c) and 6-6(d)). Also, there were noises due to the echoes of the signals reflected either from the pavement surface or the steel plates.

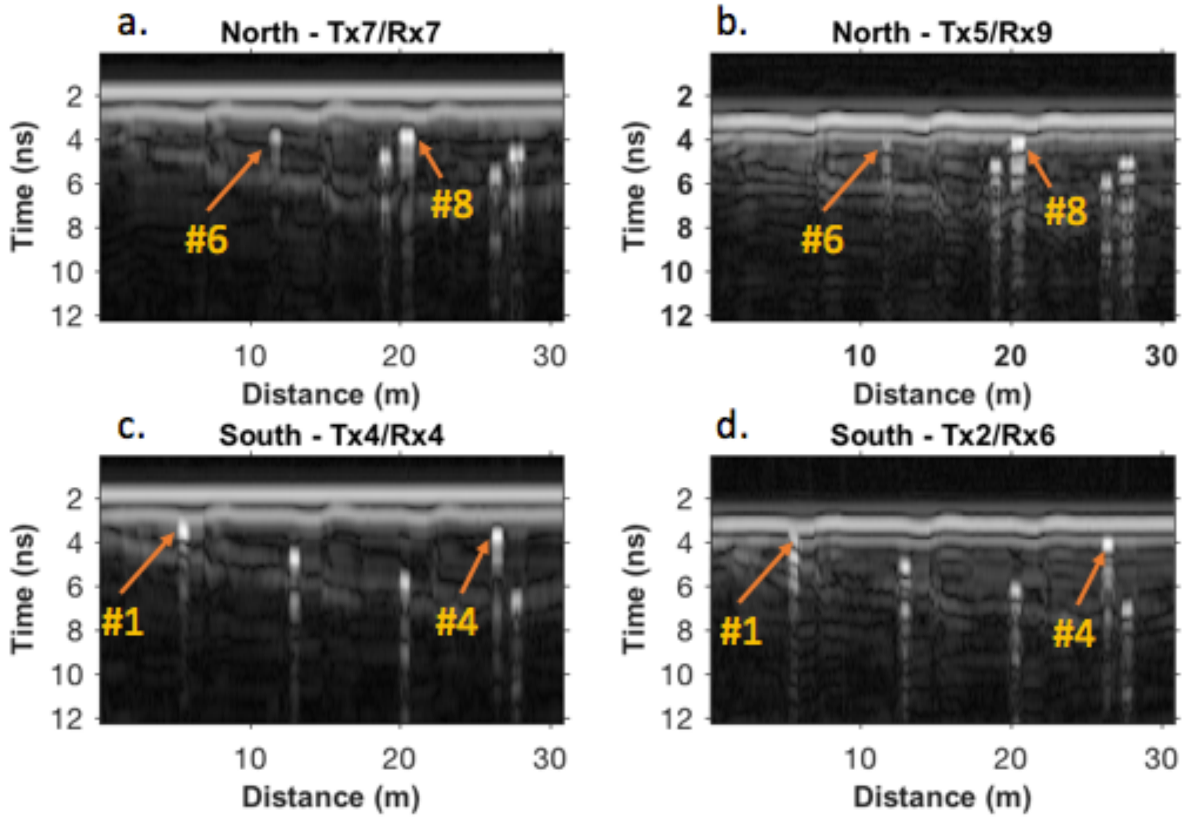

Figure 6-6 Radargrams from the XCMP configuration: (a) north half of the pavement by Tx7/Rx7, (b) north half of the pavement by Tx5/Rx9, (c) south half of the pavement by Tx4/Rx4, and (d) south half of the pavement by Tx2/Rx6.

An example of an A-scan collected from steel plate #1 by Tx4/Rx4 is shown in Figure 6-7(a). There, the surface reflection and the steel plate reflection overlapped, which can also be observed in Figure 6-6(c).

The zero-th order Tikhonov regularization was first applied as shown in equation (4-8) to the GPR signal, and the regularization result is shown in Figure 6-7(b). The original time domain signals are non-negative since only the signal magnitude was calculated using the frequency domain information. Therefore, we used a non-negative optimization method: the active set method developed by Lawson and Hanson (1995). Figure 6-7(b) shows that the once-overlapped surface reflection and steel plate reflection are clearly separated between 2 ns and 3 ns. The first peak at around 1 ns is the coupling pulse. We then found that although the regularization could improve the resolution of the GPR signal, the estimated time delay difference based on Figure 6-7(b) is not accurate and precise enough for performing XCMP analysis.

The MUSIC algorithm shown in equation (6-8) was then applied to the signal shown in Figure 6-7(a), and the P_{MUSIC} was plotted versus the time delay as shown in Figure 6-7(c). The incident signal $\vec{x}(t)$ was obtained by truncating the pavement surface reflection. The three peaks shown in the plot from left to right correspond to the direct coupling pulse, surface reflection, and the steel reflection, respectively. The advantage of the MUSIC algorithm is that the result can have very large sampling rate, since any time delay number θ can be selected in equation (6-8). This gives the TDE more precision.

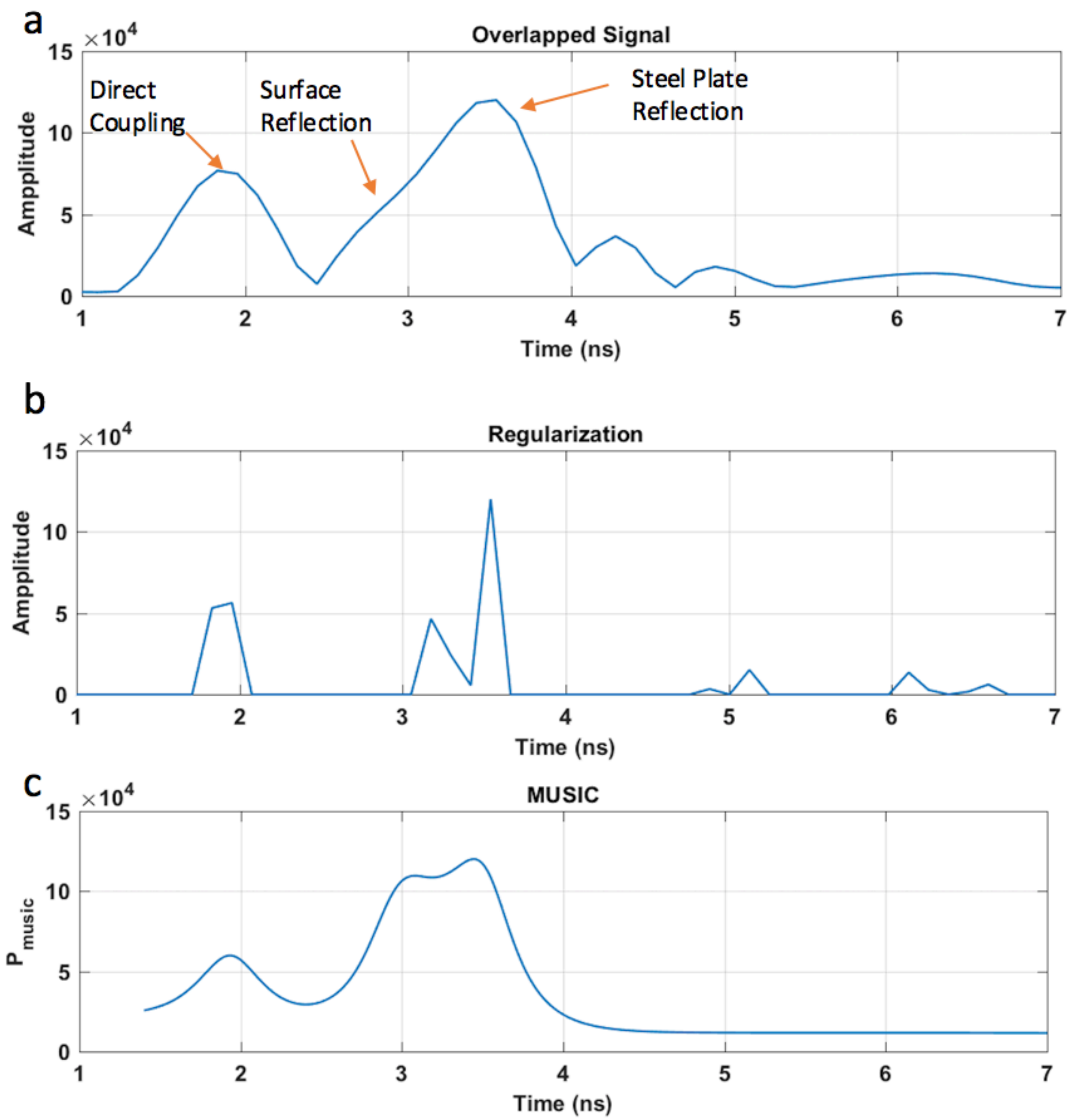

Figure 6-7 Super-resolution results: (a) overlapped XCMP signal, (b) regularization result, and (c) MUSIC algorithm result.

To reduce the effect of echoing noises, signals beyond 9.5 ns were truncated, as shown in Figure 6-2. The complete MUSIC algorithm is summarized in Figure 6-8. The coupling pulses were not removed due to the overlapping with the surface reflection. However, since coupling pulses are received in the antenna near field, the frequency spectrum of the coupling pulse is usually different than the incident wave. As a result, the assumption that a pavement reflection system that includes direct coupling is a linear one, may contribute to the system error of the MUSIC results.

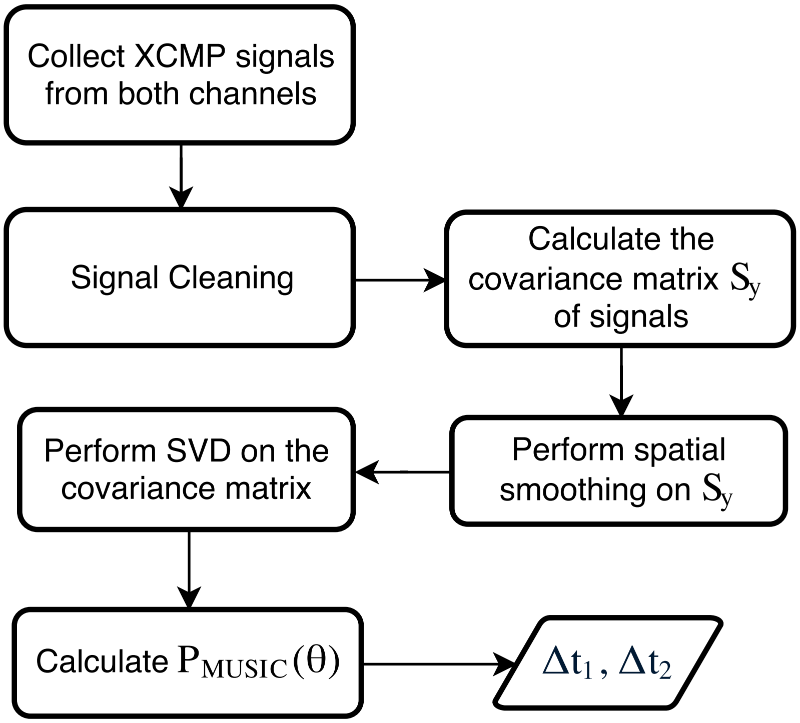

Figure 6-8 MUSIC algorithm flowchart.

In this study, only the AC overlay thickness is of concern. The thickness prediction results from 10 steel plate locations are shown in Table 6-1. The time delays Δt_1 and Δt_2 are also shown in Table 6-1. For steel plates #2, #3, #5, #7, #9, and #10, the AC overlay thickness prediction error ranged from -5.41% to 8.74%. The absolute error at steel plate #9 was large because of the effect of echoing of the surface reflection.

For steel plates #1, #4, #6, and #8, when the super-resolution method was not used, the XCMP also did not return solutions due to inaccurate time delay estimation. In these cases, the MUSIC algorithm was used for preprocessing. Following the MUSIC algorithm, the AC overlay thickness prediction errors were -2.81%, 5.09%, 2.74%, and -5.38% for steel plate locations #1, #4, #6, and #8, respectively. For those four locations, the maximum absolute prediction error was

4 mm. This error number is considered better than values obtained from cores and within the acceptable resolution for QC/QA, which is usually 6.25-12.5 mm.

Table 6-1 Thickness prediction results

Steel plate no.	1	2	3	4	5
Δt_1	0.76	1.95	3.04	1.10	3.89
Δt_2	0.75	1.92	2.99	1.09	3.83
Dielectric constant	7.07	7.27	6.68	7.03	7.27
Predicted thickness (mm)	44	110	180	64	220
True thickness (mm)	45	114	178	60	221
Error (mm)	-1	-4	2	4	-1
Error (%)	-2.81%	-3.21%	0.75%	5.09%	-0.45%
MUSIC algorithm?	Yes	No	No	Yes	No
Steel plate no.	6	7	8	9	10
Δt_1	1.16	2.09	1.06	2.88	1.96
Δt_2	1.15	2.02	1.04	2.84	1.93
Dielectric constant	7.40	6.61	7.31	6.03	7.65
Predicted thickness (mm)	65	124	60	180	108
True thickness (mm)	64	121	63	165	114
Error (mm)	1	3	-3	15	-6
Error (%)	2.74%	2.95%	-5.38%	8.74%	-5.41%
MUSIC algorithm?	Yes	No	Yes	No	No

6.4 Summary

The XCMP method allows for the calculation of the dielectric constant of AC pavement without the need for calibration. Previous studies have used the method to predict AC pavement thickness. One challenge of the XCMP method is that it requires the accurate determination of the time delay estimation when the AC layer is thin at the GPR frequency level. In this chapter, the MUSIC method was discussed and compared to the regularization method discussed in Chapters 4 and 5.

A full-scale AC overlay section was built with design thicknesses ranging from 50 mm to 200 mm. Ten steel plates were embedded in the pavement layers to increase the reflection amplitude. 3-D GPR was used in the study to perform XCMP method, with an optimized XCMP configuration we designed.

The proposed super-resolution algorithms were then applied on the XCMP signals. Before the MUSIC algorithm was applied, signal preprocessing techniques, including data cleaning and spatial smoothing, were first performed to increase the signal-noise ratio (SNR) of the signal. The predicted AC layer thicknesses were then compared with ground truth values.

The findings of this study are summarized as follows:

- For thin AC overlay, super-resolution techniques are needed for accurate determination of the signal time delay.
- The regularization method's time delay estimation may not always provide enough accuracy and precision for the XCMP method. However, the MUSIC algorithm can increase the resolution of the GPR signals collected from thin AC overlay, and achieve higher accuracy and precision in the time delay estimation.
- The maximum absolute AC layer thickness prediction error, when the MUSIC algorithm is applied, is 4 mm.
- In practice, the XCMP method can be successfully used with 3-D GPR to predict AC layer thickness and its dielectric constant.

This chapter shows that the MUSIC algorithm can increase the time resolution of the GPR signal such that XCMP method can be applied on thin AC overlay to predict its dielectric constant and thickness. The proposed XCMP and MUSIC algorithm need to be further validated on AC overlay without embedded steel plates.

CHAPTER 7: PREDICTION OF THIN ASPHALT CONCRETE OVERLAY THICKNESS AND DENSITY USING NONLINEAR OPTIMIZATION

7.1 Background and Objective

At the end of Chapter 5, two challenges were raised: one is to accurately estimate the dielectric constant of the thin AC overlay, and the second is to find the TWTT of GPR pulses when the thickness of overlay is very small. Chapter 6 provides a method to estimate the thin AC overlay dielectric constant using the XCMP and subspace methods.

In this chapter, a non-linear gradient descent approach will be used to find both the dielectric constant and TWTT when the layer thickness is very small, and the thin AC overlay thickness and density are calculated. Both FDTD simulation and field tests were conducted to validate the proposed algorithm. The simulation showed that the accuracy of dielectric constant estimation increased after the nonlinear gradient descent method was applied. This resulted in a thickness estimation error of less than 1 mm. When nonlinear gradient descent was applied to field test measured signals, the average AC overlay thickness prediction and AC density estimation errors were 3 mm and 1.81%, respectively. This demonstrates that the nonlinear gradient descent is an effective approach for estimating thin AC overlay thickness and density from GPR data.

In Section 7.2, we develop the nonlinear gradient descent method. In Section 7.3, we provide an FDTD simulation, while Section 7.4 concerns a field test we conducted. Section 7.5 concludes by summarizing the proposed method.

7.2 Methodology

In Chapter 4, it was shown that the received GPR signal reflected from pavement can be viewed as the convolution of the incident signal and the pavement impulse response (equation (4-1)). The regularized deconvolution method used in Chapters 4 and 5 can recover the pavement impulse, and the method is fast and robust to noise. However, it was found that regularized deconvolution only works when the AC layer is thicker than 25 mm, and that it is not able to accurately recover the amplitude of the surface reflection; this leads to inaccurate AC overlay density estimation.

In this study, instead of the linear optimization approach used in regularized algorithms, a nonlinear gradient descent approach is proposed to obtain thin AC overlay thickness and to find the surface reflection amplitude to calculate an accurate dielectric constant as well. In the case of two-layered AC pavement, equation (4-1) may be simplified as:

$$y(t) = x(t) * [R_1\delta(t) + R_2\delta(t-\Delta t)] = R_1x(t) + R_2x(t-\Delta t), \tag{7-1}$$

where $\delta(t)$ is the Dirac Delta function, and R_1 and R_2 are the EM reflection scale factors at the surface and bottom of the AC surface layer, respectively. R_1 is the surface reflection coefficient, while R_2 consists of the reflection coefficient at the layer interface and the transmission coefficient at the surface. Once R_1 and Δt are known, the thickness and density of the AC layer can be calculated using equations (2-10) and (2-13), respectively. To this end, a column vector $\vec{z}$ was constructed containing all the three unknowns, R_1, R_2 and Δt:

$$\vec{z} = (R_1, R_2, \Delta t)^T, \tag{7-2}$$

where “T” represents “transpose.” Now the problem is to minimize the residue cost:

$$\vec{z} = \underset{z}{argmin}\{C(z)\}, \tag{7-3}$$

where $C(\vec{z})$ is the residue cost function:

$$C(\vec{z}) = \|R_1x(t) + R_2x(t-\Delta t) - y(t)\|^2. \tag{7-4}$$

This is a nonlinear convex optimization problem, which cannot be solved using linear techniques such as regularization. Instead, gradient descent is used to solve equation (7-3) iteratively:

$$\vec{z}^{(n+1)} = \vec{z}^{(n)} - \gamma \nabla_{\vec{z}} C(\vec{z}), \tag{7-5}$$

where γ is the step size, and $\nabla_{\vec{z}} C(\vec{z})$ is the Laplacian of $C(\vec{z})$ with respect of $\vec{z}$.

7.3 Simulation Study

The open source FDTD program GPRMax was used in this study to model the thin AC overlay. A 2-D FDTD model was applied instead of a 3-D model, because pavement structures only vary in the vertical direction. A typical thin AC overlay FDTD model is shown in Figure 7-1. The dielectric constants of the AC overlay and existing old AC pavement are assumed to be 7 and 4, respectively. In practice, the dielectric constant values typically range from 4 to 8. Both layers are assumed to be non-conductive and non-magnetic. It is also possible in practice that the dielectric constant of the old AC pavement is greater than the AC overlay, such as in the case when the old pavement is concrete. The GPR system is placed at 0.5 m above the ground to simulate an air-coupled antenna. The transmitter (Tx) and receiver (Rx) are placed 50 mm away from each other, and may be considered monostatic. A perfect matched layer (PML) boundary is used to absorb the EM wave and to minimize reflection from the boundary. The computation area is spatially discretized into 2.5 mm by 2.5 mm squares, and the time step was determined automatically by the program following equation (3-11). The excitation source used to simulate real GPR pulses is the Ricker wavelet with a center frequency of 2 GHz.

AC overlays with thicknesses of 10 mm, 15 mm, 20 mm, 25 mm, 30 mm, 35 mm, and 40 mm are modeled.

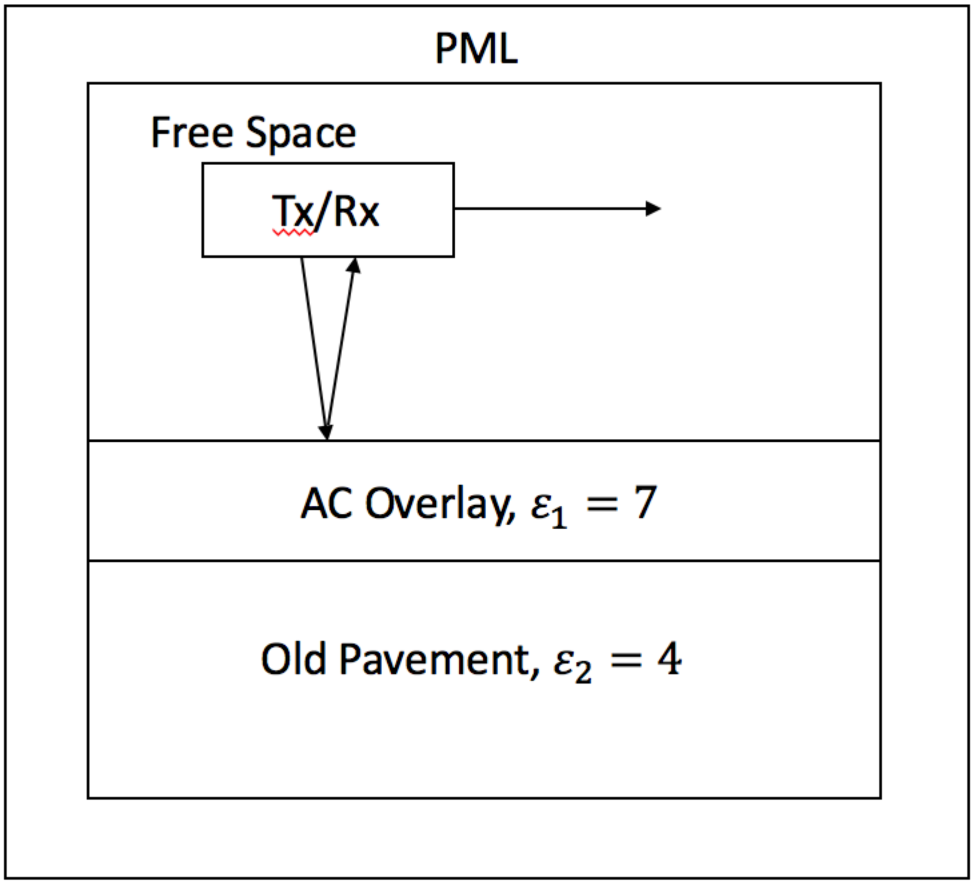

Figure 7-1 FDTD model of AC overlay

An example of an FDTD result is shown in Figure 7-2, where the AC overlay thickness is 15 mm. Figure 7-2(a) shows the AC overlay FDTD model geometry in terms of the dielectric constant of each layer. Figure 7-2(b) shows the pavement reflection radargram. Figure 7-3(c) shows the pavement reflection radargram after coupling pulse removal, and Figure 7-4(d) shows the reflection radargram from a perfect electric conductor (PEC) such as a copper plate.

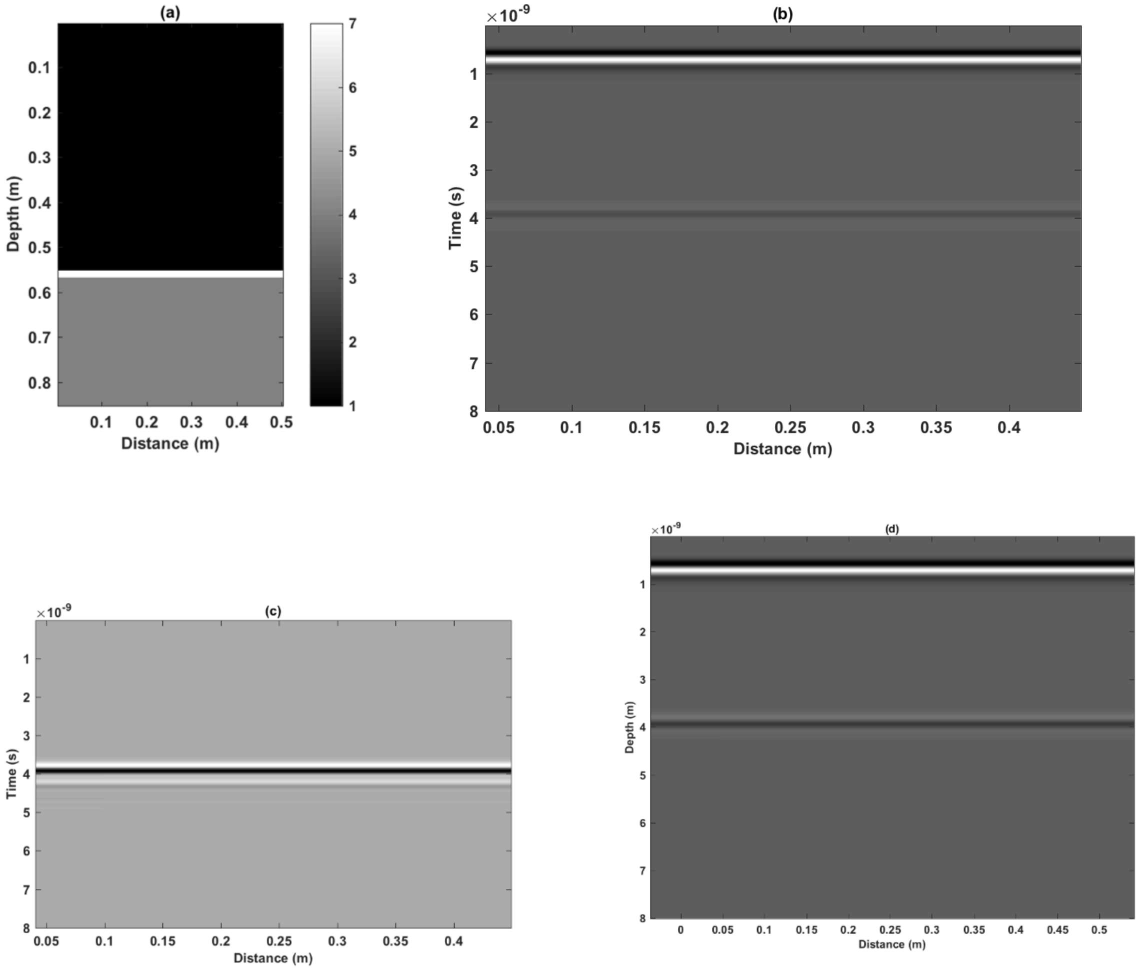

Figure 7-2 FDTD Model of AC (a) model geometry in terms of dielectric constant, (b) radargram of pavement reflection, (c) radargram after coupling pulse removal, and (d) radargram of reflection from PEC

We then averaged the radargram shown in Figure 7-2(c) to a single A-scan for further processing. In each thickness, Gaussian white noises are added to the averaged A-scans, and the signal to noise ratios (SNR) range from 5dB to 30dB, plus the clean signal. The dashed line in Figure 7-3 shows the noisy A-scan from a 1.5 cm thick AC overlay, with an SNR of 15. The solid line in Figure 7-3 shows the A-scan of reflection from a copper plate. We can see that from the noisy A-scan, the second pulse overlaps with the surface reflection; based on what we have seen from previous studies (Zhao and Al-Qadi 2017b), the regularization method cannot be used in this case since the layer thickness is below 30 mm. The nonlinear gradient descent method shown in equation (7-3) was then applied to the noisy A-scan. Based on the obtained R_1, R_2, and Δt, a signal is reconstructed using equation (7-1) and is shown in Figure 7-3 as the dash-dotted line. It can be seen that the reconstructed signal perfectly matches the original noisy pavement reflection.

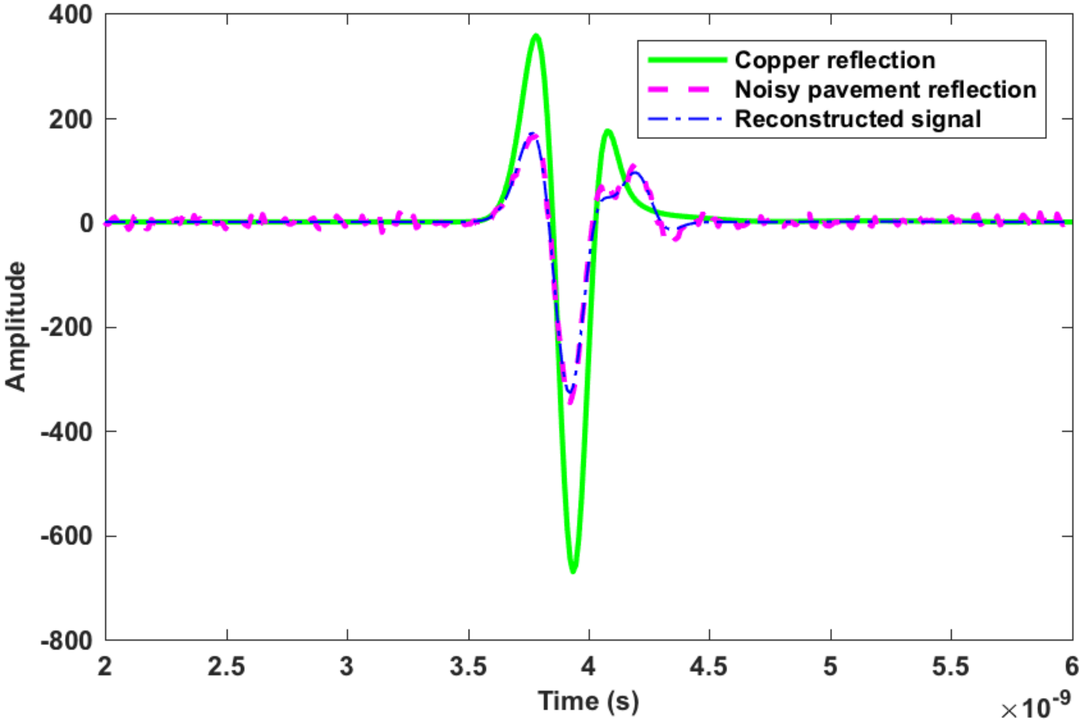

Figure 7-3 A-scan of a copper reflection, noisy pavement reflection, and A-scan reconstructed from a nonlinear gradient descent result

After the surface reflection coefficient and TWTT are obtained, the dielectric constant and the thickness of the AC overlay can be calculated using equations (2-12) and (2-10), respectively. Table 7-1 depicts the dielectric constant results from all thickness and noise levels. The true dielectric constant, according to the FDTD model, is 7. Table 7-1 shows that all the dielectric constant values calculated using nonlinear gradient descent are between 7 and 8, and the accuracy is greatly improved when compared to the dielectric constant calculated using the overlapped signal. We observed that signals with higher SNR generally resulted in a more accurate dielectric constant, and clean signals generally have the best accuracy. Moreover, thicker AC overlay generally have better accuracy, especially at low SNR.

Table 7-1 Results of AC overlay dielectric constant (true dielectric constant = 7)

Algorithm	Thickness (mm)/ SNR level (dB)	10	15	20	25	30	35	40
Nonlinear gradient descent	5	8.00	8.00	8.00	7.44	7.55	7.48	7.53
	10	8.00	8.00	7.62	7.29	7.53	7.50	7.52
	15	8.00	7.83	7.56	7.35	7.28	7.46	7.40
	20	8.00	7.81	7.44	7.39	7.19	7.29	7.37
	25	8.00	7.87	7.41	7.38	7.31	7.36	7.31
	30	8.00	7.76	7.39	7.30	7.27	7.31	7.29
	Clean	8.00	7.78	7.39	7.30	7.29	7.30	7.30
Surface Reflection Method	Clean	11.61	9.40	9.23	11.44	10.40	10.46	9.18

The thickness results are shown in Table 7-2. For each layer thickness, the accuracy increases as the SNR value increases, and the clean signals generally have the best accuracy. The average thickness estimation error at each thickness ranges from 0.6 mm to 0.4 mm. This indicates that the thickness estimation using nonlinear gradient descent is accurate for thin AC overlay, and it is robust to noise.

Table 7-2 Results of predicted thicknesses of AC Overlay in mm

AC Overlay Thickness (mm)	10	15	20	25	30	35	40
SNR=5	9.8	14.7	18.5	24	28.8	34.3	39.4
SNR=10	9.5	14.6	19.2	24.3	29.2	34.3	39
SNR=15	9.5	14.6	19.3	24.5	29.9	34.5	39.5
SNR=20	9.3	14.5	19.5	24.4	29.9	34.7	39.5
SNR=25	9.2	14.5	19.5	24.4	29.7	34.7	39.8
SNR=30	9.3	14.6	19.5	24.6	29.7	34.8	39.9
Clean	9.3	14.6	19.5	24.6	29.7	34.8	39.9
Average	9.4	14.6	19.3	24.4	29.6	34.6	39.6
Absolute Error	0.6	0.4	0.7	0.6	0.4	0.4	0.4

7.4 Field Validation

7.4.1 Description of the test site

As shown in Figure 7-4, a field study was conducted on U.S. Route 45 near Urbana, IL in August 2017 (Zhao et al. 2018). The existing AC pavement was first milled off to 64 mm, and two layers of new AC were placed on top of the existing AC pavement, including a 25 mm leveling binder, and a 38 mm wearing surface. The GPR tests were conducted after the leveling binder was placed and compacted in the southbound passing lane. Only leveling binder was tested in this study because the leveling binder thickness serves the purpose of this study. The mix design information of the leveling binder is shown in Table 7-3. The effective specific gravity (G_{se}) of the aggregate was calculated using the following equation:

$$G_{se} = \frac{100 - P_b}{100/G_{mm} - P_b/G_b}, \tag{7-6}$$

where $G_b = 1.03$ is the specific gravity of the asphalt binder, P_b is the binder percent, and G_{mm} is the maximum specific gravity of asphalt mixture.

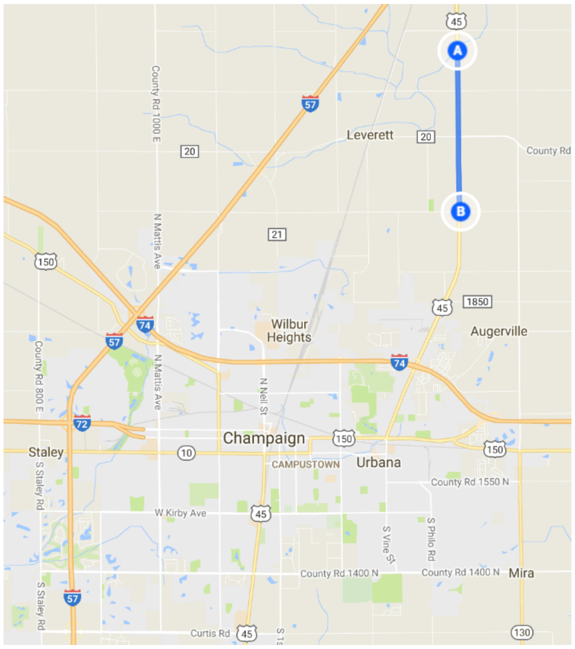

Figure 7-4 Location of the construction site, Champaign, IL

Table 7-3 Asphalt mixture design information of the leveling binder

	Nominal Maximum aggregate size (mm)	Gradation	Binder type	Binder content (%)	G_{mm}	G_{sb}	G_{se}
Leveling Binder	9.5	Fine-graded	PG 64-28	6.4	2.483	2.658	2.748

We used the GPR system manufactured by GSSI in the study, as shown in Figure 7-5. Both 2 GHz and 1 GHz antennas were used, but only the signal from the 2 GHz antenna was analyzed since it has a higher resolution than the 1 GHz antenna and the required EM penetration is a little more than 25 mm.

Figure 7-5 GPR static data collection on US Route 45 after leveling binder was placed

7.4.2 Results

A GPR survey was conducted at 14 static locations, and cores were taken from the same locations where the GPR data were collected, as shown in Figure 7-6. The thickness and density of the cores were measured at the laboratory. With continuous measurement, GPR can be used to generate the thickness and density profile along the roadway, as shown in a study conducted in

Macomb, IL (Wang et al. 2018). However, in this test, only static GPR data were collected and validated because of higher thickness and density prediction accuracy.

Figure 7-6 Core extraction at the location of GPR measurement (left), and cores taken (right)

Figure 7-7 shows one static pavement reflection from core 3-4. The next step is to average the 2-D radargram along the x-axis to get the A-scan as the solid line shown in Figure 7-8. The dashed line in Figure 7-8 shows the signal reflected from a copper plate.

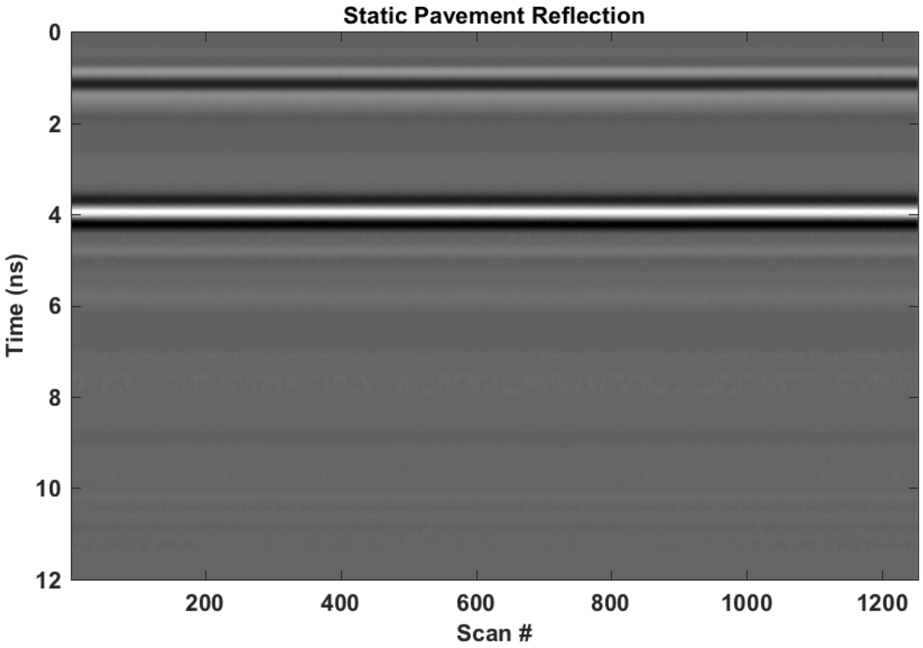

Figure 7-7 GPR radargram reflected from core location 3-4

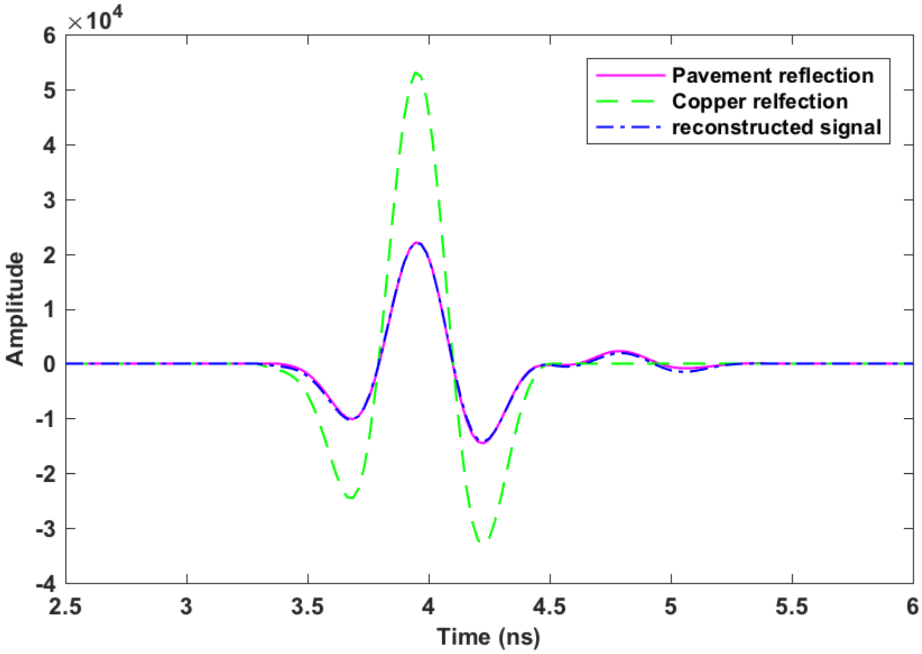

Figure 7-8 A-scan of copper reflection, pavement reflection, and A-scan reconstructed from nonlinear gradient descent result from core location 3-4

Based on the cores taken, the old AC pavement after milling has a top layer with a thickness of around 25 mm. As a result, three GPR pulses reflected from the surface of the new overlay, the interface between the new overlay and the old pavement, and the bottom of the top layer of the old pavement, are overlapped with each other. Since equation (7-4) only concerns a two-layered system, it needs to be modified to accommodate the case with a three-layered system. The new cost function is:

$$C(\vec{z}) = \|R_1 x(t) + R_2 x(t - \Delta t_1) + R_3 x(t - \Delta t_2) - y(t)\|^2, \tag{7-7}$$

where R_3 is the reflection scaling factor at the bottom of the top layer of the old pavement, and Δt_2 is the TWTT of the EM wave within the top two layers. Now the unknown vector becomes $\vec{z} = (R_1, R_2, R_3, \Delta t_1, \Delta t_2)^T$. Using equation (7-7) as the cost function in equation (7-3), and solving it using the same gradient descent method shown in equation (7-5), the surface reflection coefficient R_1 and the TWTT of EM wave within the new overlay Δt_1 can be obtained. In Figure 7-8, the dashed line shows the signal reconstructed from the solution z. It can be noted that the reconstructed result matches the original reflection from the pavement.

In actual practice, the noises contained in the GPR signals are not necessarily white noise, as was the case in the simulation study. Other types of noise include environmental inhomogeneity, internal electrical noises, ringing, etc. When using the nonlinear descent shown in equation (7-3), the solution may converge to an undesired local minimum. To this end, a confined nonlinear gradient descent approach, interior point technique (Byrd et al. 2000), was used in this study on real GPR signals. For each variable in $\vec{z} = (R_1, R_2, R_3, \Delta t_1, \Delta t_2)^T$, a lower bound and an upper bound were manually set. The bounds are determined based on prior knowledge of the range of the parameter. For example, the surface reflection coefficient should be in the range of $R_1 \in [1/3, 1/2]$, since the dielectric constant of the AC overlay is in the range of 4 to 9.

The gradient decent algorithm did not converge in the case of core location 4-5. The reason could be because the dielectric constant values between adjacent layers are close and the EM wave barely reflects at the interface; or because of the low SNR value of the GPR signal.

Table 7-4 shows the results of thickness estimation from the remaining 13 coring locations after the nonlinear gradient descent was applied. The ground truth thickness and estimation error are also included. It can be seen that except for core locations 4-4 and 5-5, all other estimated thickness errors are within 5 mm. The average core thickness is 24 mm, and the average estimated thickness is 27 mm. The error is only 3 mm, which indicates a good performance of the proposed nonlinear gradient descent algorithm.

Table 7-4 Thickness estimation results and errors for 13 core locations

Core #	3-2	3-3	3-4	3-5	4-1	4-2	4-3	4-4	5-1	5-2	5-3	5-4	5-5	Ave
Predicted Thickness (mm)	24	22	30	27	25	27	27	27	30	26	26	29	34	27
True thickness (mm)	20	25	27	25	24	24	23	21	27	25	24	25	25	24
Error (mm)	4	-3	3	2	1	3	4	6	3	1	2	4	9	3

Table 7-5 shows the dielectric constant estimated using the obtained surface reflection coefficient R_1, as well as the one using raw surface reflection amplitude. The dielectric constant before and after the nonlinear gradient descent algorithm are all around 6 and the differences are small. This could be because the surface reflection amplitude is not affected significantly by the reflection from the bottom of the overlay. Before the placing of leveling binder, longitudinal GPR tests were conducted, and it was found that the average dielectric constant of the top layer of the old pavement is mostly from 5.9 to 6.2; therefore, the difference between the dielectric constant of the surface layer and the top layer of the old pavement is small according to Table 7-5. As a result, the reflection from the interface of the leveling binder and the old pavement is small.

Table 7-5 Dielectric constant results using nonlinear gradient descent method and raw surface amplitude

Core #	3-2	3-3	3-4	3-5	4-1	4-2	4-3
Raw Surface Amplitude	5.9037	6.4721	5.8814	5.9647	5.7658	6.1328	5.7400
Nonlinear	5.4904	5.8619	5.8968	6.0863	6.1071	6.2050	5.8291
Core #	4-4	5-1	5-2	5-3	5-4	5-5	
Raw Surface Amplitude	5.8487	5.6069	5.7301	5.7831	6.0204	5.9968	
Nonlinear	5.9826	5.6778	5.7946	5.6059	6.0104	6.0666	

The densities of each core measured in the laboratory are shown in Table 7-6. Using the G_{mb} of core # 5-5, the back-calculated G_{se} value was 8.05. The G_{mb} of the other 12 cores were calculated using equation (2-13), and the results are shown in Table 7-6 for both nonlinear and raw surface amplitude methods. The errors compared to ground truth were calculated; the average values of G_{mb} and estimation error were also calculated. First of all, the estimated G_{mb} values using the nonlinear gradient descent algorithm are close to the true G_{mb}, and the maximum relative error is 5.39% for core # 4-1. The average G_{mb} estimation error, whether the nonlinear gradient descent algorithm was used, stays almost the same (1.81% vs. 2.08%). The reason is, again, that the reflection at the interface of the leveling binder and the old asphalt is small, and therefore has a small effect on the surface reflection amplitude. However, in cases where the dielectric constant of the overlay and old pavement have a large difference, the estimated G_{mb} using raw surface reflection amplitude could be inaccurate.

Table 7-6 G_{mb} estimation results using nonlinear gradient descent method and raw surface amplitude

Core #	3-3	3-3	3-4	3-5	4-1	4-2	4-3	4-4	5-1	5-2	5-3	5-4	5-5	Ave
True G_{mb}	2.2099	2.2322	2.2397	2.1850	2.1801	2.2744	2.2421	2.2968	2.2645	2.2347	2.2620	2.2297	2.2893	-
Nonlinear	2.1771	2.2479	2.2549	2.2932	2.2975	2.3179	2.2414	2.2721	2.2121	2.2347	2.1985	2.2777	2.2892	-
Error	1.48%	0.70%	0.68%	4.95%	5.39%	1.91%	0.03%	1.07%	2.31%	0.00%	2.81%	2.15%	0.01%	1.81%
Raw Surface Amplitude	2.2562	2.3746	2.2518	2.2685	2.2290	2.3028	2.2240	2.2453	2.1987	2.2221	2.2324	2.2798	2.2750	-
Error	2.10%	6.38%	0.54%	3.82%	2.25%	1.25%	0.81%	2.24%	2.91%	0.56%	1.31%	2.24%	0.63%	2.08%

7.5 Summary

In this study, a gradient descent based nonlinear optimization method was developed to increase the resolution of GPR signals reflected from thin AC overlay. It can be used to find both the TWTT and the surface reflection coefficient of the GPR reflection.

First a simulation study was conducted. GPR signals reflected from AC overlays of thickness ranging from 10 to 40 mm are modeled using FDTD simulation and noises were added. The nonlinear gradient descent algorithm was then applied to the overlapped GPR signals to recover the surface reflection amplitude and the EM wave TWTT within the overlay. The accuracy of dielectric constant values greatly improved after the nonlinear gradient descent method was applied. The errors of thickness estimation for all layer thicknesses and noise levels were all below 1 mm.

A field GPR survey was then conducted on newly built AC overlay with a design thickness of 25 mm. GPR signals were collected on 14 static coring locations. The nonlinear gradient descent algorithm was then applied on the overlapped GPR signals to find the surface reflection amplitude and the TWTT. The density of one core was used to back-calculate the G_{se} of aggregate. The thickness and G_{mb} of the AC were then calculated. The average thickness and G_{mb} estimation errors are 3 mm and 1.81%, respectively.

This study shows that the nonlinear gradient descent method is an effective algorithm for addressing the insufficient GPR resolution. It can be used on GPR signals reflected from thin AC overlays to estimate their thickness and density accurately. Compared to other super-resolution methods such as regularization, the nonlinear gradient descent method could be used on AC overlay less than 25 mm thick and can also be used to find the density of the AC overlay.

The nonlinear gradient descent requires prior knowledge of the pavement structure, since an upper and lower bounds are needed for the gradient decent to converge. Future studies should consider developing algorithms when the prior knowledge of the AC pavement structures is not known.

CHAPTER 8: DEVELOPMENT OF ALGORITHM FOR REAL-TIME THIN AC OVERLAY COMPACTION MONITORING

8.1 Background and Objective

GPR has been used for real-time estimation of the AC pavement density during compaction (Shangguan et al. 2016). For compaction monitoring of thin AC overlay, it is difficult to estimate the density accurately due to the limitation of GPR signal resolution. Meanwhile, the effect of surface moisture on the GPR signal affects the accuracy of density prediction. In this chapter, the nonlinear gradient descent approach developed in Chapter 7 was used to recover the pavement surface reflection. A “modified reference scan” approach was developed to remove the effect of surface moisture on GPR signals during density monitoring.

In Section 8.2, the “reference scan” approach is introduced. In Section 8.3, an algorithm is proposed for thin AC overlay compaction monitoring. A field validation study was conducted and discussed in Section 8.4. Section 8.5 is the summary of this chapter.

8.2 “Reference Scan” Approach

During AC pavement construction, the roller sprays water using nozzles to prevent the asphalt mixture from sticking to the drum. Since water has a larger dielectric constant than pavement, it affects the surface reflection amplitude of the GPR signals. This will cause inaccurate determination of the dielectric constant according to equation (2-12). Previous studies (Shangguan et al. 2013; Shangguan and Al-Qadi 2015; Shangguan et al. 2016) have demonstrated that while the effect of surface moisture in time domain signal is complicated, in the frequency domain, the presence of surface moisture primarily increases the high frequency part of the signal, while the low-frequency part of the signal remains unchanged. This “frequency selection” phenomenon also has a physical explanation: the high frequency part of the signal, which has shorter wavelength, is more attenuated by the lossy surface moisture since the thickness of the surface moisture layer is thin.

Based on this observation, a “reference scan” approach was developed by the authors to eliminate the effect of surface moisture from the surface reflection; then, the AC pavement density can be predicted accurately. The following procedure outlines the “reference scan” approach:

- Collect reference scan from a test pad with no moisture, $y_{dry}(t)$ and take its Fourier transform $Y_{dry}(f)$.
- Collect GPR signal reflected from AC pavement during compaction with surface moisture, $y_{wet}(t)$, and take its Fourier transform $Y_{wet}(f)$.
- Calculate the corrected frequency spectrum: $Y_{wet\_corrected}(f) = Y_{dry}(f) * |Y_{wet}(f_0)| / |Y_{dry}(f_0)|$, where f_0 is the representing low frequency. Shangguan et al. (2016) found that $f_0 = 1.1GHz$ gives the best results.
- Take inverse Fourier transform of the corrected spectrum to get the time domain signal $y_{wet\_corrected}(t)$.
- Use $y_{wet\_corrected}(t)$ as the pavement reflection to calculate the AC pavement dielectric constant and density.

Figure 8-1 illustrates an example of the “reference scan” approach based on field GPR data reflected from a wet AC pavement surface. The detail will be provided in section 8.4. The frequency plot reveals that after the correction, the high frequency part of the signal decreased. Figure 8-1(b) shows that the presence of surface moisture not only scales the GPR signal, but also changes the phase of signal in the time domain.

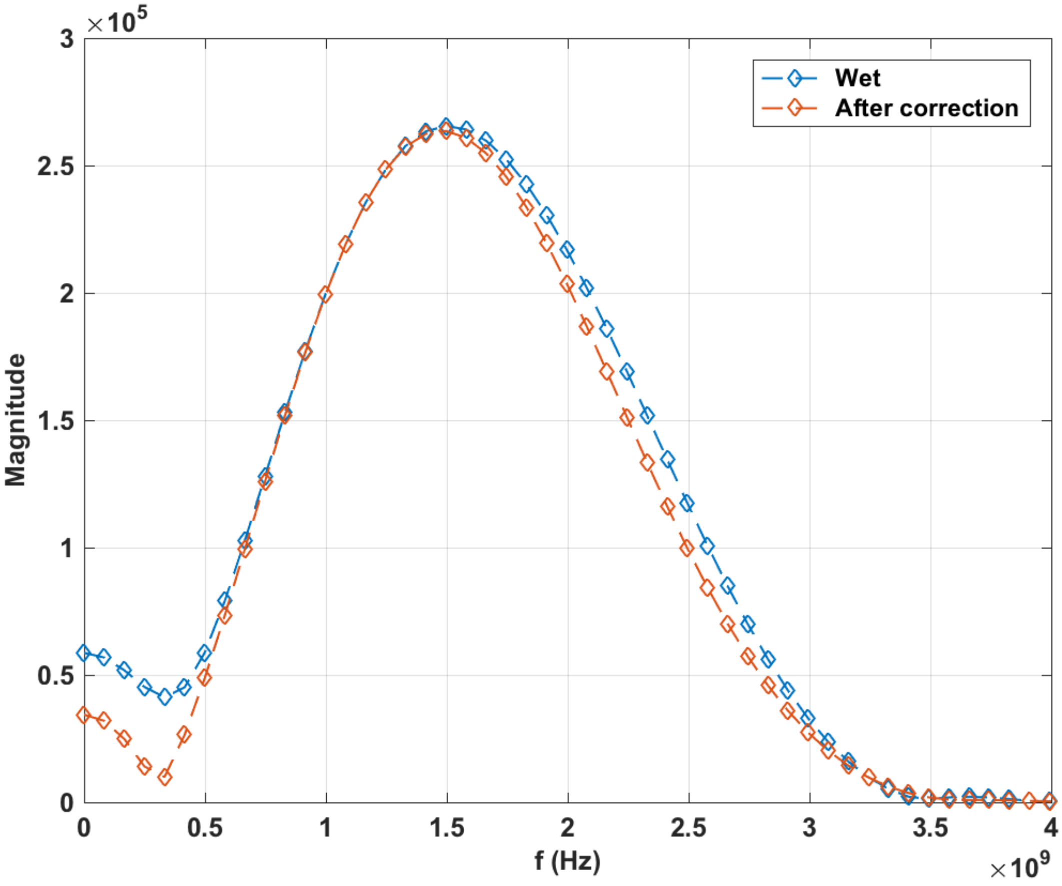

(a)

Figure 8-1 GPR wet scan before and after correction using "reference scan" approach in (a) frequency domain, and (b) time domain

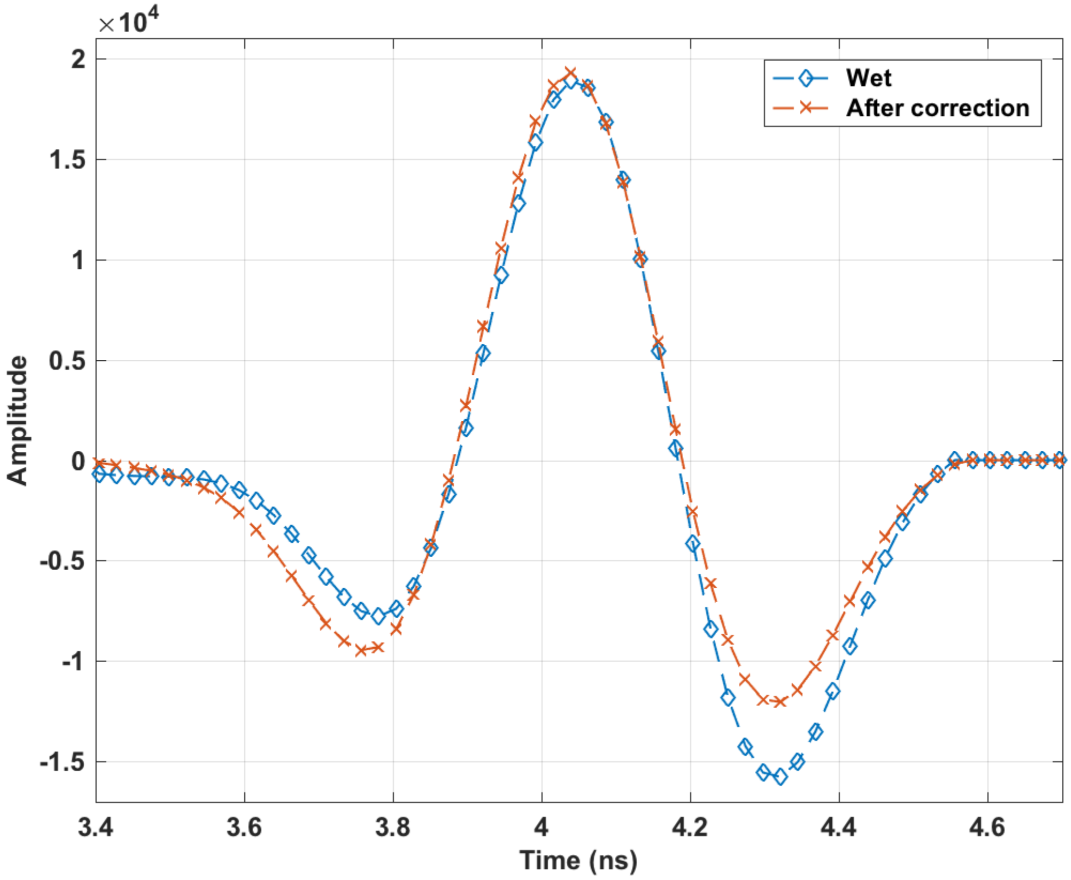

(b)
Figure 8-1 (cont.)

8.3 Thin AC Overlay Compaction Monitoring

8.3.1 Reconstruction of thin AC overlay surface reflection during compaction

In Chapter 7, a nonlinear gradient descent optimization was proposed to recover the reflection coefficient and TWTT from overlapped GPR pulses as indicated by equation (7-3). This method is based on the assumption of the linearity of pavement reflection system. However, according to Shangguan et al. (2016), when the surface moisture exists, the surface reflection is not simply the incident signal scaled by a factor, $R_1x(t)$; instead, the scaling only occurs at the higher range of the frequency spectrum, but not at the lower frequency range. This can be represented by the following equation:

$$y(t) = y_1(t) + R_2 x(t - \Delta t), \tag{8-1}$$

where $y_1(t)$ is the reflection from the wet surface.

To obtain the correct surface reflection, first equation (7-1) is still used to calculate R_2 and Δt. For AC pavement with surface moisture, the model (7-1) may have larger errors, since the reflection from the surface with moisture and the reflection from copper plate have different waveform, according to previous studies (Shangguan et al. (2016)). However, the estimation of the location and the scale factor of the reflection at the bottom of the AC overlay is not affected. Therefore, in this study, this linear model is used to solve R_2 and Δt, and then the surface reflection $y_1(t)$ can be reconstructed by subtracting the reflection from the bottom of the thin AC overlay: $y_1(t) = y(t) - R_2 x(t - \Delta t)$. The surface moisture correction algorithm in Section 8.2 can then be used to find the correct surface reflection amplitude.

8.3.2 Modified surface moisture correction algorithm

In Section 8.2, the “reference scan” approach was introduced to remove the effect of surface moisture on AC during construction. In this section, a “modified reference scan” approach was proposed to simplify the computation, and also to improve the stability and accuracy of the “reference scan” method.

The “reference scan” approach corrects the “wet scan” using a reference scan collected from dry pavement:

$$Y_{wet\_corrected}(f) = Y_{dry}(f) * \frac{|Y_{wet}(f_0)|}{|Y_{dry}(f_0)|}, \tag{8-2}$$

where $f_0 = 1.1GHz$ was found to be the cut-off frequency between changed and unchanged frequencies for 2GHz antenna signal. The corrected time domain signal is then obtained by inverse Fourier Transform:

$$\begin{aligned} y_{wet\_corrected}(t) &= \mathcal{F}^{-1}(Y_{wet\_corrected}(f)) \\ &= \mathcal{F}^{-1}(Y_{dry}(f) * |Y_{wet}(f_0)|/|Y_{dry}(f_0)|) \\ &= y_{dry}(t) * |Y_{wet}(f_0)|/|Y_{dry}(f_0)|. \end{aligned} \tag{8-3}$$

It then follows that $y_{dry}(t)/|Y_{dry}(f_0)|$ is the incident signal normalized at f_0, since the dry pavement reflection has the same waveform as the incident signal. Since the copper reflection is also a scaled incident signal, we can replace $y_{dry}(t)/|Y_{dry}(f_0)|$ with $y_{copper}(t)/|Y_{copper}(f_0)|$ in equation (8-3) to obtain:

$$y_{wet\_corrected}(t) = y_{copper}(t) * \frac{|Y_{wet}(f_0)|}{|Y_{copper}(f_0)|}, \tag{8-4}$$

or

$$\frac{y_{wet_{corrected}}(t)}{y_{copper}(t)} = \frac{|Y_{wet}(f_0)|}{|Y_{copper}(f_0)|}. \tag{8-5}$$

It can then be seen that the surface reflection coefficient A_1/A_p in equation (2-12) can be calculated as:

$$\begin{aligned} A_1/A_p &= y_{wet\_corrected}(t)/y_{copper}(t) \\ &= |Y_{wet}(f_0)|/|Y_{copper}(f_0)|. \end{aligned} \tag{8-6}$$

Equation (8-6) implies that to calculate the surface reflection coefficient without the effect of surface moisture, it's safe to skip the "reference scan" approach discussed in section 8.2, and simply take the ratio of the wet reflection and the copper reflection at frequency f_0 in the frequency domain.

Another drawback of the "reference scan" approach is that the results are highly sensitive to the reference frequency selected, f_0. A lower reference frequency would yield a more accurate expected result; however, signals at a higher reference frequency have higher signal to noise ratio, thus the results are more reliable. As a result, a constant cutoff frequency cannot satisfy both requirements. Therefore, in this study, we calculate the surface reflection coefficient R_1 using the following optimization equation:

$$R_1 = \underset{\alpha}{argmin}\left\{\left\|\left|Y_{wet}(f)\right| - \alpha\left|Y_{copper}(f)\right|\right\|^2, f \in [f_1, f_2]\right\}, \tag{8-7}$$

where f_1 and f_2 are the lower cutoff frequency and higher cutoff frequency, respectively. By using both a lower and higher cutoff frequency, the whole lower frequency parts of the GPR signal were considered, and the output is robust to noises at the same time since the calculated reflection coefficient is an averaged value. According to Shangguan et al. (2016), a 2 GHz antenna GPR signal frequency spectrum below 0.5 GHz has large fluctuations due to quantization error; therefore the lower cutoff frequency is set to $f_1 = 0.5\ GHz$. In general, the lower cutoff frequency can be determined by finding the frequency point below which the the ratio of wet signal and copper plate signal fluctuates. To this end, the following method can be used to determine both a lower and higher cutoff frequency:

- For lower cutoff frequencies $f_1 \in [f_{1lo}, f_{1hi}]$, and higher cutoff frequencies $f_2 \in [f_{2lo}, f_{2hi}]$, where f_{1lo}, f_{1hi} are the possible limits of the lower cutoff frequency, respectively, and f_{2lo}, f_{2hi} are the the possible limits of the higher cutoff frequency, respectively, calculate both the reflection coefficient R_1 using equation (14), and the corresponding mean squared error (MSE) $\left\|\left|Y_{wet}(f)\right| - R_1\left|Y_{copper}(f)\right|\right\|^2$.
- Find the f_1 and f_2, which minimize the MSE. This can be done by first minimizing MSE with respect to f_1, then with respect to f_2. This process can be repeated multiple times to make the estimation of f_1 and f_2 more accurate. Alternatively, the MSE can be minimized using gradient descent to obtain f_1 and f_2 simultaneously.

In the original “reference scan” approach, the cutoff frequency 1.1 GHz was determined on both simulated and real GPR data; while in the “modified reference scan” approach, both the higher and lower cutoff frequencies can be determined systematically using the above procedure. Therefore, the “modified reference scan” approach can be generalized to other GPR antenna frequencies.

Figure 8-2 shows an example of the above procedure based on a GPR scan collected from thin leveling binder after a final roller pass in a field test. The project details will be discussed in the next section. In Figure 8-2(a), the MSE is plotted versus different lower cutoff frequency, while the higher frequency is fixed at 1.1 GHz. It can be seen from Figure 8-2(a) that starting around 0.5 GHz, the MSE reaches the minimum value. This suggests that the lower cutoff frequency should be around 0.5 GHz, which agrees with the conclusion in Shangguan et al. (2016). In Figure 8-2(b), the MSE is plotted at a different higher cutoff frequency, while the lower cutoff frequency is fixed at 0.5 GHz. The MSE is minimized at around 1.05 GHz, which is close to the cutoff frequency found based on experiment data by Shangguan et al. (2016). Since the “modified reference scan” approach uses a series of fitting frequency points, a small difference of the lower and higher cutoff frequencies will not affect the R_1 fitting result significantly.

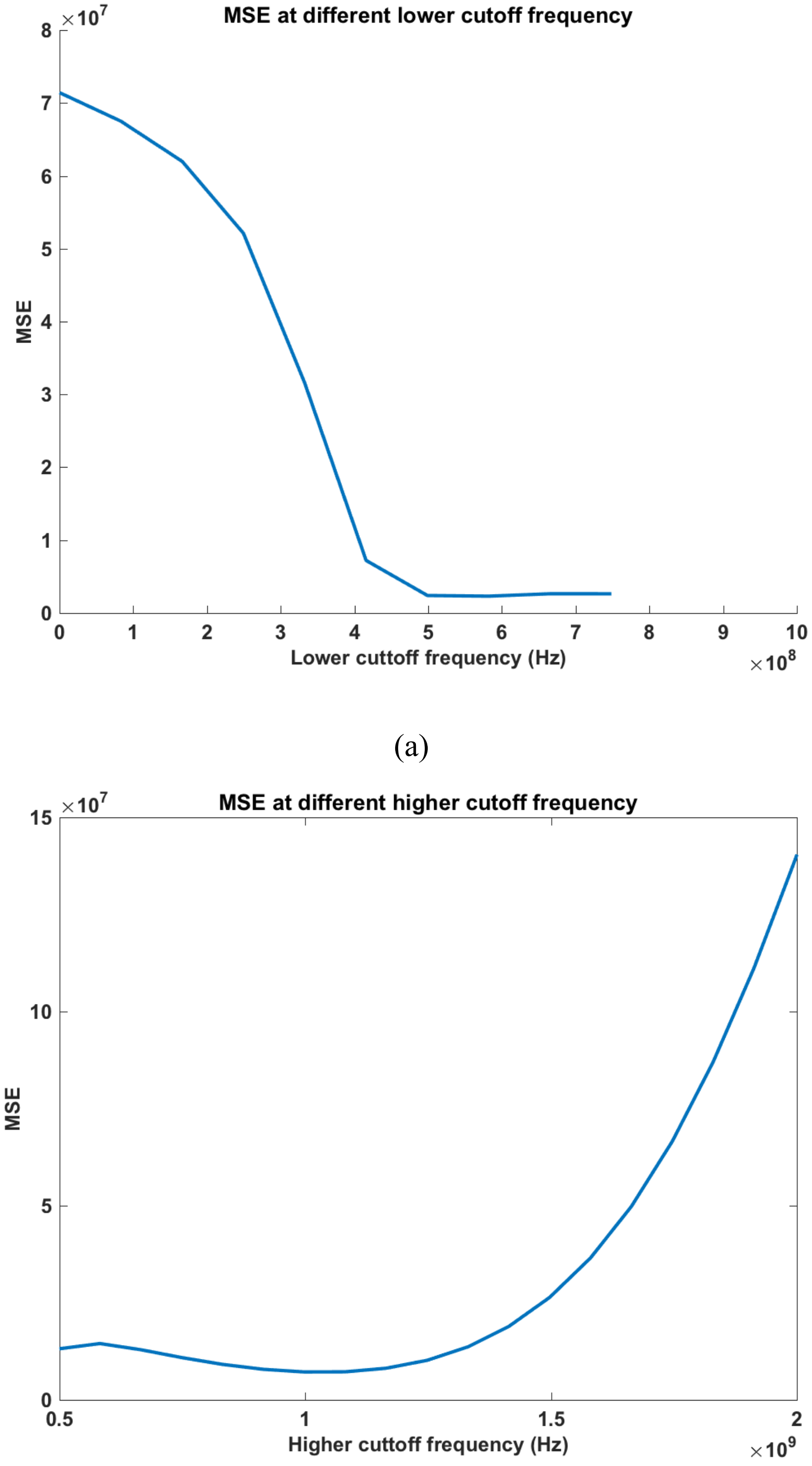

(a)

(b)

Figure 8-2 MSE at a different (a) lower cutoff frequency and (b) higher cutoff frequency

To further validate the "modified reference scan" approach with other frequency antennas, a laboratory experiment was conducted at the Illinois Center for Transportation at the University of Illinois at Urbana-Champaign. Figure 8-3(a) shows the setup of a 1 GHz antenna during the test. Under the antenna, a 1 m by 1 m square area was sprayed with 650 ml. of water as shown in Figure 8-3(b). Before spraying the water, GPR data were collected on the dry AC pavement. After the water was sprayed, GPR data were collected every 2 to 3 min until the pavement was dry to analyze the effect of change of surface moisture water volume on the signal.

(a) (b)

Figure 8-3 Laboratory experiments to analyze the effect of surface moisture on 1 GHz signal: (a) setup of 1 GHz antenna; (b) water sprayed on AC surface

In the time domain, the effect of surface moisture on GPR reflection is complicated. The effect on frequency domain is shown in Figure 8-4. It can be first seen from Figure 8-4 that compared to the dry reflection spectrum, the wet reflection spectra increase in the higher frequency part (higher than 0.7 GHz), and in the lower frequency part they remained unchanged because of the frequency selective phenomenon. Secondly, the dry pavement reflection spectrum is on the lowest level as shown in the dotted line. Finally, the frequency spectrum decreases with time because the surface moisture amount decreases with time.

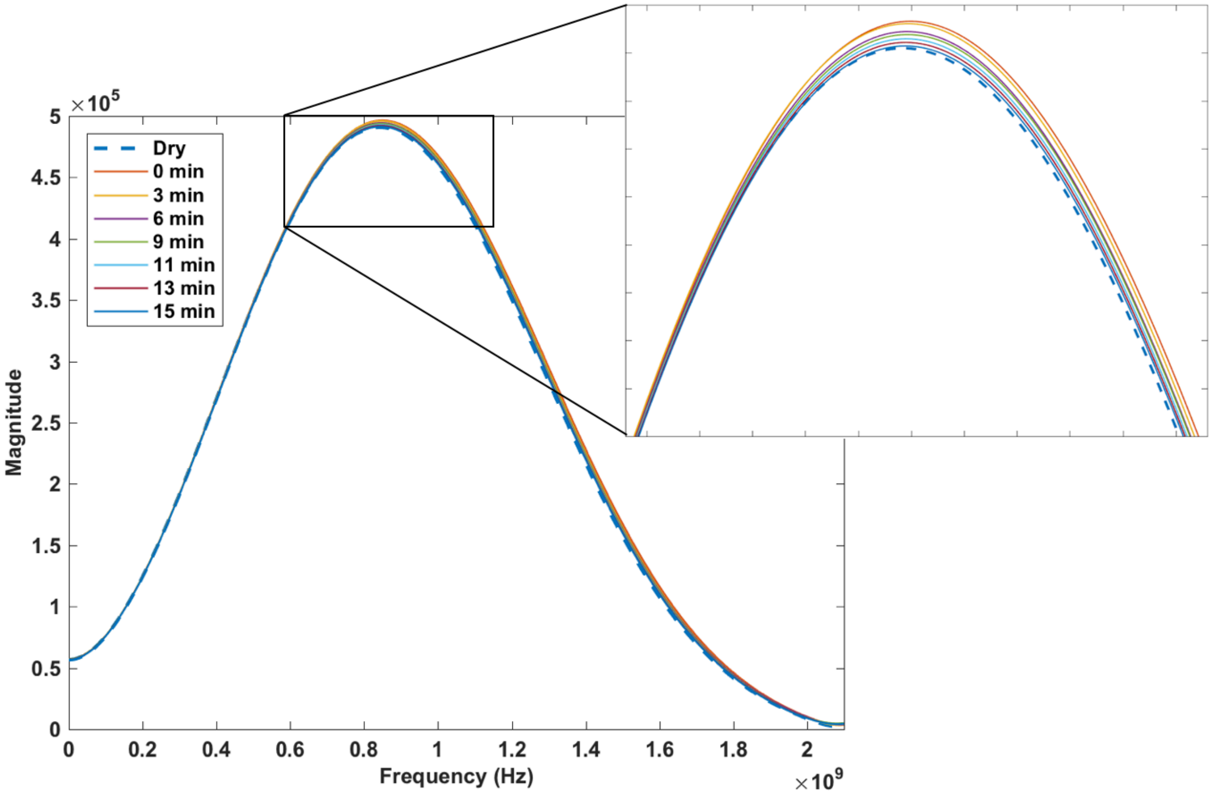

Figure 8-4 Frequency magnitude spectrum of GPR reflection from AC surface with different surface moisture amount

The "modified reference scan" method is then used to calculate the correct reflection coefficient using wet copper reflection. Figure 8-5 shows the MSE corresponding to different lower and higher cutoff frequencies. In Figure 8-5(a), the MSE is plotted versus a different lower cutoff frequency, while the higher frequency is fixed at 0.75 GHz. It can be seen that the MSE reaches the minimum value around 0.42 GHz. This suggests the lower cutoff frequency should be 0.42 GHz, which is similar to the 2 GHz antenna. In Figure 8-5(b), the MSE is plotted at a different higher cutoff frequency, while the lower cutoff frequency is fixed at 0.42 GHz. The MSE is minimized at around 0.75 GHz, which is different from that of 2 GHz antenna. Also it can be seen that with a different surface moisture amount, the lower and higher cutoff frequencies remained unchanged.

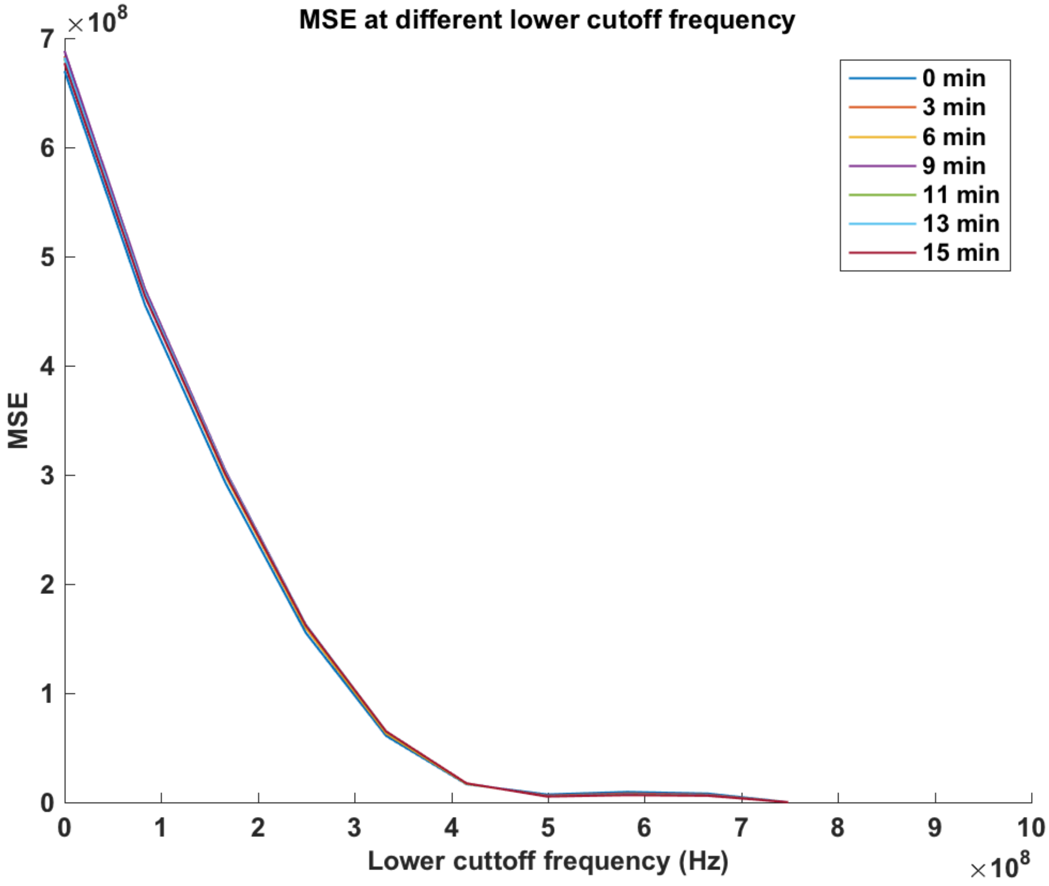

(a)

Figure 8-5 Determining (a) lower and (b) higher cutoff frequency using "modified reference scan" approach on GPR reflection from AC surface with different surface moisture amounts

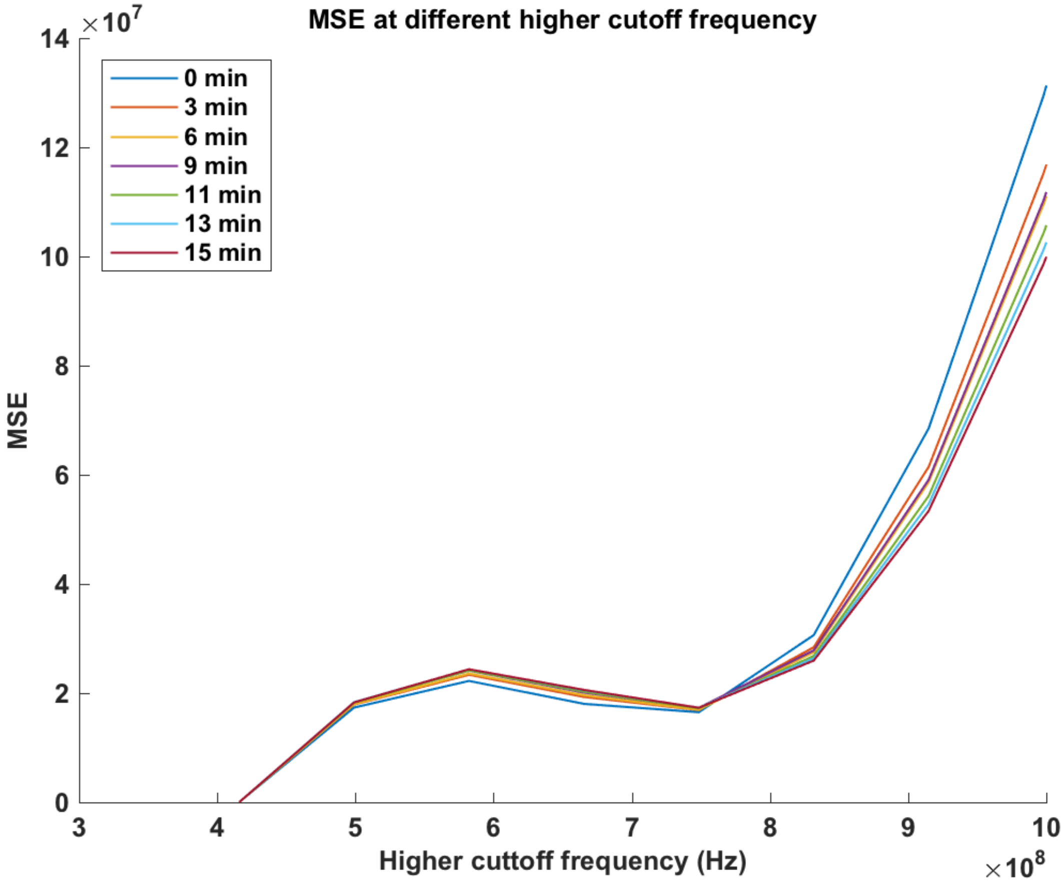

(b)
Figure 8-5 (cont.)

The dielectric constant values calculated with and without the “modified reference scan” approach are shown in Figure 8-6. The dielectric constant calculated using the dry pavement reflection is 5.9631, which is shown as the dotted line in Figure 8-6. If calculated directly using wet surface reflection, the dielectric constant values are significantly greater than the correct value and the maximum error is 3.5% right after the water was sprayed. When the surface moisture decreases with time, the error also decreases as expected. After the “modified reference scan” was applied, the dielectric constant values decreased at all surface moisture amount levels, and the maximum error is 1.1 %. The dielectric constant estimation accuracy increases when the “modified reference scan” approach is applied.

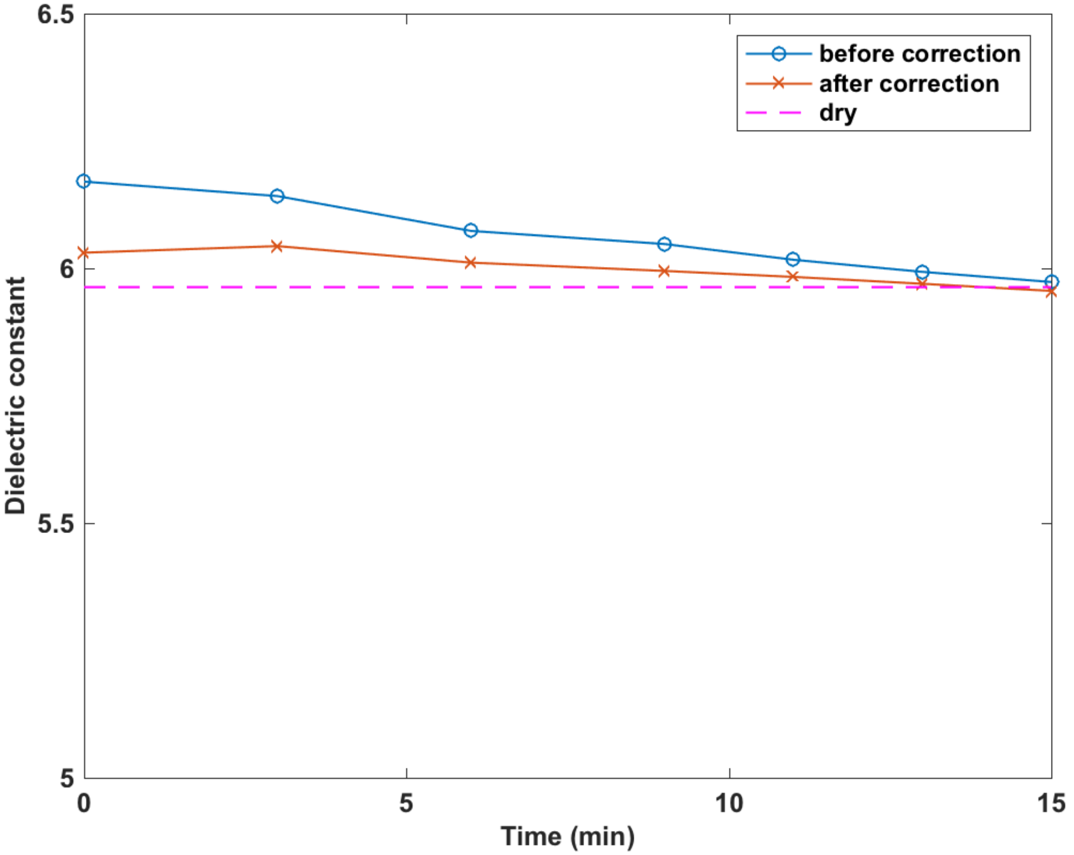

Figure 8-6 Dielectric constant values calculated before and after “modified reference scan” was applied

This experiment shows that for 1 GHz antenna, the frequency-selective property still holds. The “modified reference scan” approach can be used to remove the effect of surface moisture and recover the correct surface reflection, and thus the dielectric constant can be accurately calculated.

In this study, this “modified reference scan” approach will be used for predicting AC pavement density with presence of surface moisture.

8.4 Field Test Validation

8.4.1 Description of the test site

A field study was conducted on Indiana Avenue in Thornton, IL from October to November 2017. The test site location is shown in Figure 8-7. The existing AC pavement was first milled off to 76 mm, and two layers of new AC were placed on top of the existing AC pavement, including a 25 mm leveling binder, and a 50 mm stone matrix asphalt (SMA) surface. GPR tests were conducted after the leveling binder was placed on Oct 29, 2017 and after the SMA surface was placed on Nov 14, 2017. The mix design information of both the leveling binder and the SMA surface are shown in Table 8-1. The G_{se} of the aggregate was calculated using the equation (7-6).

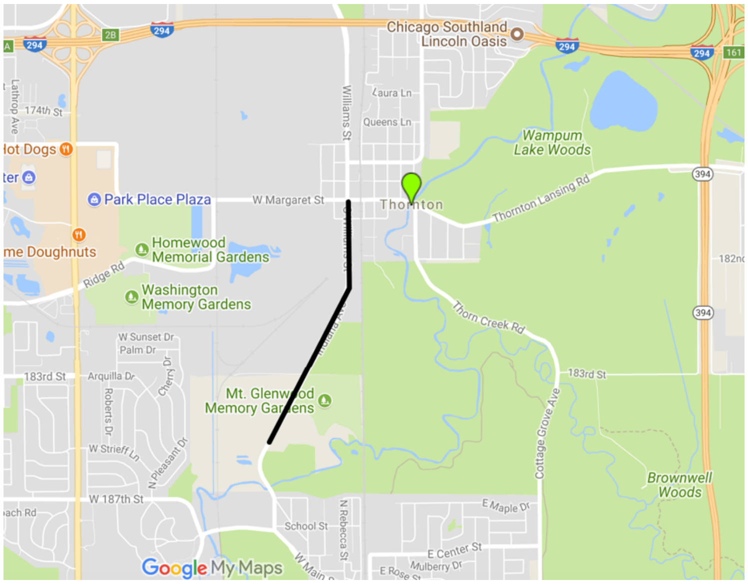

Figure 8-7 Location of the construction site, Thornton, IL

Table 8-1 Asphalt mixture design information of both leveling binder and surface SMA

	Nominal Maximum aggregate size (mm)	Gradation	Binder type	Binder content (%)	G_{mm}	G_{sb}	G_{se}
Leveling Binder	4.76	Dense-graded	PG 70-28	7.9	2.412	2.644	2.725
SMA Surface	12.7	Gap-graded	PG 70-28	6.2	2.565	2.808	2.845

To achieve the purpose of compaction monitoring, a “SAKAI R2H2” model non-vibratory roller was modified to install two GPR antennas at the front, as shown in Figure 8-8 on the left. The GPR unit used in this study is SIR 20, manufactured by Geophysical Survey Systems, Inc.

The GPR control unit was installed inside a security box on the roller together with the GPS receiver as shown in Figure 8-8, on the right. The GPS antenna was put on the hood of the roller as seen in Figure 8-8 on the left. In this study, the signal from the 2 GHz antenna on the driver's side was used.

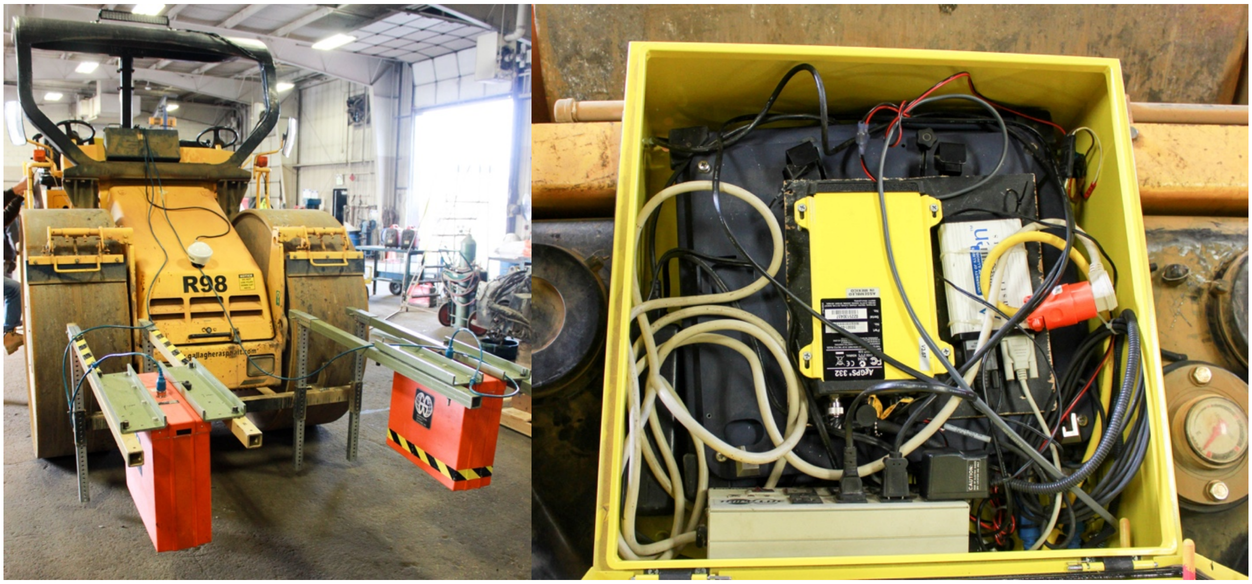

Figure 8-8 Modified SAKAI R2H2 roller (left) and GPR control unit (right) for compaction monitoring

8.4.2 GPR data collection

GPR signals were continuously collected during the compaction of the AC pavement. Figure 8-9 shows the GPR survey during both leveling binder and SMA construction. GPS coordinates were recorded so that the GPR signals can be correlated with the roller's location. The GPR data were processed after the GPR data collection. To validate the GPR density prediction results, nuclear density tests were taken at one location during both leveling binder and SMA surface construction as shown in Figure 8-9. Every time the roller passed the nuclear density spot, the GPR data was marked for later correlation. After the final roller pass, a core was taken at the nuclear spot for validation. GPR data were collected on copper plates in both constructions. For both leveling binder and SMA surface, an additional core was also taken after the construction on dry pavement for calibration of the dielectric constant of the aggregate.

Figure 8-9 AC pavement compaction monitoring using GPR on the leveling binder (left) and the SMA surface (right)

8.4.3 Results and discussions

After the GPR data were collected during compaction, the non-linear optimization and the "modified reference scan" approach were applied on the GPR signals. Figure 8-10 shows an example of the result. The GPR signal was collected after the final roller pass on the leveling binder at the nuclear spot. The copper reflection was scaled using the reflection coefficient calculated using the "modified reference scan" approach as in equation (8-7).

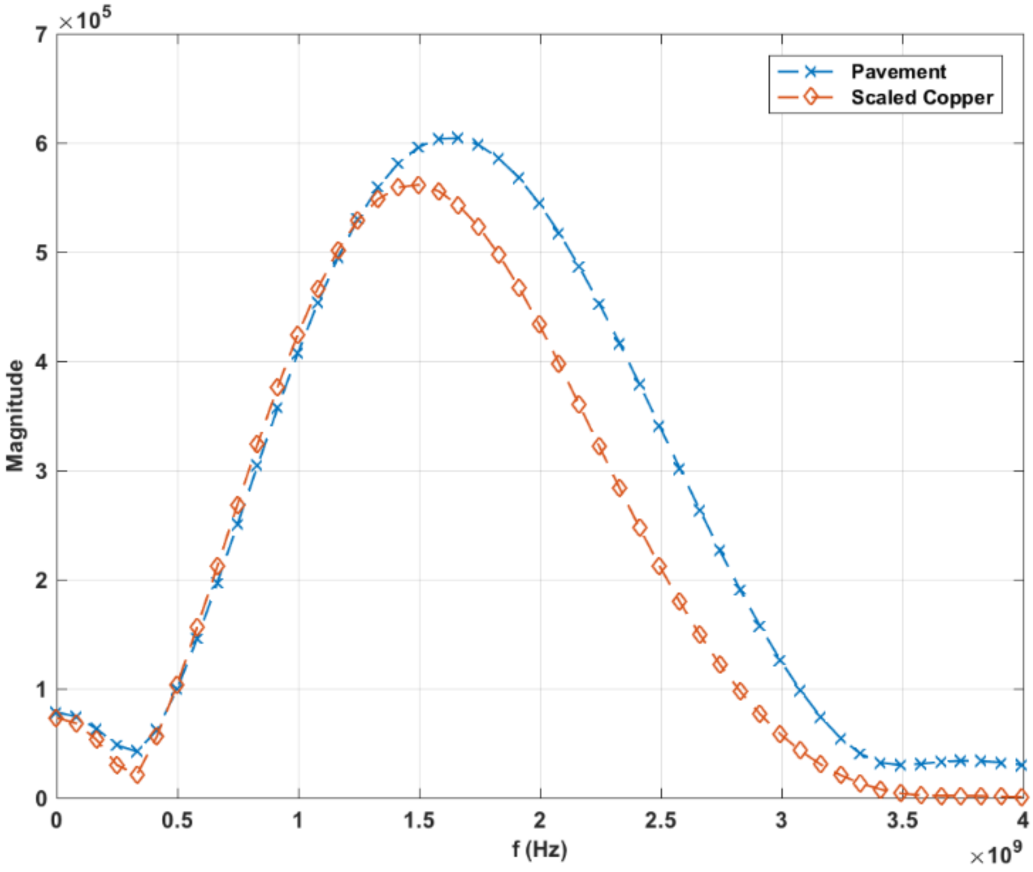

(a)

Figure 8-10 GPR wet scan on leveling binder and scaled copper plate reflection using modified "reference scan" approach in (a) frequency domain and (b) time domain

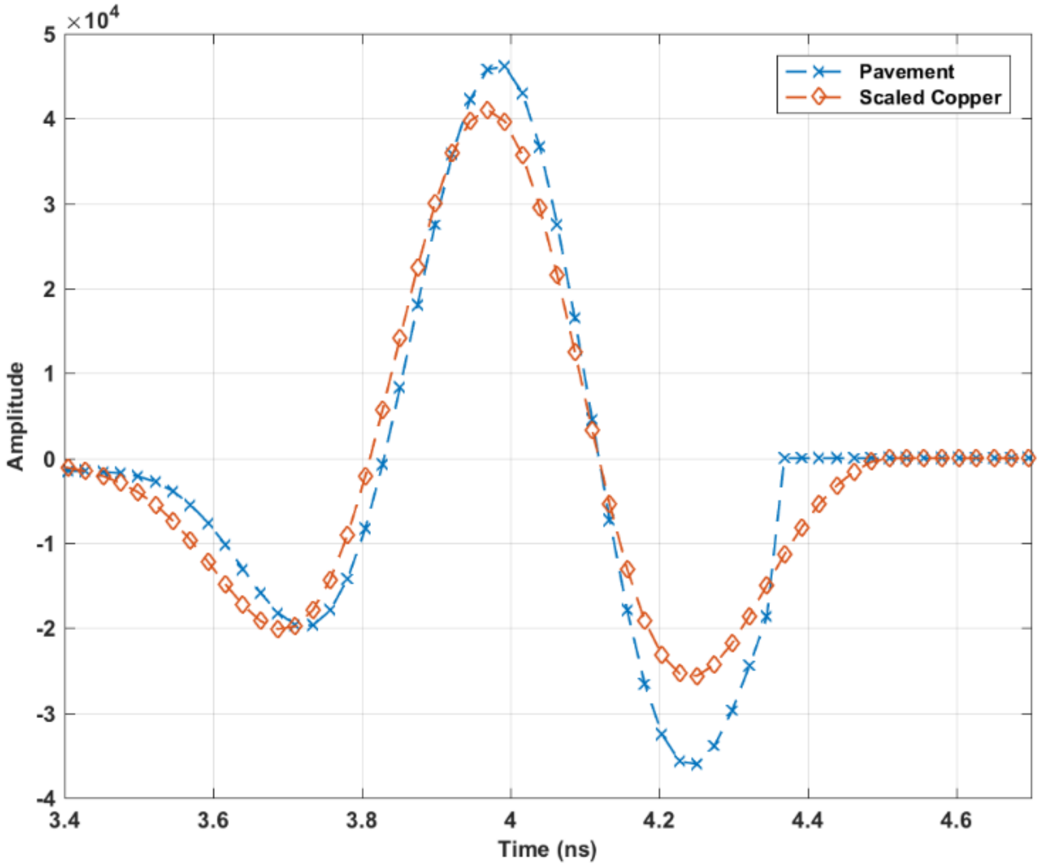

(b)
Figure 8-10 (cont.)

As shown in Figure 8-10(a), the low frequency part of the pavement scan is matched with the copper reflection, while the high frequency part of the pavement reflection is greater than the copper reflection due to the effect of surface moisture. In time domain plot Figure 8-10(b), it can be seen that the scaled copper has a lower peak than the pavement reflection.

Due to the installation position of the antennas on the roller, only data collected when roller was backing up were used, and 8 measurements were obtained. The density (G_{mb}) and air voids prediction results are presented in Figure 8-11. The air void is calculated using:

$$\text{Air void} = \frac{G_{mm} - G_{mb}}{G_{mm}}. \tag{8-8}$$

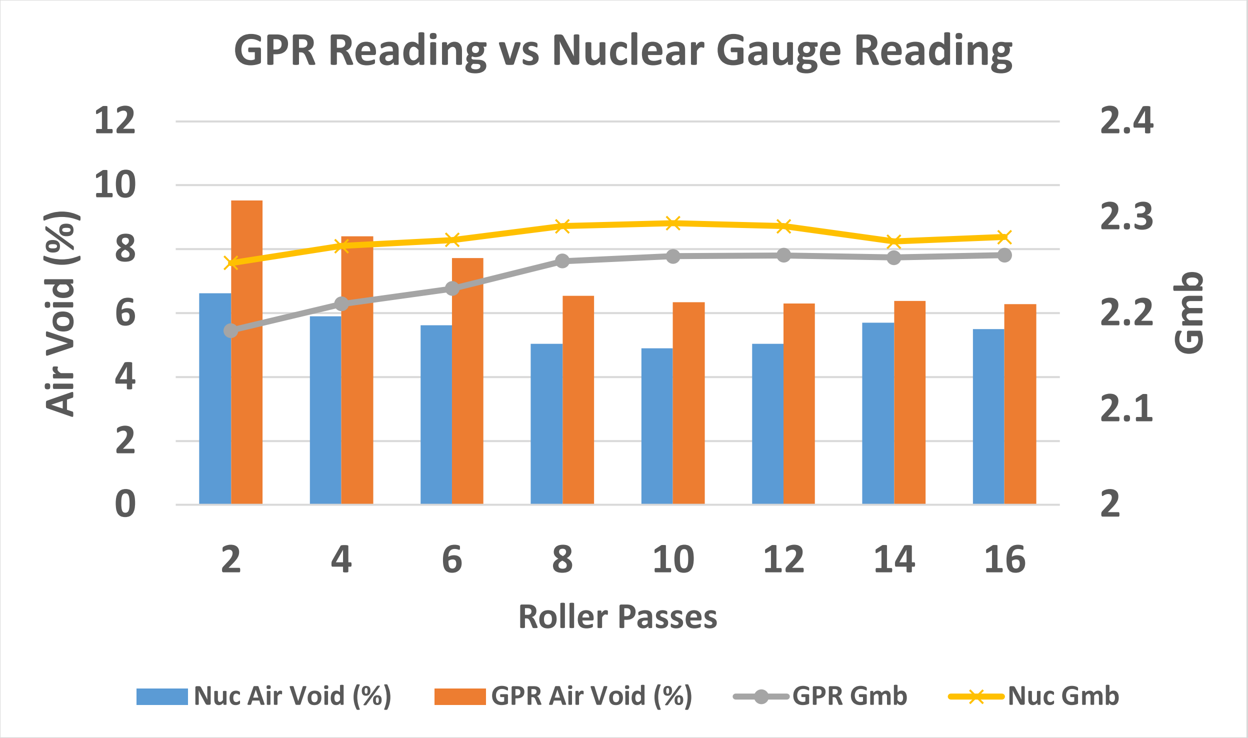

Figure 8-11 G_{mb} and air voids prediction using GPR and nuclear density gauge from leveling binder

Results from Figure 8-11 show that the GPR prediction of G_{mb} increases as the roller passes increase. The calculated air void decreases from 9% to 6% from GPR prediction. Similarly, the nuclear density gauge shows a similar change in both G_{mb} and air void percent compared to GPR results. From both GPR and the nuclear density gauge data, the change of air voids is small during the compaction. For dense-graded AC, density is usually achieved during the first several roller passes.

One core for leveling binder and another for SMA surface were taken after the final pass at the nuclear spot as shown in Figure 8-12. The G_{mb} and air void ground truth were then measured in the lab. The comparison of the GPR and nuclear prediction with the ground truth is shown in Table 8-2 for the leveling binder. The GPR G_{mb} and air void prediction errors are -0.50% and 8.28%, respectively, and the nuclear G_{mb} and air void prediction errors are -0.33% and -5.24%, respectively. It shows that both GPR and the nuclear density gauge provide accurate density prediction results compared with ground truth. It appears that the roller vibration has effect GPR collected data.

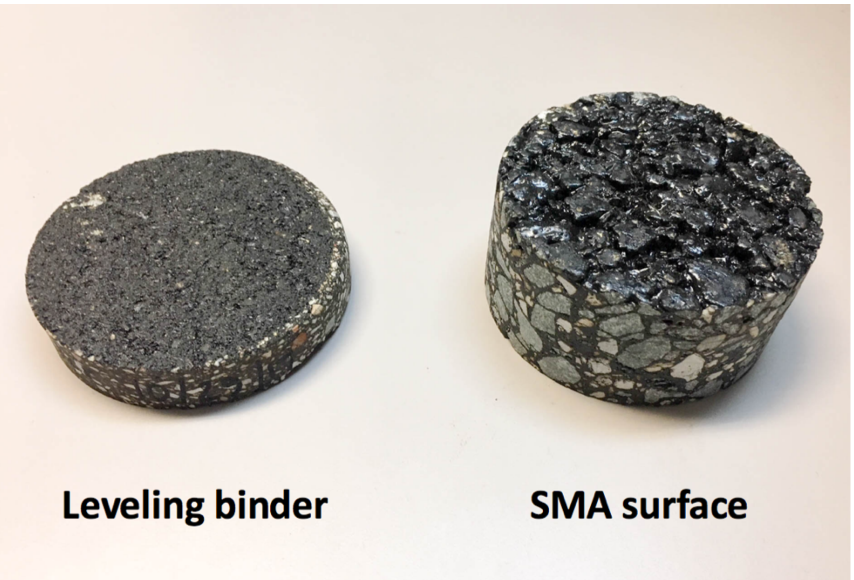

Figure 8-12 Cores taken after the final roller pass on nuclear spot from leveling binder (left) and surface SMA (right)

Table 8-2 Comparison of GPR and nuclear predicted Gmb and air void with ground truth for leveling binder

	G_{mb}	Air void (%)
GPR	2.2605	6.28
GPR error	-0.50%	8.28%
Nuclear	2.2794	5.50
Nuclear error	0.33%	-5.24%
Ground truth	2.2719	5.80

Similar to Figure 8-10, an example of the GPR signal collected from the SMA surface was shown in Figure 8-13. The non-linear optimization is not used in the SMA surface reflection signal processing since the thickness of SMA is large and both surface and bottom reflections can be obtained accurately in the time domain.

As shown in Figure 8-13, the wet pavement reflection and the scaled copper reflection are almost identical in both frequency domain and time domain. The surface water amount is relatively low and its effect on pavement surface reflection is small.

Nuclear density measurements were taken every roller pass from 3 passes to 16 passes. Again, only the GPR measurements when the roller was backing up were obtained. The G_{mb} and air void prediction results are presented in Figure 8-14. It can be seen from Figure 8-14 that the trend of the GPR measurements and the nuclear density gauge measurements are similar, but the density prediction from GPR is larger than that from the nuclear gauge at every pass number.

The GPR and nuclear measurements after the last roller pass are compared to the ground truth measured from core (Figure 8-12) in Table 8-3 for the SMA surface. The GPR G_{mb} and air void prediction errors are -0.29% and 7.23%, respectively, and the nuclear G_{mb} and air void prediction errors are -2.61% and -56.73%, respectively. In this case the density results from GPR data are more accurate than the nuclear density measurements.

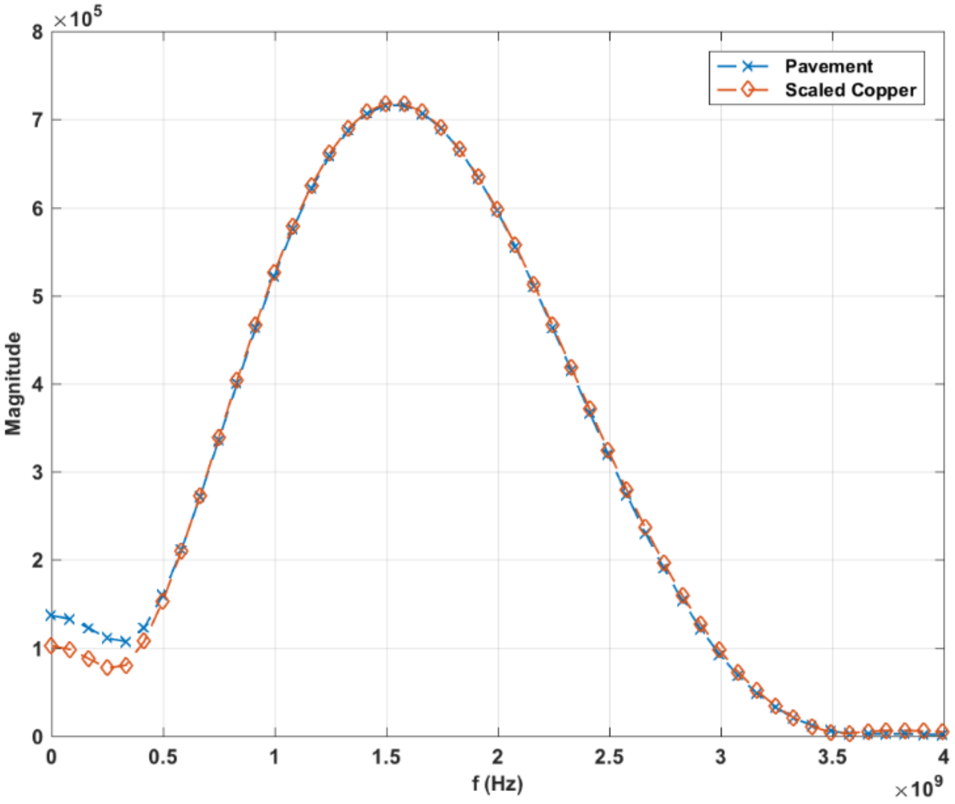

(a)

Figure 8-13 GPR wet scan on SMA surface and scaled copper plate reflection using modified "reference scan" approach in (a) frequency domain and (b) time domain

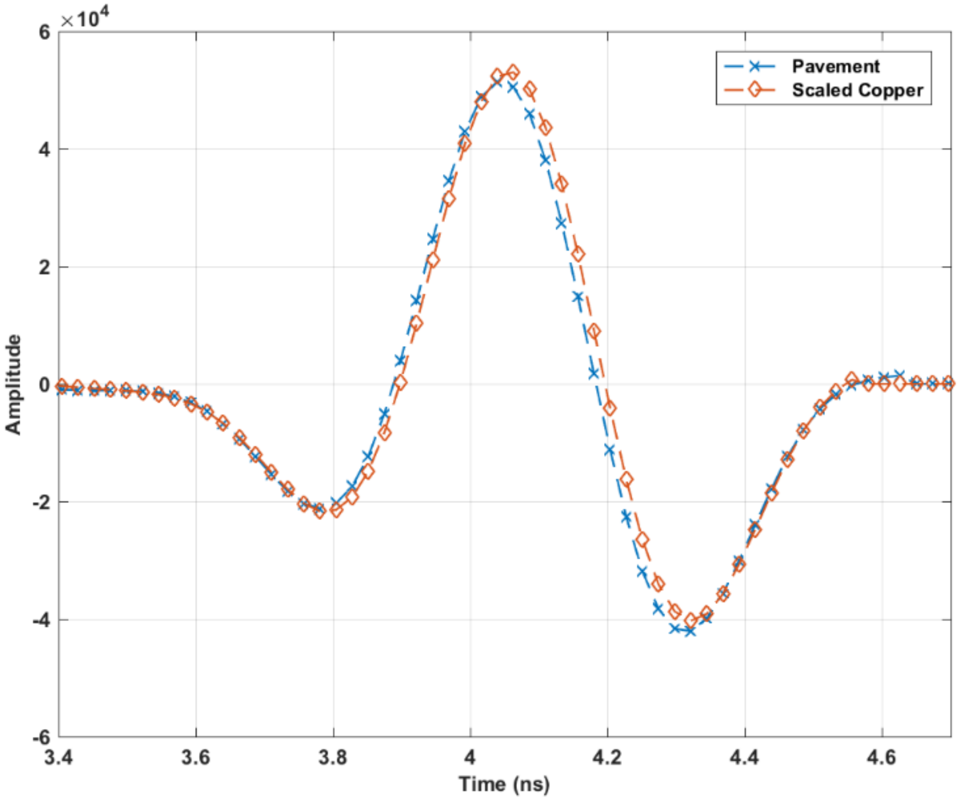

(b)
Figure 8-13 (cont.)

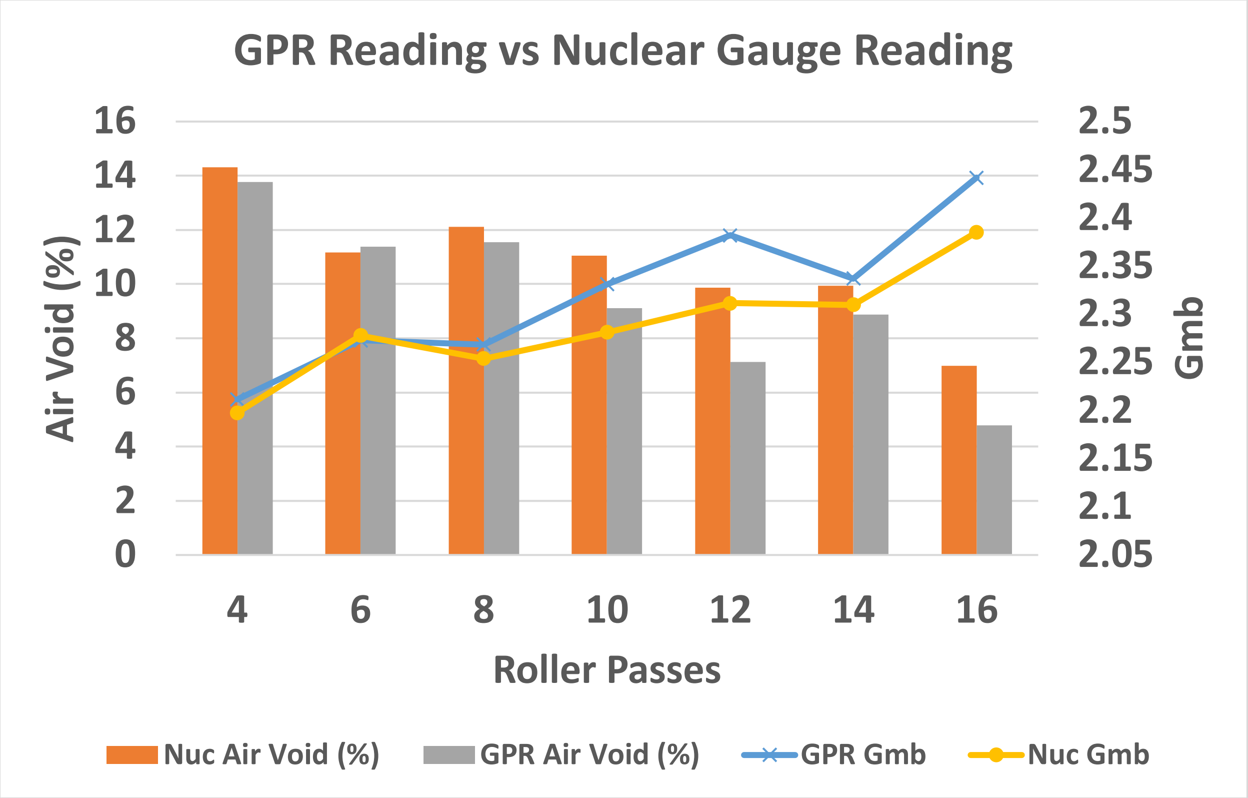

Figure 8-14 G_{mb} and air voids prediction using GPR and nuclear density gauge from SMA surface

Table 8-3 Comparison of GPR and nuclear predicted G_{mb} and air void with ground truth for SMA surface

	G_{mb}	Air void (%)
GPR	2.4418	4.78
GPR error	-0.29%	7.23%
Nuclear	2.3851	6.99
Nuclear error	-2.61%	56.73%
Ground truth	2.4489	4.46

8.5 Summary

In this chapter, a “modified reference scan” approach was proposed to remove the effect of surface moisture on GPR surface reflection, such that the density of AC pavement can be monitored in real-time during compaction. A gradient-descent-based nonlinear optimization method proposed in Chapter 7 was used to increase the resolution of the GPR signals. Compared to the original “reference scan” approach, the modified approach does not require the collection of additional reference GPR scan, and the calculated dielectric constant is more accurate and robust to noises. The “modified reference scan” approach was also validated using a 1 GHz antenna in a laboratory experiment setting.

A field study was conducted near Chicago, IL on a newly constructed AC pavement section. GPR antennas were installed at the front of the roller to monitor the density change. The tests were conducted on thin leveling binder and the SMA surface. For the leveling binder, nonlinear optimization method was first applied on the overlapped GPR signals to reconstruct the surface reflection, then the “modified reference scan” approach was used to calculate the dielectric constant of the pavement. For the SMA surface, only the “modified reference scan” approach was used. The density and air void calculated from GPR were then compared to both nuclear density gauge and core measurements. The following points summarize the findings of the research:

- The gradient-descent-based nonlinear optimization algorithm can be used on GPR signals collected from thin AC overlay to reconstruct surface reflection.
- The introduced “modified reference scan” approach is easier to apply, more reliable, and more generic compared to the original “reference scan” approach.
- The “modified reference scan” approach can be generalized to other antenna frequencies, such as a 1 GHz antenna.
- Field validation, on leveling binder and surface SMA, showed that GPR can accurately predict the AC density and air void content.

This chapter shows that the proposed nonlinear optimization and “modified reference scan” approach is an effective algorithm to be applied on GPR signals to predict AC overlay density during compaction with presence of surface moisture. It shows great potential for using a roller mounted GPR antenna for real-time compaction monitoring.

As a continuation, the following points are suggested for future study:

- The effect of antenna vibration on the GPR signal should be studied to further improve the density prediction accuracy.
- The nonlinearity of the surface reflection should be considered to improve the nonlinear optimization approach when surface moisture is present. The linearity of the system is assumed to calculate the reflection from the bottom of the AC overlay, which could potentially contribute to the density estimation error.

CHAPTER 9: FINDINGS, CONCLUSIONS, AND RECOMMENDATIONS

9.1 Summary

This work investigated the application of GPR on thin AC overlay thickness and density prediction. Compaction monitoring of thin AC overlay was also discussed.

The first half of the dissertation studied the GPR linear inversion problem. In Chapter 3, the general GPR 2-D imaging scheme was presented, and two linear inversion techniques were discussed: migration and sparse reconstruction. An FDTD simulation was conducted to validate the proposed linear inversion techniques. The reconstruction accuracy as well as computation time were assessed for both algorithms. In Chapter 4, thin AC overlay thickness estimation, a special case of GPR image reconstruction, was studied. The deconvolution method was used to reconstruct the TWTT of GPR signals within the thin overlay. Due to the effect of noise, a regularization solution was considered. Four regularization choices, including Tikhonov regularization and total variation regularization, were used on synthesized overlapped GPR pulses, and the thickness estimation accuracy were compared. L-curve criteria were applied to find proper regularization parameter. Chapter 5 further validated the regularized deconvolution method on real GPR data collected on IL-72, and the estimated thin overlay thicknesses were compared to the ground truth from cores.

The second half of the dissertation aimed at complementing the linear inversion techniques presented in the first half of the dissertation. In Chapter 6, a subspace method, the MUSIC algorithm, was utilized to increase the resolution of 3-D GPR signals. Then the XCMP method was used to find both the dielectric constant and the thickness of the thin pavement layer at a full-scale test section. 3-D GPR, together with the XCMP and MUSIC methods, was able to predict thin AC overlay thickness and density at high speed. Next, a non-linear inversion technique was proposed based on gradient descent in Chapter 7. The proposed non-linear gradient descent optimization algorithm was applied on real GPR data reflected from AC overlay, and the thickness and density prediction results are compared to ground truth. Finally, in Chapter 8, a "modified reference scan" approach was developed to eliminate the effect of surface moisture on AC density prediction. The proposed approach was evaluated in both a test section and a case study in Chicago, IL. This method allows real time compaction monitoring of AC pavement and AC overlay using vehicle mounted GPR.

9.2 Findings

The major findings of this study are summarized below:

- Migration and sparse reconstruction are both linear reconstruction algorithms. In this study, GPR signals reflected from drainage pipes were simulated using FDTD. It was found that both migration and sparse reconstruction can be used to reconstruct the upper surface of the drainage pipes, and the depth, diameter and content of the drainage pipes can be accurately determined. Migration requires less computation time, but sparse reconstruction yields more accurate reconstruction results.
- Deconvolution is a special linear inversion technique that can be used to find the thin AC overlay thickness. Four regularization methods, including zero-th order Tikhonov, first order Tikhonov, second order Tikhonov, and total variation regularization, were used to stabilize the deconvolution solution with presence of noise. GPR signals reflected from a two-layered pavement of varying thickness were modeled. The average thickness prediction errors of zero-th order Tikhonov and total variation regularization are 3.28% and 3.14%, respectively, and they outperform the first order and second order Tikhonov regularization. The computation time of zeroth order Tikhonov is 0.512 s, which is faster

than that of total variation regularization, 20.3 s. It was also found that if the impulse distances are smaller than 0.51ns, the regularization methods fail to resolve the overlapped signals.

- In a field study conducted on IL-72, AC overlays were constructed with thickness ranging from 19.1 mm to 50.8 mm. A 2GHz antenna was used to collect static GPR data at different sections. After the zeroth order Tikhonov regularization was used, the surface reflection and reflection from the bottom of the overlay were separated except in two sections, whose thicknesses are 25.4 mm and 19.1 mm, respectively. The thickness estimation errors were below 3 mm for all sections.
- 3-D GPR was used on a full-scale AC overlay section with design thickness ranging from 50 mm to 200 mm. The XCMP method was used to calculate the dielectric constant and thickness of the thin overlay. The MUSIC algorithm was applied to increase the resolution of the 3-D GPR signals. The maximum thickness prediction error when MUSIC algorithm was used was 4 mm.
- A nonlinear gradient descent optimization method was developed to calculate both the dielectric constant and thickness of AC overlay thinner than 25 mm. Based on a FDTD simulation, the accuracy of dielectric constant values greatly improved after the nonlinear gradient descent method was applied. The errors of thickness estimation for all layer thicknesses and noise levels were all below 1 mm. The proposed nonlinear optimization method was further validated in a field test, and the average thickness and G_{mb} estimation errors were 3 mm and 1.81%, respectively.
- A “modified reference scan” approach based on optimization was proposed to correct the surface reflection coefficient from surface moisture effects. A field test on a newly-

constructed AC overlay section was conducted to validate the method. GPR antennas were installed at the front of the roller to monitor the density change. GPR readings were taken after each of the roller passes to calculate the density of the overlay. After the final roller pass, the density prediction from GPR were compared to the ground truth. Using the "modified reference scan" approach, the density prediction errors are -0.50% and -0.29% for leveling binder and SMA surface, respectively.

9.3 Conclusions

Based on the results of this study, we draw the following conclusions:

- With the proposed super-resolution methods, GPR can be used for estimating thin AC overlay thickness and density fast, non-destructively, accurately, and reliably. This allows for QA/QC of thin AC overlay after construction, and also evaluating the condition of existing thin AC overlay.
- The regularized deconvolution method can be used to calculate thin AC overlay thickness when the AC overlay thickness is above a critical threshold. For a 2GHz antenna with Ricker wavelet as incident wave, the critical threshold is generally from 12.7 mm to 38.1 mm depending on the dielectric constant of the AC pavement. This method is robust to noises, and it doesn't require the prior knowledge of the pavement structure.
- The MUSIC algorithm can achieve a higher accuracy and precision in the time delay estimation compared to regularized deconvolution. In practice, the XCMP method can be combined with the MUSIC algorithm to predict AC overlay thickness and density.
- Compared to regularization, the nonlinear gradient descent method could be used on AC overlays less than 25 mm thick and can also be used to find the density of the AC overlay.

- The “modified reference scan” approach is an effective algorithm to be applied on GPR signals to predict AC overlay density with presence of surface moisture, which makes it possible to monitor AC pavement density in real time during compaction using roller mounted GPR antenna. Compared to the original “reference scan” approach, the “modified reference scan” approach is easier to apply, more accurate, more robust to noise, and can be generalized to other antenna frequencies.

9.4 Recommendations

This study shows that as an NDE tool, GPR can be used for thin AC overlay thickness and density prediction as well as AC overlay compaction monitoring. As a continuation of this research, following recommendations are proposed:

- The regularized deconvolution, nonlinear gradient descent optimization, MUSIC algorithm, and “modified reference scan” approach need to be further investigated with other GPR systems. In this study, most of the findings are based on 2GHz air coupled antenna with Ricker wavelet as incident signal. Other antenna types (e.g. stepped frequency antenna), incident signal types, and center frequencies may require different optimal parameters in these algorithms.
- For real time compaction monitoring of AC overlay, the effect of antenna vibration should be further incorporated to increase the density prediction accuracy.
- The effect of binder aging on the density prediction model accuracy need to be further studied.
- The asphalt mixture density prediction model should be further modified to include water as part of the mixture component.

REFERENCES

Acott, M. (1991). *Thin Hot Mix Asphalt Surfacings* (No. IS-110).

Akaike, H. (1974). A new look at the statistical model identification. *IEEE Transactions on Automatic Control*, 19(6), 716-723.

Al-Qadi, I. L., Lahouar, S., & Loulizi, A. (2001). In situ measurements of hot-mix asphalt dielectric properties. *NDT & E International*, *34*(6), 427-434.

Al-Qadi, I., Lahouar, S., & Loulizi, A. (2003). Successful application of ground-penetrating radar for quality assurance-quality control of new pavements. *Transportation Research Record: Journal of the Transportation Research Board*, (1861), 86-97.

Al-Qadi, I. L., & Lahouar, S. (2005). Measuring layer thicknesses with GPR–Theory to practice. *Construction and Building Materials*, 19(10), 763-772.

Al-Qadi, I., Leng, Z., Lahouar, S., & Baek, J. (2010). In-place hot-mix asphalt density estimation using ground-penetrating radar. *Transportation Research Record: Journal of the Transportation Research Board*, (2152), 19-27.

Al-Qadi, I. L., Zhao, S., & Shangguan, P. (2016). Railway ballast fouling detection using GPR data: Introducing a combined time–frequency and discrete wavelet techniques. *Near Surface Geophysics*, *14*(2), 145-153.

Allred, B. J., Fausey, N. R., Peters, L., Chen, C. C., Daniels, J. J., & Youn, H. S. (2004a). Detection of buried agricultural drainage pipe with geophysical methods. *Applied Engineering in Agriculture*, *20*(3), 307.

Allred, B., Fausey, N., Chen, C. C., Peters, L., Youn, H. S., & Daniels, J. (2004b, June). GPR detection of drainage pipes in farmlands. In *Ground Penetrating Radar, 2004. GPR 2004. Proceedings of the Tenth International Conference on* (Vol. 1, pp. 307-310). IEEE.

Antoniou, A. (2006). *Digital signal processing*. Toronto, Canada: McGraw-Hill.

Aster R.C., B. Borchers, C.H. Thurber (2013). *Parameter Estimation and Inverse Problems*, Academic Press, Cambridge.

Beaucamp, B., Fauchard, C., & Laguerre, L. (2013, July). Non destructive assessment of Hot Mix Asphalt compaction with a step frequency radar: Case study. In *Advanced Ground Penetrating Radar (IWAGPR)*, 2013 7th International Workshop on (pp. 1-6). IEEE.

Behari, J. (2006). *Microwave dielectric behaviour of wet soils (Vol. 8)*. Springer Science & Business Media.

Berkhout, A. J. (1986). Seismic inversion in terms of pre-stack migration and multiple elimination. *Proceedings of the IEEE*, 74(3), 415-427.

Blahut, R. E. (2004). *Theory of remote image formation*. Cambridge University Press.

Bleistein, N., & Gray, S. H. (2001). From the Hagedoorn imaging technique to Kirchhoff migration and inversion. *Geophysical Prospecting*, 49(6), 629-643.

Böttcher, C. J. F., van Belle, O. C., Bordewijk, P., & Rip, A. (1978). *Theory of electric polarization (Vol. 2)*. Elsevier Science Ltd.

Bruckstein, A., Shan, T. J., & Kailath, T. (1985). The resolution of overlapping echos. *IEEE Transactions on Acoustics, Speech, and Signal Processing*, 33(6), 1357-1367.

Byrd, R. H., Gilbert, J. C., & Nocedal, J. (2000). A trust region method based on interior point techniques for nonlinear programming. *Mathematical Programming*, *89*(1), 149-185.

California Department of Transportation. (2015). *Highway Design Manual*. Accessed October 2018. <http://www.dot.ca.gov/design/manuals/hdm.html>.

Central Intelligence Agency (2018). *The World Factbook.* Accessed April 3 2018. < https://www.cia.gov/library/publications/the-world-factbook/geos/us.html>.

Craig, I. J., & Brown, J. C. (1986*). Inverse problems in astronomy: a guide to inversion strategies for remotely sensed data. Research supported by SERC*. Bristol, England and Boston, MA, Adam Hilger, Ltd., 1986, 159 p.

Culick, F. E. C. (1987). A note on Rayleigh's criterion. *Combustion Science and Technology*, 56(4-6), 159-166.

Daniels, David J., (2005). *Ground Penetrating Radar*. John Wiley & Sons, Inc: Hoboken, NJ.

Duran, O., Althoefer, K., & Seneviratne, L. D. (2002). State of the art in sensor technologies for sewer inspection. *IEEE Sensors journal*, *2*(2), 73-81.

Economou, N., Vafidis, A., Hamdan, H., Kritikakis, G., Andronikidis, N., & Dimitriadis, K. (2012). Time-varying deconvolution of GPR data in civil engineering. *Nondestructive Testing and Evaluation*, 27(3), 285-292.

Eide, E., & Hjelmstad, J. (2004). UXO and landmine detection using 3-dimensional ground penetrating radar system in a network centric environment. *Proceedings of ISTMP*.

Federal Highway Administration (2014). *Highway Statistics 2014*. Office of Highway Policy Information. <https://www.fhwa.dot.gov/policyinformation/statistics/2014/>.

Gazdag, J., & Sguazzero, P. (1984). Migration of seismic data. *Proceedings of the IEEE*, 72(10), 1302-1315.

Gilmore, C., Jeffrey, I., & LoVetri, J. (2006). Derivation and comparison of SAR and frequency-wavenumber migration within a common inverse scalar wave problem formulation. *IEEE Transactions on Geoscience and Remote Sensing*, 44(6), 1454-1461.

Golub, G. H., Heath, M., & Wahba, G. (1979). Generalized cross-validation as a method for choosing a good ridge parameter. *Technometrics*, 21(2), 215-223.

Groetsch, C. W. (1977). *Generalized inverses of linear operators*. Marcel Dekker. Inc., New York.

Groetsch, C. W. (1984). *The theory of Tikhonov Regularization for Fredholm Equations*. 104p, Boston Pitman Publication.

Hansen, P. C. (1990). The discrete Picard condition for discrete ill-posed problems. *BIT Numerical Mathematics*, 30(4), 658-672.

Hansen, P. C. (1992). Analysis of discrete ill-posed problems by means of the L-curve. *SIAM Review*, 34(4), 561-580.

Hansen, P. C., & O'Leary, D. P. (1993). The use of the L-curve in the regularization of discrete ill-posed problems. *SIAM Journal on Scientific Computing*, 14(6), 1487-1503.

Huang, Y. H. (2004). *Pavement analysis and design*. Pearson Prentice Hall, Upper Saddle River, NJ.

IEEE Standard 145-1993, (1993). *IEEE Standard Definitions of Terms for Antennas*. Accessed October 16 2018. < https://ieeexplore.ieee.org/document/6758443>.

Ihamouten, A., Bosc, F., Guan, B., Le Bastard, C., Fauchard, C., Lambot, S., & Dérobert, X. (2018). Full-waveform inversion using a stepped-frequency GPR to characterize the tack coat in hot-mix asphalt (HMA) layers of flexible pavements. *NDT & E International*, 95, 17-25.

Illionois, D. O. T. (2010). *Bureau of Design and Environment Manual, Chapter 52*. Illinois Department of Transportation, Springfield, IL.

Illionois, D. O. T. (2012). *Standard Specifications for Road and Bridge Construction*. Illinois Department of Transportation, Springfield, IL.

Jia, X., Zhao, M., Buzza, M., Di, Y., & Lee, J. (2017). A geometrical investigation on the generalized lp/lq norm for blind deconvolution. *Signal Processing*, 134, 63-69.

Jin, J. M. (2011). *Theory and computation of electromagnetic fields*. John Wiley & Sons.

Jolliffe, I. T. (1986). Principal component analysis and factor analysis. In *Principal Component Analysis* (pp. 115-128). Springer, New York, NY.

Kallweit, R. S., & Wood, L. C. (1982). The limits of resolution of zero-phase wavelets. *Geophysics*, 47(7), 1035-1046.

Lahouar, S., Al-Qadi, I., Loulizi, A., Clark, T., & Lee, D. (2002). Approach to determining in situ dielectric constant of pavements: development and implementation at interstate 81 in Virginia. *Transportation Research Record: Journal of the Transportation Research Board*, (1806), 81-87.

Lahouar, S. and Al-Qadi, I.L., 2008. Automatic detection of multiple pavement layers from GPR data. *NDT & E International*, 41(2), pp.69-81.

Lambot, S., Slob, E. C., van den Bosch, I., Stockbroeckx, B., & Vanclooster, M. (2004). Modeling of ground-penetrating radar for accurate characterization of subsurface electric properties. *IEEE Transactions on Geoscience and Remote Sensing*, 42(11), 2555-2568.

Lampe, J., & Voss, H. (2010). Solving regularized total least squares problems based on eigenproblems. *Taiwanese Journal of Mathematics*, 885-909.

Lawson, C. L., & Hanson, R. J. (1995). *Solving Least Squares Problems*. Prentice-Hall: Englewood Cliffs.

Le Bastard, C., Baltazart, V., Wang, Y., & Saillard, J. (2007). Thin-pavement thickness estimation using GPR with high-resolution and superresolution methods. *IEEE Transactions on Geoscience and Remote Sensing*, *45*(8), 2511-2519.

Le Bastard, C., Wang, Y., Baltazart, V., & Derobert, X. (2014). Time delay and permittivity estimation by ground-penetrating radar with support vector regression. *IEEE Geoscience and Remote Sensing Letters*, 11(4), 873-877.

Leng, Z. (2011). Prediction of in-situ asphalt mixture density using ground penetrating radar: theoretical development and field verification (Doctoral dissertation). University of Illinois at Urbana-Champaign.

Leng, Z., Al-Qadi, I. L., & Lahouar, S. (2011). Development and validation for in situ asphalt mixture density prediction models. *NDT & E International*, 44(4), 369-375.

Leng, Z., Al-Qadi, I., Shangguan, P., & Son, S. (2012). Field application of ground-penetrating radar for measurement of asphalt mixture density: case study of illinois route 72 overlay. *Transportation Research Record: Journal of the Transportation Research Board*, (2304), 133-141.

Leng, Z., & Al-Qadi, I. L. (2014). An innovative method for measuring pavement dielectric constant using the extended CMP method with two air-coupled GPR systems. *NDT & E International*, 66, 90-98.

Leuschen, C. J., & Plumb, R. G. (2001). A matched-filter-based reverse-time migration algorithm for ground-penetrating radar data. *IEEE Transactions on Geoscience and Remote Sensing*, 39(5), 929-936.

Li, L. (2014). Sparsity-promoted blind deconvolution of ground-penetrating radar (GPR) data. *IEEE Geoscience and Remote Sensing Letters*, 11(8), 1330-1334.

Liuzzo-Scorpo, A., & Cook, A. (2017). Accuracy evaluation of traffic-speed coreless GPR techniques in pavement layer thickness estimation. In *Advanced Ground Penetrating Radar (IWAGPR), 2017 9th International Workshop on* IEEE, 1-6.

Lyons, R. G. (2011). *Understanding Digital Signal Processing, 3rd* ed. Prentice Hall: Upper Saddle River, NJ.

Lytton, R. L., Uzan, J., Fernando, E. G., Roque, R., Hiltunen, D., & Stoffels, S. M. (1993). *Development and validation of performance prediction models and specifications for asphalt binders and paving mixes*. The Strategic Highway Research Program Rep. No. SHRPA-357, National Research Council, Washington, DC.

Marengo, E. A., Hernandez, R. D., & Lev-Ari, H. (2007). Intensity-only signal-subspace-based imaging. *J. the Optical Society of America*, *24*(11), 3619-3635.

Masad, E., Al-Rub, R. A., & Little, D. N. (2012). Recent developments and applications of pavement analysis using nonlinear damage (Panda) model. In *7th RILEM International Conference on Cracking in Pavements* (pp. 399-408). Springer, Dordrecht.

Morozov, V. A. (2012). *Methods for solving incorrectly posed problems*. Springer Science & Business Media.

Nassiraei, A. A., Kawamura, Y., Ahrary, A., Mikuriya, Y., & Ishii, K. (2006, November). A new approach to the sewer pipe inspection: Fully autonomous mobile robot" kantaro". In *IEEE Industrial Electronics, IECON 2006-32nd Annual Conference on* (pp. 4088-4093). IEEE.

Newcomb, D. E. (2009). *Thin asphalt overlays for pavement preservation* (No. Information Series 135). National Asphalt Pavement Association, Lanham, MD.

Riad, S. M. (1986). The deconvolution problem: An overview. *Proceedings of the IEEE*, 74(1), 82-85.

Roman, H. T., Pellegrino, B. A., & Sigrist, W. R. (1993). Pipe crawling inspection robots: an overview. *IEEE Transactions on Energy Conversion*, 8(3), 576-583.

Saarenketo, T. (1997). Using ground-penetrating radar and dielectric probe measurements in pavement density quality control. *Transportation Research Record: Journal of the Transportation Research Board*, (1575), 34-41.

Sala, J., & Linford, N. (2012). Processing stepped frequency continuous wave GPR systems to obtain maximum value from archaeological data sets. *Near Surface Geophysics*, *10*(1), 3-10.

Savelyev, T. G., & Sato, M. (2004). Comparative analysis of UWB deconvolution and feature extraction algorithms for GPR landmine detection. In *Proc. of SPIE* Vol (Vol. 5415, p. 1009).

Schmidt, R. (1986). Multiple emitter location and signal parameter estimation. *IEEE Transactions on Antennas and Propagation*, 34(3), 276-280.

Schmelzbach, C., & Huber, E. (2015). Efficient deconvolution of ground-penetrating radar data. *IEEE transactions on geoscience and remote sensing*, 53(9), 5209-5217.

Shan, T. J., Wax, M., & Kailath, T. (1985). On spatial smoothing for direction-of-arrival estimation of coherent signals. *IEEE Transactions on Acoustics, Speech, and Signal Processing*, 33(4), 806-811.

Shangguan, P., Al-Qadi, I., Leng, Z., Schmitt, R., & Faheem, A. (2013). Innovative approach for asphalt pavement compaction monitoring with ground-penetrating radar. *Transportation Research Record: Journal of the Transportation Research Board*, (2347), 79-87.

Shangguan, P., & Al-Qadi, I. L. (2015). Calibration of FDTD simulation of GPR signal for asphalt pavement compaction monitoring. *IEEE Transactions on Geoscience and Remote Sensing*, 53(3), 1538-1548.

Shangguan, P., Al-Qadi, I., Coenen, A., & Zhao, S. (2016). Algorithm development for the application of ground-penetrating radar on asphalt pavement compaction monitoring. *International Journal of Pavement Engineering*, 17(3), 189-200.

Shivola, A. H. (1989). Self-consistency aspects of dielectric mixing theories. *IEEE Transactions on Geoscience and Remote Sensing*, 27(4), 403-415.

Sinha, S. K. (2003). State-of-the-art in sensor technologies for pipe inspection. *Proc. Pipeline Eng. Construction Int. Conf.*, 1592-1602.

Sinha, S. K. (2004). A multi-sensory approach to structural health monitoring of buried sewer pipelines infrastructure system. In *Pipeline Engineering and Construction,* 1-12.

Soldovieri, F., Solimene, R., Monte, L. L., Bavusi, M., & Loperte, A. (2011). Sparse reconstruction from GPR data with applications to rebar detection. *IEEE Transactions on Instrumentation and Measurement*, 60(3), 1070-1079.

Son, S., Al-Qadi, I., Lippert, D., & Zehr, T. (2013). Innovative sprinkle treatment for thin durable asphalt overlays. *Transportation Research Record: Journal of the Transportation Research Board*, (2366), 87-97.

Soumekh, Mehrdad. *Synthetic Aperture Radar Signal Processing*. Vol. 7. New York: Wiley, 1999.

Spagnolini, U., 1997. Permittivity measurements of multilayered media with monostatic pulse radar. *IEEE Transactions on Geoscience and Remote sensing*, 35(2), pp.454-463.

Stutzman, W. L., & Thiele, G. A. (2012). *Antenna Theory and Design*. John Wiley & Sons: Hoboken, NJ.

Van Den Berg, E., & Friedlander, M. P. (2008). Probing the Pareto frontier for basis pursuit solutions. *SIAM Journal on Scientific Computing*, 31(2), 890-912.

Wang, S., Zhao, S., & Al-Qadi, I. L. (2018). Continuous real-time monitoring of flexible pavement layer density and thickness using ground penetrating radar. *NDT & E International*, 100, 48-54.

Wax, M., & Kailath, T. (1984, March). Determining the number of signals by information theoretic criteria. In *Acoustics, Speech, and Signal Processing, IEEE International Conference on ICASSP'84*. (Vol. 9, pp. 232-235). IEEE.

Wax, M., & Kailath, T. (1985). Detection of signals by information theoretic criteria. *IEEE Transactions on Acoustics, Speech, and Signal Processing*, *33*(2), 387-392.

Williams, R. T., Prasad, S., Mahalanabis, A. K., & Sibul, L. H. (1988). An improved spatial smoothing technique for bearing estimation in a multipath environment. *IEEE Transactions on Acoustics, Speech, and Signal Processing*, *36*(4), 425-432.

Wright D., Baltazart V., Elsworth N., Hamrouche R., Karup J., Lurdes Antunes M., McRobbie S., Merecos V. and Saarenketo T. (2014). Monitoring structural and surface conditions, *Tomorrow's Road Infrastructure Monitoring and Management (TRIMM), FP7 project 285119*.

Wu, R., Li, J., & Liu, Z. S. (1999). Super resolution time delay estimation via MODE-WRELAX. *IEEE Transactions on Aerospace and Electronic Systems*, *35*(1), 294-307.

Wu, R., Li, X., & Li, J. (2002). Continuous pavement profiling with ground-penetrating radar. *IEE Proceedings-Radar, Sonar and Navigation*, *149*(4), 183-193.

Xu, P. (1998). Truncated SVD methods for discrete linear ill-posed problems. *Geophysical Journal International*, 135(2), 505-514.

Yamada, H., Ohmiya, M., Ogawa, Y., & Itoh, K. (1991). Superresolution techniques for time-domain measurements with a network analyzer. *IEEE Transactions on Antennas and Propagation*, *39*(2), 177-183.

Yilmaz Ö. (2001). *Seismic Data Analysis: Processing, Inversion, and Interpretation of Seismic Data*. Society of Exploration Geophysicists, Tulsa, OK.

Yoder, E. J., & Witczak, M. W. (1975). *Principles of Pavement Design*. John Wiley & Sons: New York.

Youn, H. S., & Chen, C. C. (2004, June). Neural detection for buried pipe using fully polarimetric GPR. In Ground Penetrating Radar, 2004. GPR 2004. *Proceedings of the Tenth International Conference on* (Vol. 1, pp. 303-306). IEEE.

Zeng, X., & McMechan, G. A. (1997). GPR characterization of buried tanks and pipes. *Geophysics*, *62*(3), 797-806.

Zhao, S., Shangguan, P., & Al-Qadi, I. L. (2015). Application of regularized deconvolution technique for predicting pavement thin layer thicknesses from ground penetrating radar data. *NDT & E International*, 73, 1-7.

Zhao, S., & Al-Qadi, I. L. (2016). Development of an analytic approach utilizing the extended common midpoint method to estimate asphalt pavement thickness with 3-D ground-penetrating radar. *NDT & E International*, 78, 29-36.

Zhao, S., & Al-Qadi, I. (2017a). Pavement drainage pipe condition assessment by GPR image reconstruction using FDTD modeling. *Construction and Building Materials*, *154*, 1283-1293.

Zhao, S., & Al-Qadi, I. L. (2017b). Development of regularization methods on simulated ground-penetrating radar signals to predict thin asphalt overlay thickness. *Signal Processing*, 132, 261-271.

Zhao, S., & Al-Qadi, I. L. (2018). Super-resolution of 3-D GPR signals to estimate thin asphalt overlay thickness using the XCMP method. *IEEE Transactions on Geoscience and Remote sensing*, 99, 1-9.

Zhao, S., Al-Qadi, I. L., & Wang, S. (2018). Prediction of thin asphalt concrete overlay thickness and density using nonlinear optimization of GPR data. *NDT & E International*, 100, 20-30.